

MEMS TECHNOLOGY AND DEVICES FOR A MICRO FLUID DOSING SYSTEM

Thesis by

Ellis Meng

In Partial Fulfillment of the Requirements
for the Degree of

Doctor of Philosophy



California Institute of Technology

Pasadena, CA 91125

2003

(Defended January 31, 2003)

© 2003

Ellis Meng

All Rights Reserved

To Tuan

ACKNOWLEDGEMENT

It has been nearly a decade since I started as a freshman at Caltech. Throughout my many years here, I have wonderful encountered many people who have helped define who I am today and are in large part responsible for getting me to this point. I would like to extend my sincerest thanks to all of these people for their friendship and support though all these years.

I have learned a great deal under the guidance of Professor Yu-Chong Tai. His never-ending supply of new ideas and enthusiasm for his research was a source of inspiration for my own work and greatly influenced my decision to stay in academia. I am extremely fortunate to have been a member of his lab.

I have had a number of wonderful and talented officemates during graduate school. Dr. Thomas Tsao has been a great role model, TA, and friend dating all the way back to my undergraduate days. I thank him for encouraging me and me invaluable advice when I applied to graduate school. The many hours in we spent playing volleyball, wallyball, and basketball or discussing the X-Files were not only enjoyable but played a big part keeping me sane in graduate school. Dr. John Wright was my officemate for only a short time but was able to witness his ability to come up with interesting engineering solutions through which he provided me with a different perspective on how to do MEMS. Although graduate school seemed to drag on forever at times, before I even realized it, I became a senior student in the lab. I have to thank Justin Boland for reminding me what it was like to be an ambitious new student and of some of the difficulties that they face. His energy and motivation made me remember why I started this whole process.

Several other current and previous students have helped me along the way. Dr. Xuan-Qi Wang was always in a good mood and made time to explain things or instruct me on various processes. Both he and Dr. Shuyun Wu amazed me in that they managed to be full time graduate students and parents as well. Dr. Xing Yang went out of the way to help me get started in lab. Dr. Charles Grosjean and Ted Harder have been extremely helpful with debugging computer problems and were always interesting to talk to. Many thanks go to Trevor Roper who has single-handedly maintained the lab for years despite all that graduate

students do to hinder his efforts. Rodney Rojas and John van Deusen have helped me in the machine shop since my undergraduate years. They have managed to impart some machining experience and knowledge that has been invaluable in the completion of this thesis.

I also want to acknowledge Professor Joel Burdick, Professor Axel Scherer, Professor Ken Pickar, Professor Jerry Pine, Dr. Qiao Lin, Dr. Fukang Jiang, Dr. Amish Desai, Dr. Wen Hsieh, Ken Walsh, Dr. Nick Pornsinsirak, Dr. Tze-Jung Yao, Dr. Yong Xu, Dr. Sang-wook Lee, Jun Xie, Victor Shih, Qing He, Dr. Yuji Suzuki, Edward Chiu, Howen Mak, Sascha Gassmann, Hans Hoeg, Dr. Brett Slatkin, Tanya Hefner, Janice Tucker, and Hung Bui for their help over the years.

I would like to thank my friends and family who have dragged me out of lab and provided me with some semblance of a life outside of work. My family has been extremely supportive and patient in putting up with me during this crazy time. I have many fond memories of adventures and laughs with Stephanie Pao and Frances Tice. Dr. Kim West and the Residence Life staff have given me the opportunity to try something completely different and for that I am grateful.

Finally, I would like to thank Tuan Hoang, to whom this thesis is dedicated, for his unwavering support and encouragement through the best and the worst of times. Without his friendship and advice, this Ph.D. would not have been possible.

ABSTRACT

MEMS TECHNOLOGY AND DEVICES FOR A MICRO FLUID DOSING SYSTEM

Thesis by

Ellis Meng

Doctor of Philosophy in Electrical Engineering

California Institute of Technology

Microelectromechanical systems (MEMS) technology has matured to the point where practical biological and chemical applications are possible. One particularly active research area is in the development of lab-on-a-chip type systems. In order to create successful lab-on-a-chip and other microfluidic systems, it is necessary to have the capability of controlling and directing fluid flow. Such functionality can be found on the front end of a microfluidic system and is known as a fluid delivery or dosing subsystem. For a MEMS micro fluid dosing system to be realized, several components are necessary. The essential components include a fluid actuator, a fluidic control device, and micro plumbing. A prototype fluid delivery system is demonstrated here using a micropump as the fluid actuator, a thermal flow sensor as the fluidic control device, and micromachined couplers as plumbing. The technology to build these components has been developed and each of these components have been fabricated and tested. A prototype constructed of discrete components has also been demonstrated. A truly integrated, channel-based fluid dosing system can be achieved through device scaling.

TABLE OF CONTENTS

CHAPTER 1

Introduction	1
1.1 The Beginning of MEMS	2
1.1.1 Modern Day MEMS and Future Prospects.....	4
1.2 MEMS Technology	5
1.2.1 Fundamental MEMS Techniques	5
1.2.1.1 Lithography	6
1.2.1.2 Bulk Micromachining	6
1.2.1.3 Surface Micromachining	8
1.2.1.4 LIGA	9
1.2.1.5 Wafer Bonding.....	10
1.2.2 Non-Traditional MEMS Techniques	11
1.3 MEMS For Microfluidics Applications	11

CHAPTER 2

A Micro Diaphragm Pump	19
2.1 Micropumping Fundamentals	20
2.1.1 Basic Pump Output Parameters.....	20
2.1.2 Mechanical Pumping Schemes	22
2.1.2.1 Actuation Methods.....	22
2.1.2.2 Displacement Pumps	27
2.1.2.3 Dynamic Pumps	31
2.1.3 Non-Mechanical Pumping Schemes	31
2.2 Design and Fabrication.....	32
2.2.1 Parylene Check Valves	32
2.2.1.1 Parylene Fundamentals.....	34
2.2.1.2 Parylene Processing.....	36
2.2.1.3 Parylene Check Valve Fabrication	37
2.2.2 Silicone Rubber Pumping Membrane	39
2.2.2.1 Silicone Rubber Fundamentals	40
2.2.2.2 Silicone Rubber Processing	41
2.2.2.3 Silicone Membrane Fabrication	41
2.2.3 Silicon Rubber Gaskets.....	44
2.2.3.1 Check Valve to Pump Seat Gasket	44
2.2.3.2 Check Valve to Pump Chamber Gasket.....	46
2.2.3.3 Pump Chamber Spacer and Gasket.....	47
2.2.4 External Actuators.....	47
2.2.4.1 Solenoid Valve Controlled Pneumatic Actuation	48
2.2.4.2 Solenoid Plunger Actuator.....	48
2.2.5 Assembly and Packaging	49
2.3 Pump Characterization.....	51

2.3.1	Check Valve Performance	51
2.3.2	Pneumatic Actuation Experiments	53
2.3.3	Mechanical Actuation Experiments	55
2.4	Discussion	58
2.5	Summary	60

CHAPTER 3

Microfluidic Couplers		64
3.1	The Need For Microfluidic Couplers	65
3.1.1	Search for the Ideal Coupler	66
3.1.2	Current Microfluidic Coupling Solutions	67
3.1.2.1	Academic Work	67
3.1.2.2	Commercial Products	71
3.2	Design and Fabrication	72
3.2.1	Design Considerations	72
3.2.2	Micromachined Fluidic Couplers	74
3.2.3	Bulk Couplers	77
3.2.4	Molded Couplers	80
3.2.5	Post Couplers	82
3.2.6	Flanged Couplers	85
3.3	Coupler Testing	87
3.4	Discussion of Results	90
3.5	Summary	91

CHAPTER 4

A Micro Flow Sensing Array		95
4.1	Flow Measurement Methods	96
4.1.1	Physical Principles of Flow Measurement	96
4.1.2	Non-Thermal Flow Measurement Methods	97
4.1.2.1	Differential Pressure FlowMeters	97
4.1.2.2	Variable Area FlowMeters	99
4.1.2.3	Positive Displacement FlowMeters	100
4.1.2.4	Turbine and Impeller FlowMeters	101
4.1.2.5	Electromagnetic FlowMeters	101
4.1.2.6	Vortex Shedding FlowMeters	102
4.1.2.7	Ultrasonic FlowMeters	102
4.1.2.8	Drag Force FlowMeters	103
4.1.3	Thermal Flow Measurement Methods	103
4.1.3.1	Hot-Wire and Hot-Film	104
4.1.3.2	Calorimetric	105
4.1.3.3	Time-of-Flight	106
4.1.4	Flow Sensing Parameters	108
4.1.5	A Brief History of Micromachined Flow Sensors	110
4.2	Device Design	111
4.2.1	Platinum as a Thermal Sensing Material	112
4.3	Fabrication	114
4.3.1	Process Flow 1	114

4.3.2	Process Flow 2.....	117
4.3.2.1	Electroless Gold Plating.....	121
4.4	Packaging.....	122
4.5	Device Characterization.....	123
4.5.1	Temperature Calibration.....	123
4.5.2	Hot Film Mode Flow Testing.....	125
4.5.2.1	Constant Current Operation.....	126
4.5.2.2	King's Law.....	129
4.5.2.3	Transient Response.....	130
4.5.3	Calorimetric Mode Flow Testing.....	131
4.5.4	Time-of-Flight Mode Flow Testing.....	132
4.5.5	Bubble Detection.....	133
4.6	Discussion of Multi-Mode Testing Results.....	134
4.7	Summary.....	135
CHAPTER 5		
	A MEMS Fluid Dosing System.....	139
5.1	Microfluidic Systems.....	139
5.2	Dosing System Construction.....	140
5.3	Testing results.....	141
5.4	Discussion.....	142
5.5	Summary.....	143
CHAPTER 6		
	Conclusion.....	147

LIST OF FIGURES

<i>Number</i>	<i>Page</i>
Figure 1-1 Photolithography Process for Negative and Positive Resists.....	6
Figure 1-2 Isotropic Etching of Silicon.....	7
Figure 1-3 Anisotropic Wet Etching of Silicon	8
Figure 1-4 Anisotropic Dry Etching of Silicon via DRIE Using the Bosch Process.....	8
Figure 1-5 Basic Surface Micromachining Process	9
Figure 1-6 Typical LIGA Process	10
Figure 1-7 Overview of a Typical Lab-on-a-Chip System.....	13
Figure 1-8 Overview of Components in a Fluid Delivery System.....	13
Figure 2-1 Micro Diaphragm Pump Components.....	29
Figure 2-2 Graphic Depiction of Peristaltic Pumping	29
Figure 2-3 A MEMS Peristaltic Pump [9].....	30
Figure 2-4 Valveless Pump Operation	31
Figure 2-5 Check Valve Behavior [35].....	33
Figure 2-6 Check Valve Types Found in Literature [35]	33
Figure 2-7 Parylene S-Tethered Check Valve Operation [35].....	34
Figure 2-8 Two Types of Fabricated Double Sided Check Valves.....	34
Figure 2-9 Types of Commercially Available Parylene.....	35
Figure 2-10 Parylene Deposition Process [37].....	36
Figure 2-11 Double Sided Check Valve Fabrication Process	38
Figure 2-12 BrF ₃ Roughened Silicon	38
Figure 2-13 Rounded Photoresist Step After Hard Baking.....	39
Figure 2-14 SEMs of Fabricated Check Valves.....	39
Figure 2-15 A Linear Polysiloxane Chain	40
Figure 2-16 A Simple Silicone Membrane Process [40]	42
Figure 2-17 Process Flow for Silicone Membrane with Pillars [40].....	42
Figure 2-18 Fabricated Silicone Membrane with Pillars.....	43
Figure 2-19 Circular Silicone Membrane Fabrication Process.....	44
Figure 2-20 Fabricated Circular Membranes.....	44
Figure 2-21 Silicone Gasket Fabrication Process	45
Figure 2-22 Alignment Structures on a Fabricated Gasket and Machined Pump Seat.....	46
Figure 2-23 As-Molded Silicone Check Valve to Pump Chamber Gaskets.....	47
Figure 2-24 Circular Pump Chamber Spacer and Gasket.....	47
Figure 2-25 Cross Section of Solenoid Actuator.....	49
Figure 2-26 Solenoid Actuation Scheme.....	49
Figure 2-27 Two Types of Tips Used on the Solenoid Actuator.....	49
Figure 2-28 Various Views of the 1 st Generation Solenoid Driven Pump.....	50
Figure 2-29 Clamped Pump Chamber Structure.....	51
Figure 2-30 Various Views of Clamped Pumps	51
Figure 2-31 Single Check Valve Testing Results	52
Figure 2-32 Check Valve Array Testing Results.....	52

Figure 2-33 Comparison of Check Valve Schemes.....	53
Figure 2-34 Pneumatic Testing Fixture Schematic.....	54
Figure 2-35 Pneumatic Testing Results of Single Check Valve Pump.....	55
Figure 2-36 Pneumatic Testing Results of Check Valve Array Pump.....	55
Figure 2-37 Solenoid Actuated Pump Testing Fixture and Schematic.....	56
Figure 2-38 Solenoid Actuation Testing Results of Single Check Valve Pump.....	56
Figure 2-39 Solenoid Actuation Testing Results of Single Check Valve Pump with Bossed Membrane.....	57
Figure 2-40 Volume Pumped Per Cycle vs. Frequency of the Various Pumps.....	59
Figure 3-1 Examples of Glued Fluidic Connections Between Fluidic Devices and Tygon Tubing.....	66
Figure 3-2 Early Examples of Fluidic Interconnect Research.....	68
Figure 3-3 Precision Machined PEEK Connectors.....	69
Figure 3-4 Various DRIE Etched Connectors.....	69
Figure 3-5 Various Polymer Based Connectors.....	70
Figure 3-6 Compression Molded Polymer Connectors.....	70
Figure 3-7 Upchurch Scientific NanoPort™ Assemblies.....	72
Figure 3-8 Cross Section of Mismatched and Matched Tubing-to-Fluidic Port Connections..	73
Figure 3-9 Cryogenic Insertion Process.....	76
Figure 3-10 Spray Coating Process.....	76
Figure 3-11 Comparison of Fluidic Coupling Techniques.....	77
Figure 3-12 Bulk Coupler Fabrication Process.....	78
Figure 3-13 Three Dimensional Rendering of a Bulk Coupler.....	78
Figure 3-14 Corner Compensation Schemes and Results.....	79
Figure 3-15 SEMs of Bulk Couplers.....	79
Figure 3-16 Bulk Couplers with Fused Silica Tubing and Assembly Process.....	80
Figure 3-17 Cross Sectional SEM of a Glued Bulk Coupler.....	80
Figure 3-18 Molded Coupler Fabrication Process.....	81
Figure 3-19 Views of Coupler Molds.....	82
Figure 3-20 Molded Coupler with Fused Silica Capillary and Assembly Process.....	82
Figure 3-21 Example of a Possible Coupler System.....	83
Figure 3-22 Post Coupler Fabrication Process.....	84
Figure 3-23 SEMs of Post Couplers.....	84
Figure 3-24 Post Couplers and Assembly Process.....	85
Figure 3-25 Flanged Coupler Fabrication Process.....	86
Figure 3-26 SEM Views of Flanged Couplers.....	86
Figure 3-27 Flanged Coupler with PEEK Tubing and the Assembly Process.....	87
Figure 3-28 Schematic of Coupler Pressure Testing Apparatus.....	88
Figure 3-29 Original Testing Setup.....	88
Figure 3-30 Improved Testing Setup.....	88
Figure 3-31 Silicon Bulk Couplers with Polyimide Coated Fused Silica Capillaries in a Microchannel Device [18].....	91
Figure 3-32 Silicon Post Couplers with PEEK Tubing in a MEMS Flow Sensor [20].....	91
Figure 4-1 Physical Principles Used in Flow Measurement.....	96
Figure 4-2 Examples of Conventional Flowmeters.....	97
Figure 4-3 Hot-Film Operational Modes.....	105
Figure 4-4 3D Views of the Flow Sensor.....	112
Figure 4-5 Electrical Resistivity of Platinum vs. Temperature.....	113

Figure 4-6 First Run Fabrication Process for Flow Sensor.....	115
Figure 4-7 Lift-Off Results of First Fabrication Run	117
Figure 4-8 Second Run Fabrication Process for Flow Sensor.....	118
Figure 4-9 Process Steps for New Lift-Off Technique.....	119
Figure 4-10 Comparison of Lithography Results for New Lift-Off Technique	119
Figure 4-11 Lift-Off Results of Second Fabrication Run	120
Figure 4-12 Effects of Oxide Stress on Sensor Membrane.....	120
Figure 4-13 Views of Packaged Sensors With Electrical and Fluidic Connections	123
Figure 4-14 Temperature Calibration Curves for Both Flow Sensors	123
Figure 4-15 Flow Sensor IV Characteristics.....	124
Figure 4-16 Resistance and Overheat Temperature Dependence on Current	125
Figure 4-17 Flow Sensor Testing Setup	126
Figure 4-18 Uncorrected and Corrected Sensor Output vs. Flow Curves	127
Figure 4-19 Improved Flow Sensor Testing Setup	128
Figure 4-20 Flow Sensor Output at Three Different Overheat Ratios	128
Figure 4-21 Agreement of Sensor Output With King's Law	129
Figure 4-22 Sensor Response at Various Flow Rates	130
Figure 4-23 Short and Long Sensor Time Constants	131
Figure 4-24 Calorimetric Testing Results.....	132
Figure 4-25 Heater Response to a Heat Pulse and Time-of-Flight Results	133
Figure 4-26 Superimposed Detected Heat Pulses at Different Flow Rates	133
Figure 4-27 Sensor Response to the Passage of an Air Bubble Train.....	134
Figure 5-1 Schematic of Micro Dosing System	141
Figure 5-2 Flow Sensor Response to Micropump Induced Flow in Time-of-Flight Mode	142
Figure 5-3 Pump Behavior Analysis by Time-of-Flight Flow Testing.....	143

LIST OF TABLES

<i>Number</i>	<i>Page</i>
Table 1.1 A Brief History of MEMS	3
Table 2.1 Thermal Expansion Coefficients of Common MEMS Materials.....	27
Table 2.2 Physical and Thermal Properties of Parylenes [37]	35
Table 2.3 Physical Properties of MRTV1 and Sylgard 184	41
Table 2.4 Silicone Preparation Procedure.....	41
Table 2.5 Summary of Pump Testing Results.....	58
Table 3.1 List of Parameters Influencing Fluidic Coupler Design.....	67
Table 3.2 Coupler Testing Results Compared to Other Work.....	89
Table 4.1 Operational Modes of Thermal Mass Flow Sensors	104
Table 4.2 Mechanical, Physical, and Thermal Properties of Platinum	113
Table 4.3 TCR and Resistance Characteristics of Common Metals	113
Table 4.4 Process for Electroless Au Plating on Pt	121
Table 4.5 Sensitivities in Hot-Film Mode	128

CHAPTER 1

INTRODUCTION

The invention of the transistor in 1947 by John Bardeen and Walter Brattain of Bell Labs marked the beginning of a revolution in electrical engineering that eventually led to the birth of microelectromechanical systems (MEMS). Soon after this pivotal discovery, a research ensued at a frenzied pace in the development of microelectronics resulting in the introduction of commercial silicon transistors in 1954 and the invention of the first integrated circuit (IC) by Jack Kilby of Texas Instruments in 1958. One of these early pioneers, Gordon Moore, made an astute observation in 1965 that the number of components per IC would double every 2 years. Moore's prediction, now popularly known as Moore's Law, is not completely correct and actually follows an 18-month doubling trend. Even so, this phenomenal growth rate means that we are now able to enjoy personal computers that run on the computing power of tens of millions of transistors in centimeter scale CPU packages [1]. The impact these developments have had on society and the way we live are pervasive and profound. In the

realm of engineering, the boom in microelectronic research has spun off countless new technologies that are continually changing the way in which we engineer solutions to problems. MEMS was inspired by the technologies used to create microelectronic devices. The graduation from micro-electronic to electromechanical devices is a natural progression in the technological evolution of the IC world.

1.1 THE BEGINNING OF MEMS

Perhaps one of the most notable historical events in the development of MEMS was when Richard Feynman challenged the scientific community to explore the realm of miniaturization. During his talk to the American Physical Society in 1959 dubbed “There’s Plenty of Room at the Bottom,” Feynman pointed out the void in research done on “manipulating and controlling things on a small scale.” He explained to scientists that this field “might tell us much of great interest about the strange phenomena that occur in complex situations...a lot of new things that would happen that represent completely new opportunities for design” and that “it would have an enormous number of technical applications.” In order to properly explore this field and be able to construct small machines, it would be necessary to design a new set of infinitesimal machines that not only require scaling but also redesign. Ironically, modern equipment used to construct semiconductor and MEMS devices is by no means infinitesimal but there is hope in self-assembly and nanotechnology that these tiny machines can be realized.

To further entice scientists to think about these issues, Feynman ended his talk with two \$1000 competitions to the first person to print the information on the page of a book in an area $1/25,000$ smaller in linear scale and to make a working electric motor measuring no more than $1/64$ in³. Clearly he turned some heads as two men stepped forth to claim these prizes: the

motor was completed in 1960 by William McLellan [2], an engineer, albeit by cleverly using conventional techniques and the book was reproduced using electron beam lithography by Thomas Newman, a Stanford University graduate student, in 1985 [3].

Feynman’s vision continues to be a source of inspiration to the MEMS community in addition to the relatively new nanotechnology field. One might even go so far as to say that it represents the starting point for both fields. As MEMS technology has reached maturity, it is expected that in the next 20 years, there will be a wealth of development in the MEMS applications arena. MEMS has clearly become an international technology as evidenced by the various terms used to describe it in the different regions of the world (“MEMS” or “micromachining” in the US, “microsystems” in Europe and “micromachines” in Japan). Table 1.1 lists several defining moments and important developments in the history of MEMS.

Table 1.1 A Brief History of MEMS

1950’s	1960’s	1970’s	1980’s	1990’s
“There’s Plenty of Room at the Bottom” [2]	Silicon Piezoresistive Sensors (Honeywell) [4]	Silicon Pressure Transducers (Honeywell)	“Silicon as a Mechanical Material” [5]	Commercial Accelerometer (Analog Devices) [6]
Integrated Circuits	Resonant Gate Transistor (Westinghouse Labs) [7, 8]	Integrated Gas Chromatograph [9]	Polysilicon Surface Micromachining	Digital Mirror Display (TI)
Metal Sacrificial Process	HNA & EDP Etching	Ink Jet Nozzles (IBM) [10] KOH Etching	Polysilicon Micromotors [11, 12] Silicon Wafer Bonding [13] LIGA [14]	Optical Network Switch (Lucent) Silicon Gyroscope (Draper Labs) RF MEMS Optical MEMS Bio MEMS TMAH Etching Micro EDM [15] Deep Reactive Ion Etching (DRIE)

1.1.1 MODERN DAY MEMS AND FUTURE PROSPECTS

While interest in MEMS in the early days was lacking, today we are already seeing the impact of MEMS on the society in which we live. MEMS products have a growing commercial presence. Undoubtedly, the pressure sensor and accelerometers in our cars; the ink jet heads in our printers; and the digital mirror displays in the digital light projectors (DLPs) in our movie theaters are the most popular and prevalent products to date. With the increasing interest in national security, microfluidic systems are being explored as a means to warn of dangerous biological agents. They are also being heavily explored in their ability to aid in chemical and biological assays. MEMS are miniaturized, less expensive versions of their macro world analogs that perform as well as or better. This technology has matured to the point where the transition from pure research to commercial products can be made.

Many have forecasted a continually growing and extremely profitable MEMS market with the primary areas of interest being in data storage, displays, automotive applications, telecommunications, environmental monitoring, and medical/biochemical applications. According to the MEMS Industry Group, there is an estimate 1.6 MEMS devices per person today in the US. By 2004, this number is expected to increase to 5. Also, in 2000, the MEMS industry was estimated to be worth \$2-5 billion and is expected to grow to \$8-15 billion by 2004 [16]. However, even with such positive market indicators, the success of MEMS is still hindered by several factors. Thus far, it is typical that an inordinate amount of time, on the order of several years, is required to take MEMS inventions from research to the market. Another confounding problem is that most MEMS work is still being done in large part by universities and non-profit research facilities. Packaging devices is an ongoing effort and is by no means a perfected technique. Many are working hard to resolve these issues in the near future.

1.2 MEMS TECHNOLOGY

The materials and techniques used in MEMS are continually evolving. MEMS technology is still based largely on borrowed techniques from the semiconductor industry. Some processes are essentially identical to their semiconductor industry analogs; however, other processes have been adapted to suit the specific needs. The underlying focus of a semiconductor process vs. a MEMS process can be drastically different to the extent that frequently it is not possible or very difficult to integrate both electronics and MEMS on the same piece of real estate. Microfabricated semiconductor devices are contained mainly within the top few microns of the substrate material. MEMS devices may require the entire substrate thickness, utilize both sides of the substrate, or even require bonding multiple substrates together. Over the years, the spectrum of processes considered to be part of the MEMS toolbox has expanded greatly. Traditional techniques are still very popular but are now accompanied by a host of newer ones.

1.2.1 FUNDAMENTAL MEMS TECHNIQUES

MEMS has its roots in silicon-based devices from semiconductor fabrication. In addition to silicon, alternative substrates such as metal, glass/quartz, ceramics, plastic, and silicone rubber are gaining in popularity. Driving factors for this change are the desire to move towards producing devices that are biocompatible, use cheaper materials, and are easy to fabricate from both the process standpoint and when considering the required infrastructure to do so. Even so, most devices are still fabricated in silicon because of its well-known electrical and mechanical properties [5]. Silicon-based devices are also attractive in that there is a possibility of integrating electronics next to MEMS devices on the same substrate.

The MEMS toolbox consists of a set of processes that based in silicon microfabrication techniques. The key process steps are lithography, bulk micromachining, surface

micromachining, LIGA, and wafer bonding. The majority of devices are still fabricated using some combination of these techniques.

1.2.1.1 LITHOGRAPHY

Lithography is a method by which pattern transfer can be achieved from a master pattern to the substrate. The fundamental idea is not a new concept and has in fact been employed by artisans since the late 1700's [17]. Lithography in some form is typically the first step in most processes and, as a result, is probably the most important. Photolithography is the most common technology used but in order to keep up with the demanding resolution needs of the semiconductor industry, as alluded to by Moore's Law, technologies such as X-ray lithography, electron beam lithography, and ion beam lithography have been developed [18]. The basic steps for photolithography involving positive and negative resists are shown in Figure 1-1.

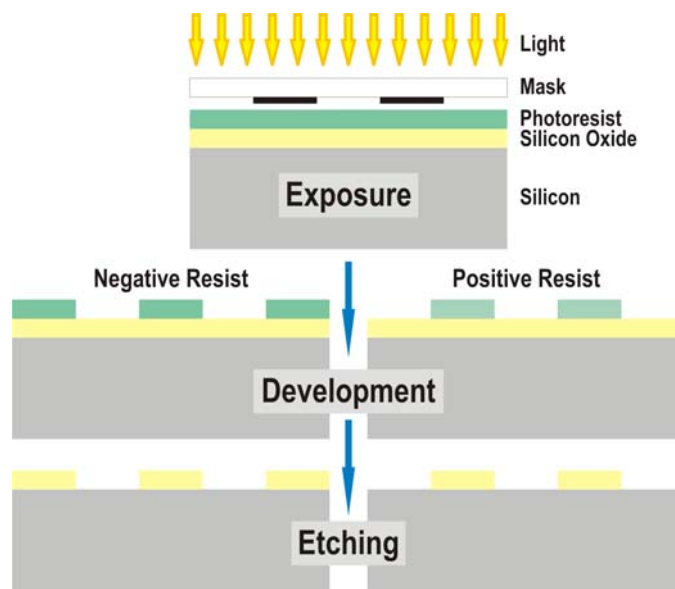


Figure 1-1 Photolithography Process for Negative and Positive Resists

1.2.1.2 BULK MICROMACHINING

Bulk micromachining allows the production of structures carved out of the substrate. Typically, the substrate is silicon, which can be machined using a variety of physical and

chemical etching techniques. Some of these techniques allow etching through the substrate, to fully utilize the entire substrate thickness. In addition, the crystalline nature of silicon can be particularly advantageous when using certain wet etches. Both isotropic and anisotropic, or orientation-dependent, wet etches are readily available (Figure 1-2 & Figure 1-3). Traditional wet etch recipes include HNA (a hydrofluoric, nitric, and acetic acid mix), potassium hydroxide (KOH), ethylenediamine-pyrocatechol-water (EDP), and tetramethylammoniumhydroxide (TMAH) and are still a popular means of carving out channels or creating membranes in silicon. Dry etching techniques such as plasma and gas phase etching (XeF_2 and BrF_3) are also extensively used. Newer techniques, such as deep reactive ion etching (DRIE) [19-21], allow structures with complex in-plane geometry and high aspect ratios ($> 20:1$) to be fabricated (Figure 1-4). Even so, bulk micromachining is not suitable to create all desired geometries. Devices requiring complex, multi-layer or multi-depth structures are frequently difficult or not possible by bulk micromachining alone.

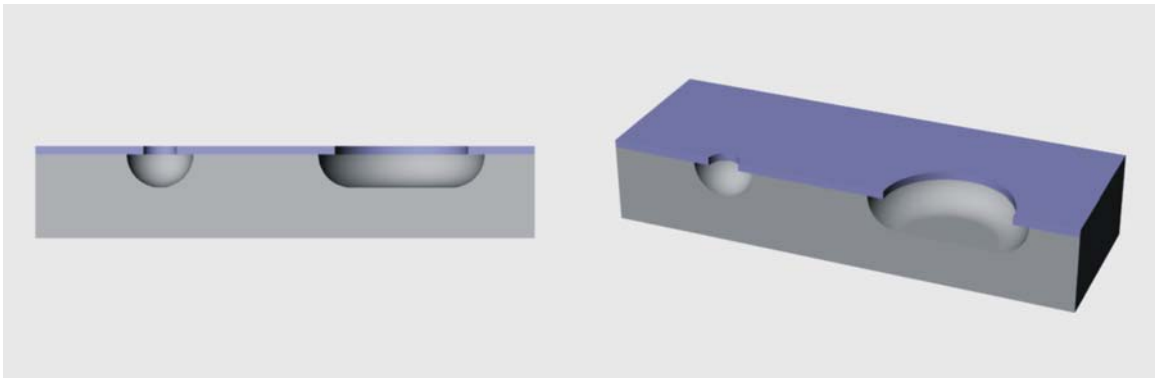


Figure 1-2 Isotropic Etching of Silicon

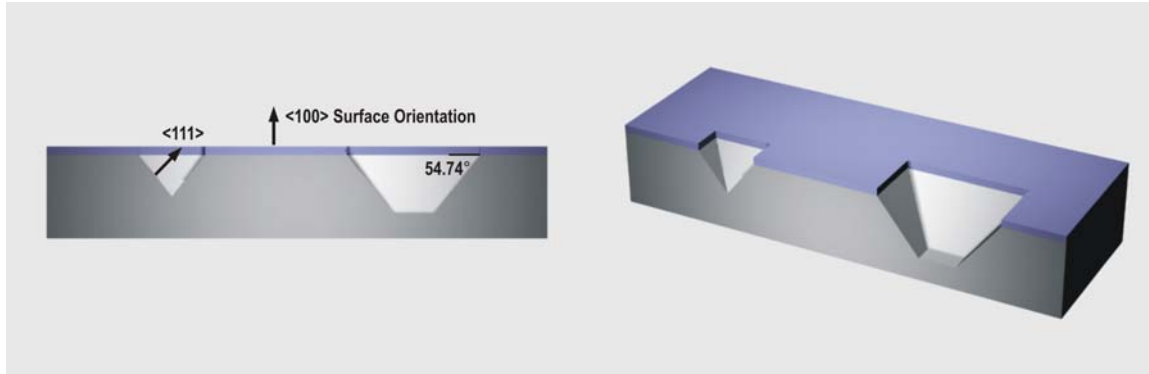


Figure 1-3 Anisotropic Wet Etching of Silicon

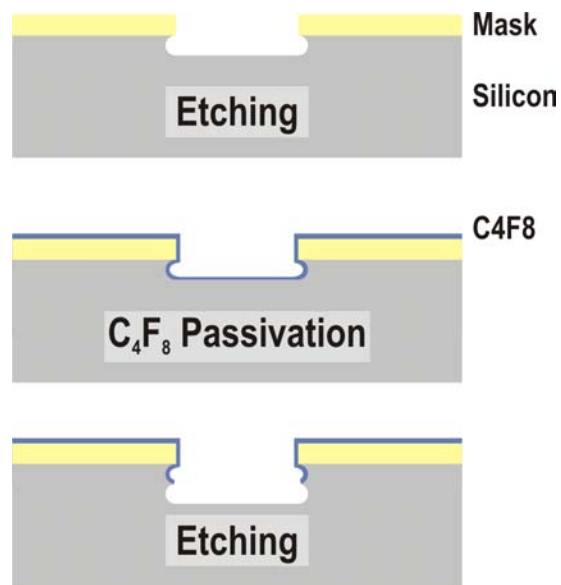


Figure 1-4 Anisotropic Dry Etching of Silicon via DRIE Using the Bosch Process

1.2.1.3 SURFACE MICROMACHINING

To create complex planar structures, it is necessary to use surface micromachining. Here, alternating layers of structural and sacrificial materials are deposited and selectively removed to achieve the desired results (Figure 1-5). As opposed to bulk micromachining, the substrate may or may not be structurally significant in the final device and is often used only as a mechanical support on which to build structural layers. Virtually any material that can be deposited can be used as a structural layer. An assortment of sacrificial layers is available

including phosphosilicate glass (PSG), polysilicon, polymers (photoresist and polyimide), and metals.

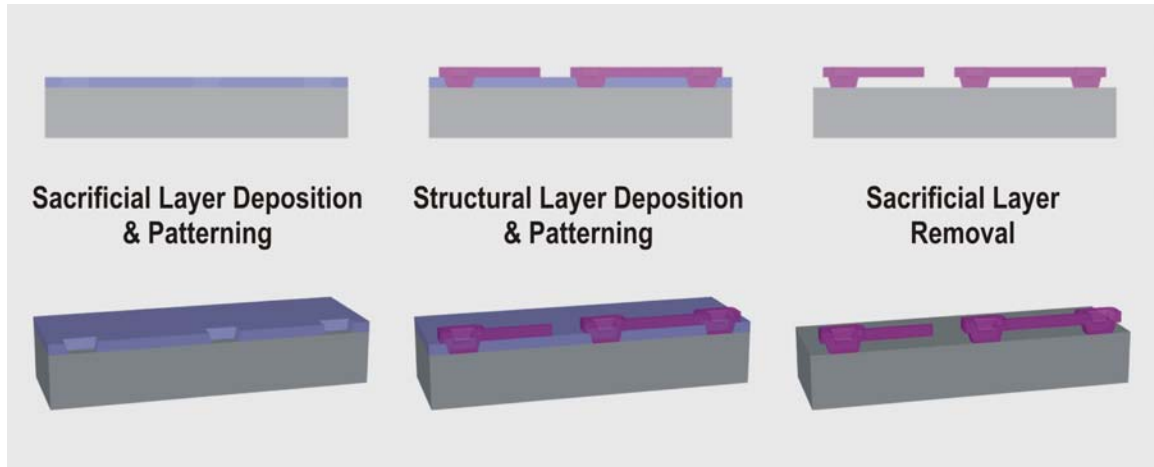


Figure 1-5 Basic Surface Micromachining Process

It is possible to build freestanding, released, and interlocking structures of any desired planar geometry with surface micromachining. Surface micromachining examples include electrostatic micromotors [11, 12], out-of-plane hinged structures [22-24], and springs [25]. However, only thin layers ($\leq \mu\text{m}$) of both the structural and sacrificial materials can be deposited due to stress and other mechanical problems. Thus, the overall thickness of devices created by surface micromachining is relatively thin. In addition, sometimes devices are plagued by stiction.

1.2.1.4 LIGA

LIGA was initially developed in 1982 for the fabrication of micron-sized separation nozzles for nuclear power production applications in Germany [14]. The name is actually derived from the German acronym for “X-ray lithographie galvanofornung abformung,” which means x-ray lithography, electrodeposition, and molding.

Figure 1-6 shows a typical LIGA process. Thick x-ray resist is exposed and used as a mold for electroplating. This newly formed metal mold can then be used to injection mold plastic parts or more plastic molds. High aspect ratio structures ranging from microns to centimeters in height with high resolution ($< 0.2 \mu\text{m}$) can be formed in this manner. An assortment of devices such as accelerometers [26], optical couplings [27], and microfluidic devices [28] have been fabricated using LIGA. While the capability of producing three-dimensional structures using LIGA is attractive, LIGA is a costly process due to the synchrotron source required for x-ray exposure and x-ray masks. Thus, less expensive means of producing the same results are being investigated.

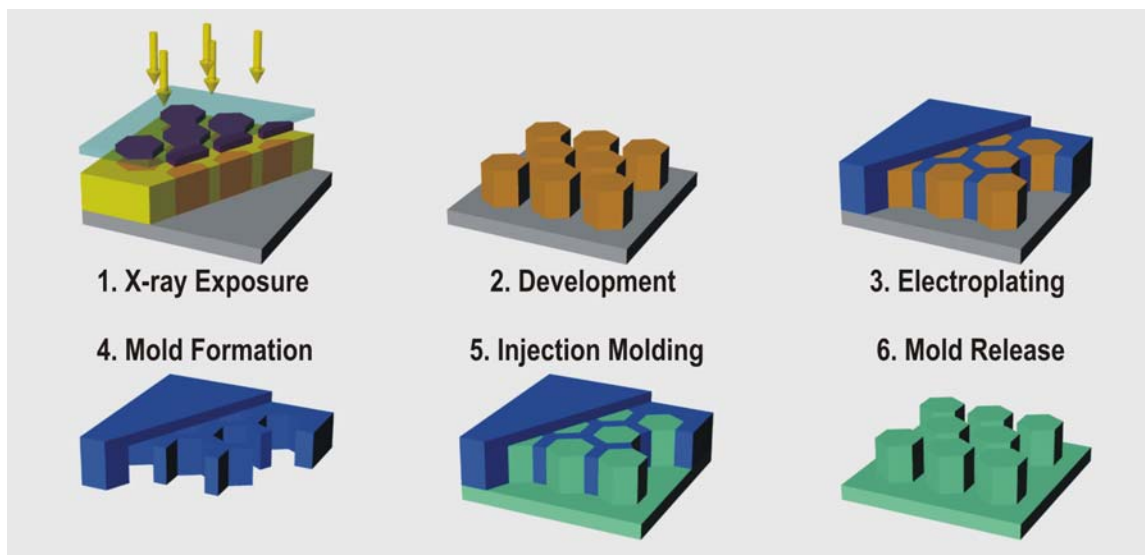


Figure 1-6 Typical LIGA Process

1.2.1.5 WAFER BONDING

Wafer bonding is a convenient means of permanently joining wafers together and circumventing the wafer thickness limitation on devices. It also gives a means to create multi-level devices by combining wafers processed using bulk or surface micromachining or even adding electronics. Other applications of wafer bonding are device packaging and hermetic

sealing. The three most common forms of bonding are fusion bonding (silicon-to-silicon) [19, 29, 30], anodic bonding (silicon-to-glass) [31-33], and eutectic bonding (silicon-to-gold) [34]. Historically, glass-to-metal bonding has been investigated as early as 1969 [35]. The high pressure, temperature, or voltage requirements of certain bonding processes may not be compatible with all devices.

1.2.2 NON-TRADITIONAL MEMS TECHNIQUES

Adding to the wealth of variety in the micromachinist's processing toolbox are a number of non-conventional micromachining techniques that have been developed over the years. The desire to create truly three-dimensional structures has led to the development of micro EDM [15, 36-38], laser micromachining [39, 40], and 3D stereolithography [41, 42]. With the ever-increasing demand for biocompatible devices, plastics have become more popular as are techniques to process them are more readily available. Injection molding [43, 44] and compression molding/hot embossing [45, 46] can be used to fabricate inexpensive plastic parts quickly and in high volume. Another inexpensive and fast process is the "soft lithography" [47, 48] of compliant silicone rubber structures. This technique has become particularly popular in the microfluidics field. As always, man looks back to nature for inspiration; self assembly [49] hopes to bring micromachining to a new level by taking advantage of naturally occurring biological and chemical processes to assemble useful devices and structures.

1.3 MEMS FOR MICROFLUIDICS APPLICATIONS

Much of the attention on MEMS in recent times has been devoted to the development of microfluidics. Biosensors and other tools for chemistry and biology are among the many exciting applications of microfluidics. These efforts are frequently referred to as lab-on-a-chip or micro total analysis systems (μ TAS).

The need for technology to produce devices capable of high throughput, low volume consumption, and producing accurate results already exists in genome sequencing and drug analysis. While these reasons are compelling, miniaturization of systems can also provide impetus for continued progress in microfluidics. Many laboratory techniques common to chemistry and biological require time consuming repetition of many tasks. With microfluidic technology, it is possible not only to miniaturize one specific process, but also to combine a multitude of functionality into one chip level system. By seamlessly integrating tasks such as sample preparation, sample reaction, and product detection, it is possible to speed up processes dramatically. In addition to automating processes, microfluidics offers the possibility of the conduction of massively parallel processes.

Lab-on-a-chip systems may consist of a number of components in a variety of subsystems (Figure 1-7). In general, inputs are converted to the desired outputs through a network of fluidic channels and may encounter a combination of sample preparation stages, reaction chambers, or detectors during this process. While each specific application may require different arrangements of the subsystems, one common element in all of these systems is a fluid delivery and transport mechanism. The ability to control, monitor, and direct flow in a precise and meaningful manner is crucial in the development of practical microfluidic systems for biological and chemical processes.

Many have demonstrated individual devices that are required in a fluid delivery system but complete systems are lacking. In an effort to realize lab-on-a-chip systems, a micro fluid dosing system has been developed. The essential components are a fluid actuator, a fluidic control device, and micro plumbing. MEMS components that were chosen for the development of this system are a micro diaphragm pump (Chapter 2), microfluidic couplers

(Chapter 3), and a micro thermal flow sensing array (Chapter 4). Each piece of the system has been designed, fabricated, and tested prior to implementation in a fluid dosing system (Chapter 5).

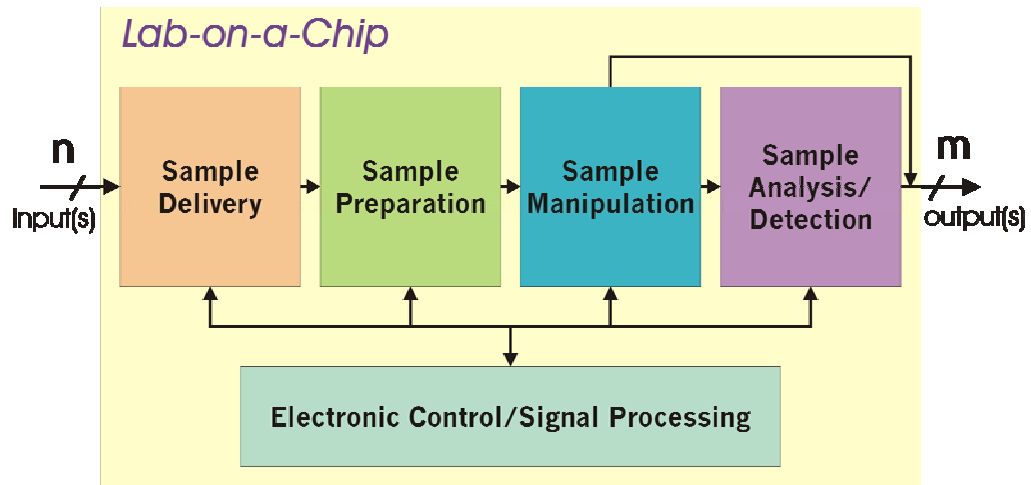


Figure 1-7 Overview of a Typical Lab-on-a-Chip System

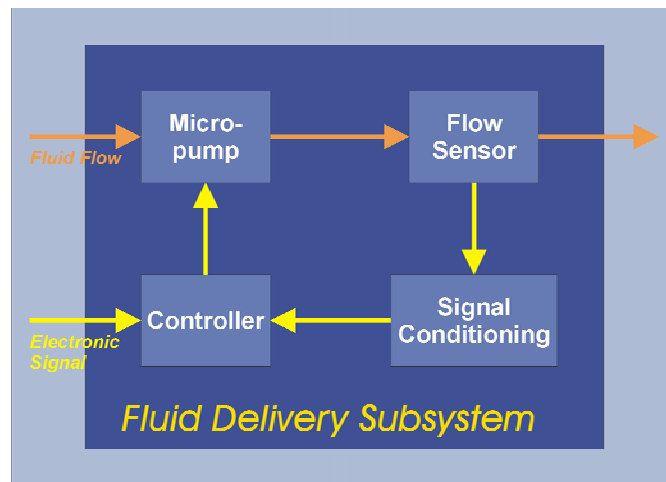


Figure 1-8 Overview of Components in a Fluid Delivery System

REFERENCES

- [1] IC Knowledge, *History of the integrated circuit*.
<http://www.icknowledge.com/history/history.html>.
- [2] Feynman, R.P., *There's Plenty of Room at the Bottom*. Journal of Microelectromechanical Systems, 1992. **1**(1): p. 60-66.
- [3] Foresight Institute, *Prizes Offered by Richard Feynman*.
<http://www.foresight.org/GrandPrize.1.html>.
- [4] Tufte, O.N., P.W. Chapman, and D. Long, *Silicon Diffused-Element Piezoresistive Diaphragms*. Journal of Applied Physics, 1962. **33**(11): p. 3322-3327.
- [5] Petersen, K.E., *Silicon as a Mechanical Material*. Proceedings of the IEEE, 1982. **70**(5): p. 420-457.
- [6] Editor, *Analog Devices Combines Micromachining with BICMOS*, in *Semiconductor International*. 1991. p. 17.
- [7] Nathanson, H.C., W.E. Newell, R.A. Wickstrom, and J.R. Davis, Jr., *The Resonant Gate Transistor*. IEEE Transactions on Electron Devices, 1967. **ED-14**(3): p. 117-133.
- [8] Nathanson, H.C. and R.A. Wickstrom, *A resonant-gate silicon surface transistor with high-Q bandpass properties*. Applied Physics Letters, 1965. **7**(4): p. 84-86.
- [9] Terry, S.C., J.H. Jerman, and J.B. Angell, *Gas-Chromatographic Air Analyzer Fabricated on a Silicon Wafer*. IEEE Transactions on Electron Devices, 1979. **26**(12): p. 1880-1886.
- [10] Bassous, E., H.H. Taub, and L. Kuhn, *Ink jet printing nozzle arrays etched in silicon*. Applied Physics Letters, 1977. **31**(2): p. 135-137.
- [11] Tai, Y.-C. and R.S. Muller, *IC-Processed Electrostatic Synchronous Micromotors*. Sensors & Actuators, 1989. **20**(1-2): p. 49-55.
- [12] Fan, L.-S., Y.-C. Tai, and R.S. Muller, *IC-processed Electrostatic Micromotors*. Sensors and Actuators, 1989. **20**(1-2): p. 41-47.
- [13] Shimbo, M., K. Furukawa, K. Fukuda, and K. Tanzawa, *Silicon-to-silicon direct bonding method*. Journal of Applied Physics, 1986. **60**(8): p. 2987-2989.
- [14] Becker, E.W., W. Ehrfeld, D. Munchmeyer, H. Betz, A. Heuberger, S. Pongratz, W. Glashauser, H.J. Michel, and V.R. Siemens, *Production of Separation Nozzle Systems for Uranium Enrichment by Combination of X-Ray Lithography and Galvanoplastics*. Naturwissenschaften, 1982. **69**: p. 520-523.

- [15] Masaki, T., K. Kawata, and T. Masuzawa, *Micro Electro-Discharge Machining and its Applications*, in *MEMS '90*. 1990: Napa Valley, California. p. 21-26.
- [16] MEMS Industry Group, *MEMS Industry Group Annual Report 2001*. 2001, MEMS Industry Group: Pittsburg, PA.
- [17] Madou, M., *Fundamentals of Microfabrication*. 1997: CRC Press.
- [18] Moreau, W.M., *Semiconductor Lithography: Principles, Practices, and Materials*. Microdevices: Physics and Fabrication Technologies, ed. J.J. Muray and I. Brodie. 1988, New York: Plenum Press.
- [19] Bartha, J.W., J. Greschner, M. Puech, and P. Maquin, *Low temperature etching of Si in high density plasma using SF₆/O₂*. *Microelectronic Engineering*, 1995. **27**(1-4): p. 453-456.
- [20] Clerc, P.-A., L. Dellmann, F. Grétilat, M.-A. Grétilat, P.-F. Indermühle, S. Jeanneret, P. Luginbuhl, C. Marxer, T.L. Pfeffer, G.-A. Racine, S. Roth, U. Staufer, C. Stebler, P. Thiébaud, and N.F. de Rooij, *Advanced deep reactive ion etching: a versatile tool for microelectromechanical systems*. *Journal of Micromechanics and Microengineering*, 1998. **8**(4): p. 272-278.
- [21] Klaassen, E.H., K. Petersen, J.M. Noworolski, J. Logan, N.I. Maluf, J. Brown, C. Storment, M. Wendell, and G.T.A. Kovacs, *Silicon fusion bonding and deep reactive ion etching: a new technology for microstructures*. *Sensors & Actuators A*, 1996. **52**(1-3): p. 132-139.
- [22] Pister, K.S.J., M.W. Judy, S.R. Burgett, and R.S. Fearing, *Microfabricated hinges*. *Sensors & Actuators A*, 1992. **33**(3): p. 249-256.
- [23] Ross, M. and K.S.J. Pister, *Micro-windmill for optical scanning and flow measurement*. *Sensors & Actuators A*, 1995. **47**(1-3): p. 576-579.
- [24] Gunawan, D.S., L.-Y. Lin, and K.S.J. Pister, *Micromachined corner cube reflectors as a communication link*. *Sensors & Actuators A*, 1995. **47**(1-3): p. 580-583.
- [25] Fan, L.-S., Y.-C. Tai, and R.S. Muller, *Integrated Movable Micromechanical Structures for Sensor and Actuators*. *IEEE Transactions on Electron Devices*, 1988. **35**(6): p. 724-730.
- [26] Strohrmann, M., P. Bley, O. Fromhein, and J. Mohr, *Acceleration Sensor with Integrated Compensation of Temperature Effects Fabricated by the LIGA Process*. *Sensors & Actuators A*, 1994. **42**(1-3): p. 426-429.
- [27] Rogner, A., W. Ehrfled, D. Münchmeyer, P. Bley, C. Burbaum, and J. Mohr, *LIGA-based flexible microstructures for fiber chip coupling*. *Journal of Micromechanics and Microengineering*, 1991. **1**(3): p. 167-170.
- [28] Schomburg, W.K., J. Vollmer, B. Büstgens, J. Fahrenberg, H. Hein, and W. Menz, *Microfluidic components in LIGA technique*. *Journal of Micromechanics and Microengineering*, 1994. **4**(4): p. 186-191.

- [29] Harendt, C., W. Appel, H.-G. Graf, B. Höfflinger, and E. Penteker, *Wafer fusion bonding and its application to silicon-on-insulator fabrication*. Journal of Micromechanics and Microengineering, 1991. **1**(3): p. 145-151.
- [30] Harendt, C., H.-G. Graf, B. Höfflinger, and E. Penteker, *Silicon fusion bonding and its characterization*. Journal of Micromechanics and Microengineering, 1992. **2**(3): p. 113-116.
- [31] Hanneborg, A., M. Nese, and P. Øhlekens, *Silicon-to-silicon anodic bonding with a borosilicate glass layer*. Journal of Micromechanics and Microengineering, 1991. **1**(3): p. 139-144.
- [32] Cozma, A. and B. Puers, *Characterization of the electrostatic bonding of silicon and Pyrex glass*. Journal of Micromechanics and Microengineering, 1995. **5**(2): p. 98-102.
- [33] Obermeier, E., *Anodic Wafer Bonding*. Electrochemical Society Proceedings, 1995. **95-7**: p. 212-220.
- [34] Ko, W.H., J.T. Suminto, and G.J. Yeh, *Bonding Techniques for Microsensors*, in *Micromachining and Micropackaging of Transducers*, C.D. Fung, P.W. Cheung, W.H. Ko, and D.G. Fleming, Editors. 1985, Elsevier Science Publishing Company Inc. p. 41-61.
- [35] Wallis, G. and D.I. Pomerantz, *Field Assisted Glass-Metal Sealing*. Journal of Applied Physics, 1969. **40**(10): p. 3946-3949.
- [36] Reynaerts, D., P.-H. Heeren, and H. Van Brussel, *Microstructuring of silicon by electro-discharge machining (EDM) - part I: theory*. Sensors & Actuators A, 1997. **60**(1-3): p. 212-218.
- [37] Heeren, P.-H., D. Reynaerts, H. Van Brussel, C. Beuret, O. Larsson, and A. Bertholds, *Microstructuring of silicon by electro-discharge machining (EDM) - part II: applications*. Sensors & Actuators A, 1997. **61**(1-3): p. 379-386.
- [38] Takahata, K., S. Aoki, and T. Sato, *Fine Surface Finishing Method for 3-Dimensional Micro Structures*. IEICE Transactions on Electronics, 1997. **E80C**(2): p. 291-296.
- [39] Chichkov, B.N., C. Momma, S. Nolte, F. von Alvensleben, and A. Tünnermann, *Femtosecond, picosecond and nanosecond laser ablation of solids*. Applied Physics A, 1996. **63**(2): p. 109-115.
- [40] Müllenborn, M., H. Dirac, J.W. Petersen, and S. Bouwstra, *Fast three-dimensional laser micromachining of silicone for microsystems*. Sensors and Actuators A, 1996. **52**(1-3): p. 121-125.
- [41] Ikuta, K. and K. Hirowatari, *Real Three Dimensional Micro Fabrication Using Stereo Lithography and Metal Molding*, in *MEMS '93*. 1993: Fort Lauderdale, FL. p. 42-47.
- [42] Ikuta, K., K. Hirowatari, and T. Ogata, *Three Dimensional Micro Integrated Fluid Systems (MIFS) Fabricated By Stereo Lithography*, in *MEMS '94*. 1994: Oiso, Japan. p. 1-6.

- [43] Larsson, O., O. Öhman, Å. Billman, L. Lundbladh, C. Lindell, and G. Palmkog, *Silicon Based Replication Technology of 3D-Microstructures by Conventional CD-Injection Molding Techniques*, in *Transducers '97*. 1997: Chicago, IL. p. 1415-1418.
- [44] Despa, M.S., K.W. Kelly, and J.R. Collier, *Injection molding of polymeric LIGA HARMS*. Microsystem Technologies, 1999. **6**(2): p. 60-66.
- [45] Becker, H. and U. Heim, *Hot embossing as a method for the fabrication of polymer high aspect ratio structures*. Sensors & Actuators A, 2000. **83**(1-3): p. 130-135.
- [46] Heckeke, M., W. Bacher, and K.D. Müller, *Hot embossing - The molding technique for plastic microstructures*. Microsystem Technologies, 1998. **4**(3): p. 122-124.
- [47] Xia, Y.N. and G.M. Whitesides, *Soft lithography*. Annual Review of Materials Science, 1998. **28**: p. 153-184.
- [48] Qin, D., Y. Xia, J.A. Rogers, R.J. Jackman, X.-M. Zhao, and G.M. Whitesides, *Microfabrication, Microstructures and Microsystems*. Topics in Current Chemistry, 1998. **194**(5369): p. 1-20.
- [49] Whitesides, G.M., J.P. Mathias, and C.T. Seto, *Molecular Self-Assembly and Nanochemistry: A Chemical Strategy for the Synthesis of Nanostructures*. Science, 1991. **254**: p. 1312-1319.

CHAPTER 2

A MICRO DIAPHRAGM PUMP

Inasmuch as pumping is still the primary means of fluid transport for microfluidic systems today, micropumps are perhaps the most extensively researched topic in microfluidics. With the drive to apply microfluidic solutions to research in genomics, proteomics, and drug discovery, micropump research is focused on producing a practical solution for providing the controlled and accurate transport of fluids. Various actuation and pumping methods have been explored as a solution to moving fluids on the micro scale. Even so, the controlled transport of fluids is critical but not yet practical by micropumps. Also, a fully integrated solution for microfluidics still does not exist; methods presented thus far still have inherent limitations. The two generations of pumps presented here are primarily targeted at moving fluids at relatively high flow rates.

2.1 MICROPUMPING FUNDAMENTALS

Macro world devices directly inspire most of the micropumps that exist today. In fact, many micropumps are modeled exactly after their macroscopic designs. However, micropumps are uniquely able to take advantage of transport effects that provide meaningful forces only at the micro-scale. Electrokinetic [1], acoustic streaming [2], and magnetohydrodynamic [3, 4] effects have inspired a new breed of non-mechanical pumping schemes. In general, pumps can be classified as either mechanical or non-mechanical based on the method by which kinetic energy is obtained to drive fluid flow.

2.1.1 BASIC PUMP OUTPUT PARAMETERS

A designer must consider several parameters to optimize micropump performance. These include maximum flow rate (\dot{Q}_{\max}), maximum back pressure (p_{\max}), pump power (P_{pump}), and pump efficiency (η).

The maximum flow rate is obtained when the pump is working at zero back pressure. Back pressure opposes the work done by the pump and at the maximum back pressure, the flow rate of the pump becomes zero. Pump head (h), or net head, can be derived from the steady flow energy equation assuming incompressible flow and neglecting viscous work and heat transfer. It is the work done on a unit weight of liquid passing from the inlet to the outlet [5]:

$$h = \left(\frac{p}{\gamma} + \frac{u^2}{2g} + z \right)_{\text{out}} - \left(\frac{p}{\gamma} + \frac{u^2}{2g} + z \right)_{\text{in}} \quad (2.1)$$

where:

$\gamma = \rho g$ = pressure head

g = acceleration of gravity

ρ = fluid density

u = velocity

$\frac{u^2}{2g}$ = velocity head

z = elevation.

This represents an increase in Bernoulli head from the inlet to the outlet. Usually, u_{out} and u_{in} are about the same and $z_{\text{out}} - z_{\text{in}}$ is negligible, so the maximum pump head becomes:

$$h_{\text{max}} \approx \frac{P_{\text{out}} - P_{\text{in}}}{\gamma} = \frac{\Delta p}{\gamma} \quad (2.2)$$

Power delivered to the fluid by the pump is the product of the specific weight, discharge, and net head change. It can be expressed as [6]:

$$P_{\text{pump}} = \gamma \dot{Q}_{\text{max}} h_{\text{max}} = \rho g \dot{Q}_{\text{max}} h_{\text{max}} \quad (2.3)$$

If the power required to drive the pump actuator is P_{actuator} , pump efficiency is expressed as:

$$\eta = \frac{P_{\text{pump}}}{P_{\text{actuator}}} \quad (2.4)$$

In an ideal pump, losses would not exist and P_{pump} and P_{actuator} would be identical. Realistically, efficiency is governed by fluid leakage losses (volumetric efficiency), frictional losses (mechanical efficiency), and losses due to imperfect pump construction (hydraulic efficiency). Traditionally, total efficiency is broken up into these three parts [5]:

$$\eta \equiv \eta_v \eta_m \eta_h \quad (2.5)$$

where:

η_v = volumetric efficiency

η_m = mechanical efficiency

η_h = hydraulic efficiency.

2.1.2 MECHANICAL PUMPING SCHEMES

Mechanical pumps can be further classified into displacement vs. dynamic pumps, the distinguishing feature being how mechanical energy is applied to fluid. Displacement systems involve the periodic addition of mechanical energy to modulate the pressure experienced in the pumping chamber. Dynamic systems involve the constant addition of mechanical energy to increase fluid velocities. No closed volumes are involved. The focus here will be on mechanical displacement pumps and their actuation methods. Mechanical pumps are particularly suited for delivering fluid at flow rates of about 10 $\mu\text{l}/\text{min}$ to several milliliters per minute [7].

2.1.2.1 ACTUATION METHODS

Regardless of type, mechanical pumps all required actuators to generate mechanical energy to initiate and sustain fluid flow. The choice of whether to use an integrated versus an external actuator depends on the specific requirements of the application at hand. To achieve large stroke for higher flow rates, the large force and displacement of external actuators is desirable. However, using an external actuator means sacrificing size. Ideally, actuators are easy to construct and can provide large force, have large stroke, have fast response time, run under low power consumption, and have low thermal losses. Various integrated actuation methods have been studied but tradeoffs associated with the various schemes may not be acceptable

based on pump design specifications. Currently, a micro actuator that possesses all of the ideal characteristics mentioned does not exist. Several popular micro actuation methods are discussed here.

2.1.2.1.1 PNEUMATIC

Pneumatic actuation is certainly the easiest to design for in a micropump and interfacing requires very little device real estate. Micro-pneumatic sources are not readily available. Thus, such an actuation scheme is not portable, however, new research towards on-chip pressure sources may make pneumatic actuation a practical for portable devices in the future. The current state of the art is only able to sustain a short air pulse and is designed to be disposable [8]. Typically, bursts of gas used to drive micropumps are obtained from an external pressure source that is regulated by off-the-shelf pneumatic on-off valves [9, 10]. Commercial products for constructing pneumatic manifolds are readily available leaving only the micro-to-macro scale interface to the designer. Thus, for prototyping needs, pneumatic actuation provides an inexpensive and quick means to validate designs.

2.1.2.1.2 ELECTROSTATIC

Electrostatic actuation is based on the Coulombic attraction force between oppositely charged plates. By using the parallel plate approximation to Coulomb's Law, the force generated between the plates when a voltage is applied can be expressed as:

$$F = \frac{dW}{dx} = \frac{1}{2} \frac{\epsilon_0 \epsilon_r A V^2}{x^2} \quad (2.6)$$

where:

F = electrostatic attraction force

W = energy stored

$\epsilon = \epsilon_0 \epsilon_r$ = dielectric constant

A = electrode area

V = applied voltage

x = electrode spacing.

The non-linear relationship between the generated force versus the applied voltage and generated force versus distance are not ideal. It is evident that increasing the applied voltage will increase the force obtained, however, power consumption will be sacrificed. Parameters that are more practical to consider when designing electrostatic actuators are the electrode area and spacing. Large electrode area may not always be available so to maximize the force output, the gap distance should be as small as possible. A force of about 400 μN is generated for the following conditions:

$$\epsilon = 8.85 \times 10^{-12} \frac{\text{N}}{\text{V}^2} \text{ for air}$$

$$A = 1 \text{ mm}^2$$

$$V = 100 \text{ V}$$

$$x = 10 \mu\text{m}.$$

It can be seen that small forces and strokes are typical of electrostatic actuators. Thus, only low flow rates are easily achievable using electrostatic actuation. Such actuators also suffer from effects of fringing fields and large voltage requirements. The benefits are fast response time, reliability, and low power consumption.

2.1.2.1.3 ELECTROMAGNETIC

A wire carrying a current in the presence of a magnetic field will experience the Lorentz force, which can be describe by:

$$\mathbf{F} = (\mathbf{I} \times \mathbf{B})L \quad (2.7)$$

where:

\mathbf{F} = electromagnetic (Lorentz) force

\mathbf{I} = current passing through wire

\mathbf{B} = magnetic field

L = length of wire.

A force on the order of 0.1 mN is generated for the following conditions:

$$\mathbf{I} = 1 \text{ A}$$

$$\mathbf{B} = 0.1 \frac{\text{N}}{\text{m-A}}$$

$$L = 1 \text{ mm.}$$

While the forces generated are large, electromagnetic actuation requires an external magnetic field usually present in the form of an external permanent magnet. Also, the current requirement can result in high power consumption as well as heating issues.

2.1.2.1.4 PIEZOELECTRIC

Piezoelectric actuation involves the strain induced by an applied electric field. High stress and fast response times are typical of piezoelectric actuators. However, fabrication is complex, as piezo-materials are not easily processed. Given the fabrication constraint, frequently, piezoelectric actuators are external and not integrated.

2.1.2.1.5 THERMOPNEUMATIC

Thermopneumatic actuation relies on the thermally induced volume change and/or phase change of fluids sealed in a cavity with at least one compliant wall. For liquids, the pressure increase is expressed as:

$$\Delta P = E \left(\beta \Delta T - \frac{\Delta V}{V} \right) \quad (2.8)$$

where:

ΔP = pressure change

E = bulk modulus of elasticity

β = thermal expansion coefficient

ΔT = temperature increase

$\frac{\Delta V}{V}$ = volume change percentage.

For simplicity, assume no volume expansion. Thus, for water, the temperature-dependent pressure change can be expressed as 76 psi/°C for the following conditions:

$$E = 3.3 \times 10^5 \text{ psi}$$

$$\beta = 2.3 \times 10^{-4} \text{ } ^\circ\text{C}^{-1}.$$

Such a large pressure translates to large deflections and forces but suffer from high power consumption and slow response time which are characteristic of thermal actuation methods.

In addition, the requirement for a sealed cavity implies that fabrication will be complicated and difficult.

2.1.2.1.6 BIMETALLIC

Bimetallic actuation depends on the thermal expansion coefficient differences of materials.

When dissimilar materials are bonded together and subjected to temperature changes,

thermally induced stresses can provide a means of actuation. However, even though forces generated may be large and the implementation can be extremely simple, the deflections achieved are small as the thermal expansion coefficients are also small. The thermal expansion coefficients for some popular MEMS materials are given in Table 2.1 [11]. Large deflections are only achievable at higher temperatures, which limits the usefulness of such actuators.

Table 2.1 Thermal Expansion Coefficients of Common MEMS Materials

Material	Thermal Expansion Coefficient (ppm/°K)
Silicon	2.60
Polysilicon	2.33
Silicon Dioxide	0.35
Silicon Nitride	1.60
Aluminum	25.00
Gold	14.20
Nickel	13.00
Copper	16.50
Platinum	8.80

2.1.2.1.7 SHAPE MEMORY EFFECT

Shape memory actuators involve special alloys that undergo reversible temperature-dependent phase transitions. Alloys start in the martensite phase and transform into the austenite phase when heated. These phase transitions result in mechanical deformations that can be useful for actuation. But, as with all thermal actuators, high power consumption is required and the response time is slow. Also, special alloys such as Au/Cu, In/Ti, and Ni/Ti are required.

2.1.2.2 DISPLACEMENT PUMPS

2.1.2.2.1 CHECK-VALVE/DIAPHRAGM/MEMBRANE PUMPS

Perhaps the most popular pump in both the micro- and macro-scale is the diaphragm pump. A simple schematic is shown in Figure 2-1. The key components include an actuator, flexible pump membrane, pump chamber, and two check valves. In diaphragm pumps, fluidic

transport is achieved by alternating the production of under- and over-pressures in the pump chamber. This results in a supply mode and a pump mode, respectively. During these modes, pumping occurs only when enough pressure difference is produced to overcome the cracking pressure (Δp_{crit}) of the rectifying valves. The pressure generated is a function of the stroke volume (ΔV) produced by the actuator. The actuator also has to contend with a dead volume (V_0) present in the pumping chamber. Diaphragm pump performance is governed by the compression ratio (ε):

$$\varepsilon = \frac{\Delta V}{V_0} = \frac{\text{stroke volume}}{\text{dead volume}} \quad (2.9)$$

The compression ratio for diaphragm pumps is typically small due to small actuator strokes and large dead volume. For liquid pumps, the minimum compression ratio is [12]:

$$\varepsilon_{\text{liquid}} > \kappa |\Delta p_{\text{crit}}| \quad (2.10)$$

where κ is the compressibility of the liquid. For water, $\kappa = 0.5 \times 10^{-8} \frac{\text{m}^2}{\text{N}}$, which is small, like that of most liquids. Thus, this condition is easily met if perfect pump priming is assumed. However, pump priming is by no means trivial and gas bubbles are frequently trapped in the pump chamber. This relationship is a useful tool in designing self-priming micropumps. Given these parameters, successful micro diaphragm pumps are characterized by small critical pressures, large stroke volume, and small dead volume. There are numerous examples of micro diaphragm pumps [13-15].

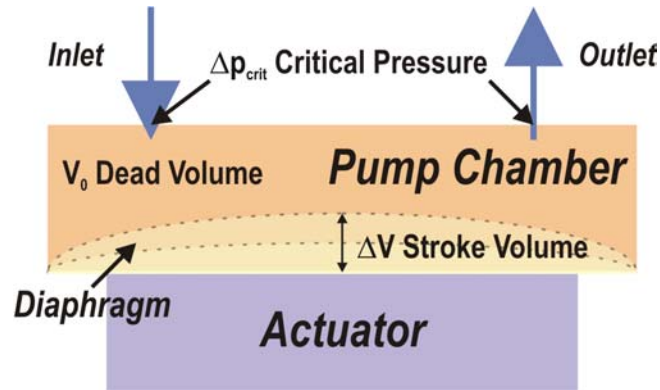


Figure 2-1 Micro Diaphragm Pump Components

2.1.2.2.2 PERISTALTIC PUMPS

Peristaltic pumps operate based on the peristaltic motion of sequentially arranged pumping chambers (Figure 2-2) [16]. This motion squeezes fluid from one point to another. Although they are structurally simplistic compared to diaphragm pumps, which require check valves, reverse leakage can be a major problem for peristaltic pumps. The planar layout of such pumps allows for ease of fabrication and assembly but multiple actuators with control electronics are required to drive these pumps. Several MEMS implementations of peristaltic pumps have been explored (Figure 2-3) [9, 10, 17]. Large stroke volume and compression ratio are strategies for improving peristaltic pumps.

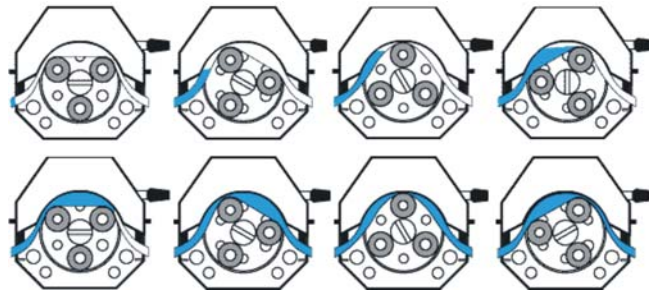


Figure 2-2 Graphic Depiction of Peristaltic Pumping

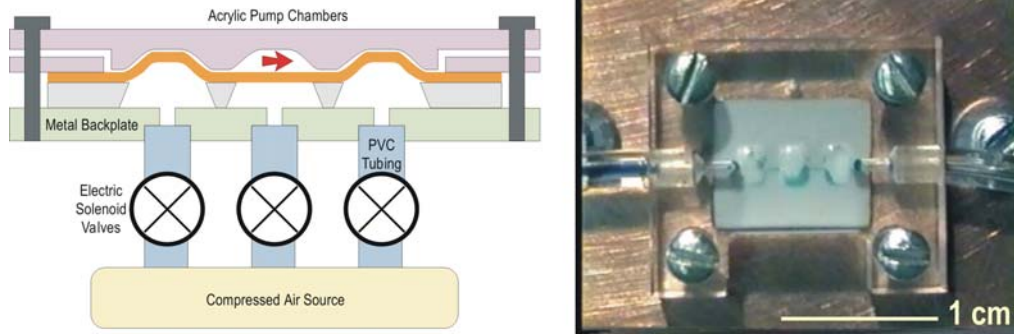


Figure 2-3 A MEMS Peristaltic Pump [9]

2.1.2.2.3 VALVELESS PUMPS

Valveless pumps are similar to diaphragm pumps but do not use check valves to rectify flow. Instead, diffusers or nozzles are used. These elements direct flow such that during the supply mode, more fluid enters through the inlet than exits at the outlet and the reverse occurs for the pump mode (Figure 2-4) [18, 19].

The pressure difference at a diffuser is given by:

$$\Delta p = \frac{1}{2} \xi \rho \bar{v}^2 \quad (2.11)$$

where:

ξ = pressure loss coefficient

ρ = fluid density

\bar{v} = mean velocity at narrowest cross section.

Performance of the diffusers is characterized by the ratio between the pressure loss coefficients in the negative and positive flow directions:

$$\eta = \frac{\xi_{\text{negative}}}{\xi_{\text{positive}}} \quad (2.12)$$

High η is required for good flow directing capability. As suggested by lack of reverse flow blocking elements, valveless pumps are prone to leakage and back flow. It is important to maximize stroke volume and minimize dead volume when designing valveless pumping systems.

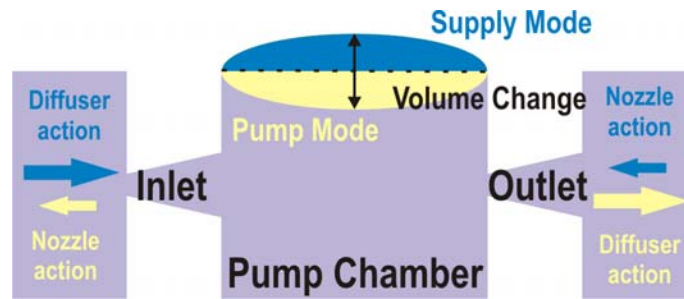


Figure 2-4 Valveless Pump Operation

2.1.2.2.4 ROTARY PUMPS

Rotary pumps potentially can be used to pump viscous fluids at the micro-scale [20, 21]. However, the large loads make an integrated actuator impractical. Also, the complexities involved in fabricating high aspect ratio rotating gears makes these types of pumps unattractive. Although these pumps can potentially be self-priming, leakage effects can prove difficult to overcome during assembly.

2.1.2.3 DYNAMIC PUMPS

Dynamic pumps are further divided into ultrasonic and centrifugal pumps.

2.1.3 NON-MECHANICAL PUMPING SCHEMES

Non-mechanical pumps require the conversion of non-mechanical energy to kinetic energy to supply the fluid with momentum. These phenomena are practical only in the micro-scale. Thus practical flow rates for non-mechanical pumps start at 10 $\mu\text{l}/\text{min}$ and below [7]. Non-mechanical pumps include electrohydrodynamic (EHD) [22, 23], dielectrophoresis [24],

electrokinetic [1, 25], magnetohydrodynamic (MHD) [3, 4], and surface tension driven pumps [26-28].

2.2 DESIGN AND FABRICATION

Mechanical pumping is ideal for operation in presence of particulates, multi phase fluids, and for its immunity to properties of the flow. In the micropump realm, mechanical pumps have been well studied. While diaphragm pumps are somewhat complicated to fabricate, they have the potential to deliver large amounts of flow. The limiting factor is typically the actuator. Micro actuators are restricted to small strokes so to utilize the flow throughput potential of micropumps, external actuators are required. Here, a diaphragm pump with an external actuator is presented. The design aims are to maximize actuator deflection, and thus stroke volume to explore higher flow rates than typically achieved by micropumps (> 1 ml/min).

This diaphragm pump has gone through two iterations of the design process. Significant improvements were made from one generation to the next as individual components were completely redesigned. Micropumps, by nature, are composed of a significant number of components that are difficult to fabricate in a completely integrated manner. Thus, the approach here is to create modular components that can be clamped together to form a pump. This prototyping method facilitates pump characterization.

2.2.1 PARYLENE CHECK VALVES

Check valves are rectifying fluidic elements and share an equivalent function to diodes do in electrical circuits. Ideally, a check valve permits flow when exposed to forward fluid stream and inhibits flow for a reverse one. However, a finite cracking pressure is required to initiate forward fluid flow and most implementations exhibit some amount of reverse leakage flow (Figure 2-5). Another non-ideal behavior is that the valves fail when exposed to sufficiently

large reverse pressures. Various implementations of check valves have been investigated including rectifying structures created from ring mesas [13], cantilevers [29], membranes [30], discs [31], V-flaps [32], and floats [33] (Figure 2-6). These valves are constrained to operate within a specific flow range. This is in large part due to the excessive flow resistance to forward flow experienced across the valve cap and valve seat. As shown in Figure 2-6, MEMS check valves used in micropumps will result in out-of-plane flow. Planar check valves have not been extensively researched and are currently not optimized for use with micropumps [34].

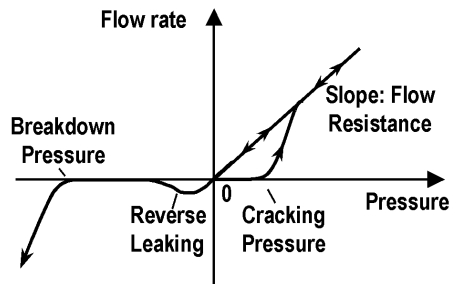


Figure 2-5 Check Valve Behavior [35]

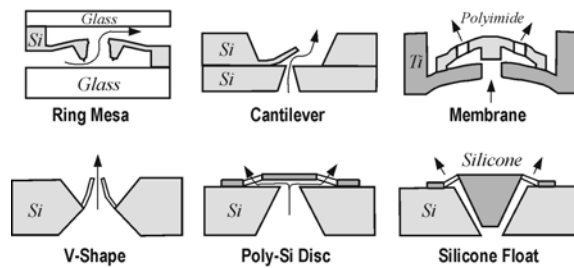


Figure 2-6 Check Valve Types Found in Literature [35]

To reduce the forward flow resistance, an elastic material and appropriate valve cap geometry are chosen. In this approach, parylene C check valves from [36] were used in the first pump design. Large valve cap deflections are possible as parylene has a low Young's modulus (~ 2.8 GPa) and S-shape tethers allow the valve cap two degrees of freedom. Flow resistance and, accordingly, cracking pressure are drastically reduced, as the valve cap is able to rotate and

elevate away from the valve seat (Figure 2-7). In addition, reverse leakage is extremely low as valve-cap-to-valve-seat sealing is excellent and high reverse pressures can be tolerated. The overall performance is further enhanced by the immunity to stiction and surface tension effects. However, since these check valves were fabricated on the same side of the wafer, they are only able to rectify flow in one direction. In order to construct a pump from these valves, complicated assembly was required to separate individual valves and glue them, facing in opposite directions, to a Plexiglas structural support. As a result, in the second design, check valves were fabricated using a process modified from [36] to create a double-sided valve chip (Figure 2-8). In addition, linear arrays of check valves were also fabricated using the same process.

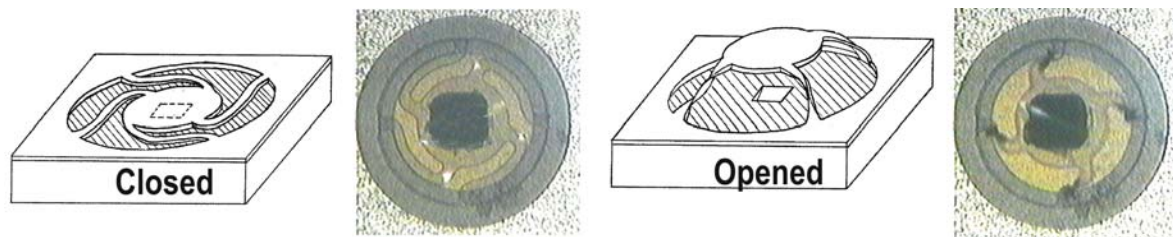


Figure 2-7 Parylene S-Tethered Check Valve Operation [35]

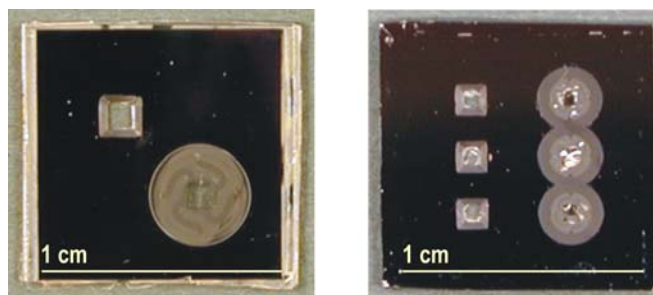


Figure 2-8 Two Types of Fabricated Double Sided Check Valves

2.2.1.1 PARYLENE FUNDAMENTALS

Parylene is the generic name for a family of unique vapor phase deposited thermoplastic polymers. Its ability to form continuous, pinhole free conformal coatings at room temperature

and biocompatibility are factors in its increasing popularity as a MEMS material. Excellent dielectric properties have resulted in extensive use of parylene in semiconductor processing as well. Three kinds of parylene are available commercially and each material has slightly different properties for flexibility in application (Figure 2-9). A comparison of parylene N, C, and D is shown in Table 2.2. Parylene C is the most commonly used form for its useful combination of physical and electrical properties.

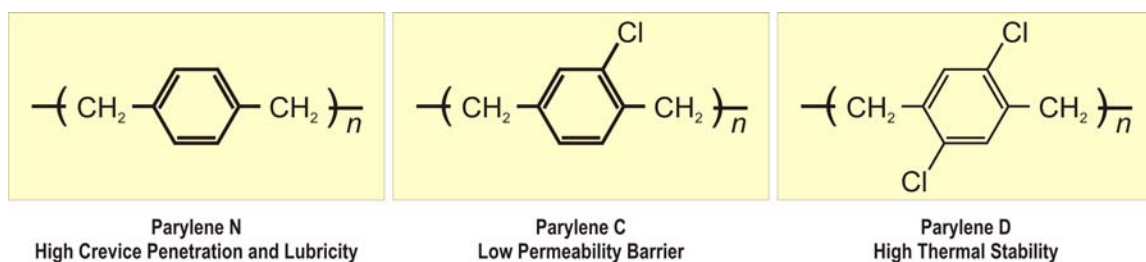


Figure 2-9 Types of Commercially Available Parylene

Table 2.2 Physical and Thermal Properties of Parylenes [37]

Property	Parylene N	Parylene C	Parylene D
Young's Modulus (GPa)	2.4	2.8	2.6
Tensile Strength (MPa)	41–76	69	76
Yield Strength (MPa)	42	55	62
Elongation (%)	20250	200	10
Yield Elongation (%)	2.5	2.9	3.0
Rockwell Hardness	R85	R80	R80
Melting Point (°C)	420	290	380
Linear Coefficient of Expansion (/°C)	6.9×10^{-5}	3.5×10^{-5}	$3-8 \times 10^{-5}$
Thermal Conductivity (cal/(cm · s · °C))	3.0×10^{-4}	2.0×10^{-4}	–
Specific Heat (cal/(g · °C))	0.20	0.17	–

2.2.1.2 PARYLENE PROCESSING

Parylene was discovered by Michael Mojzesz Swarc at the University of Manchester in 1947. Later, in the 1950's, research to develop a commercial parylene deposition process was initiated by William F. Gorham of the Union Carbide Corporation. A coating system was finally introduced to the market in 1965. Although only three kinds of parylene are commercially available, it is interesting to note that Union Carbide developed over 20 different types [38]. The finalized synthetic process involves the vapor phase deposition of parylene from its dimer form (Figure 2-10). The dimer (di-para-xylylene) is a stable compound that comes in granular form.

The first step of the deposition process vaporizes the dimer at 150 °C. Then pyrolysis occurs causing the dimer to be cleaved into a monomer radical (para-xylylene). This monomer adsorbs and polymerizes when it reaches the room temperature deposition chamber. The deposition rate of parylene C is about 5 μm/hr. All depositions of parylene were performed using the PDS 2010 Labcoter® 1 from Specialty Coating Systems.

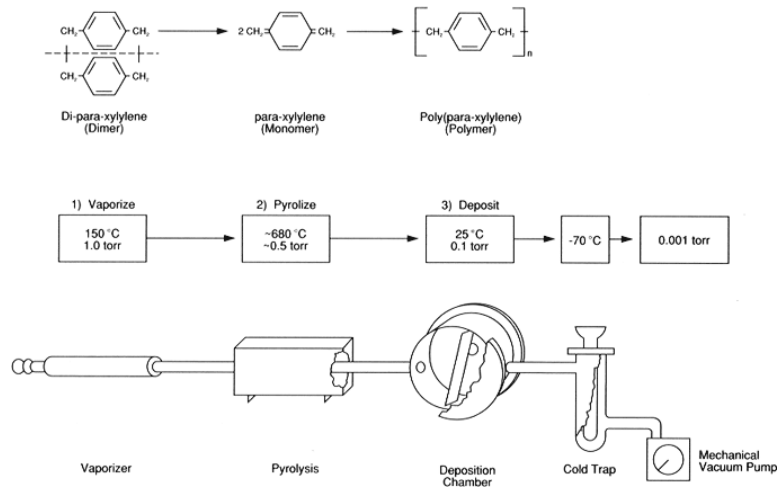


Figure 2-10 Parylene Deposition Process [37]

A convenient feature of parylene is that it integrates well into MEMS processes. Oxygen plasma etching conveniently patterns the material using either an Al or photoresist masking layer. In addition, adequate adhesion to silicon and silicon oxide are achieved by applying a special adhesion promoter (A-174) prior to deposition.

2.2.1.3 PARYLENE CHECK VALVE FABRICATION

The fabrication process starts with a thermally oxidized (1.5 μm thick) silicon wafer (Figure 2-11). This layer serves as a simply etching mask. The first structural feature to be defined is the orifice. However, as subsequent processing is necessary in these areas to form the valve cap, only a cavity is etched and not a through hole. Cavities are etched using KOH. The remaining 20 μm thick silicon membrane serves as a structural support on which to build the check valves. A circular region of silicon is then exposed to BrF_3 gas for the purpose of roughening the surface via etching [39]. This roughened silicon surface serves two purposes: (1) it prevents stiction of the parylene tethers to the substrate and (2) it enhances the adhesion of the anchored portions of the parylene tethers to the silicon substrate by increasing the contacted surface area (Figure 2-12). A-174 adhesion promoter is applied and followed by the deposition of a 2 μm layer of parylene-C. This layer is patterned in oxygen plasma to form a circular support ring for the valve cap layer. Then a sacrificial photoresist layer (5 μm of AZ 4400) is spun and patterned to separate the valve cap from the valve seat. To prevent check valve failure due to mechanical failure from stresses experienced at sharp corners, the photoresist is hard baked to round off the convex corners as depicted in Figure 2-13. A second layer of parylene (3 μm) is deposited and masked with a 1000 \AA layer of thermally evaporated aluminum. This Al masking layer was replaced with thick photoresist (10 μm of AZ 4620) in the double-sided process to avoid exposing the photoresist and parylene layers to

the high temperatures of the thermal evaporation process. To release the check valves, the 20 μm silicon layer between the eventual orifice and sacrificial photoresist layer is etched away in BrF_3 gas. After dicing, the Al/photoresist masking layer and sacrificial photoresist layer are removed to complete the fabrication process. Various views of the fabricated check valves are shown in Figure 2-8 and Figure 2-14.

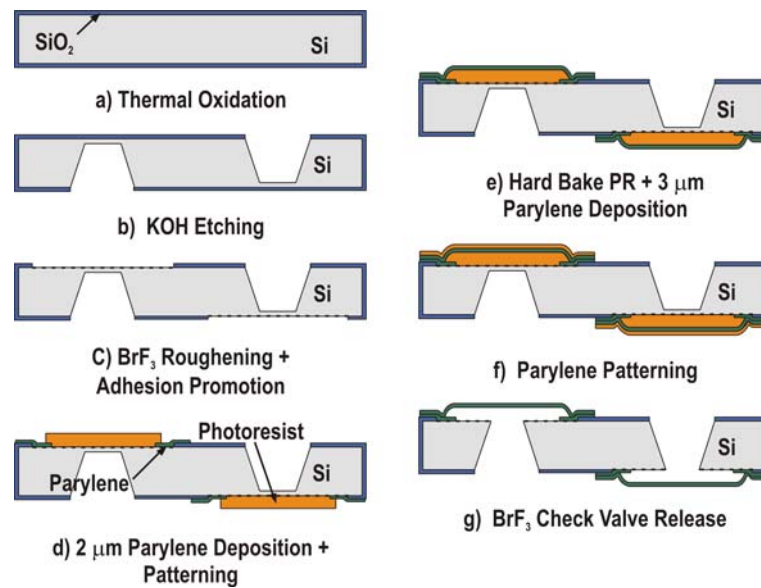


Figure 2-11 Double Sided Check Valve Fabrication Process

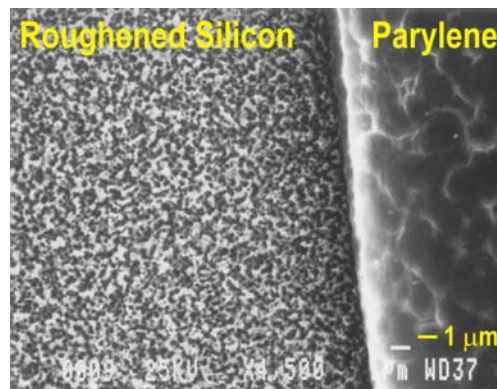


Figure 2-12 BrF_3 Roughened Silicon

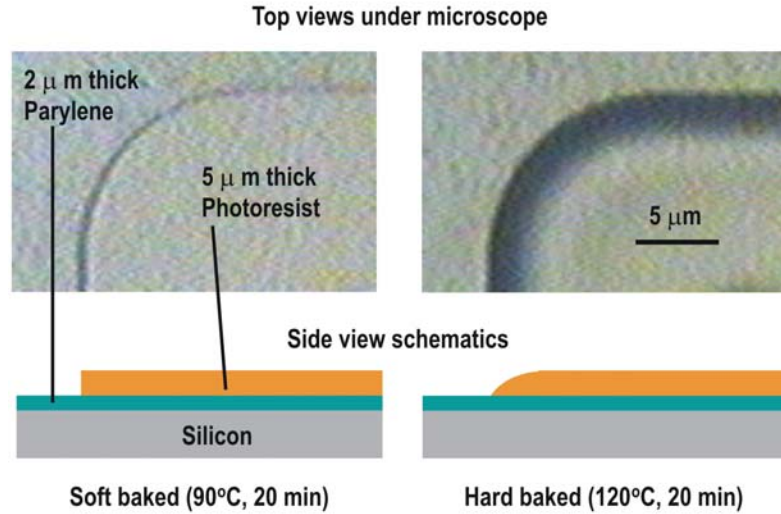


Figure 2-13 Rounded Photoresist Step After Hard Baking

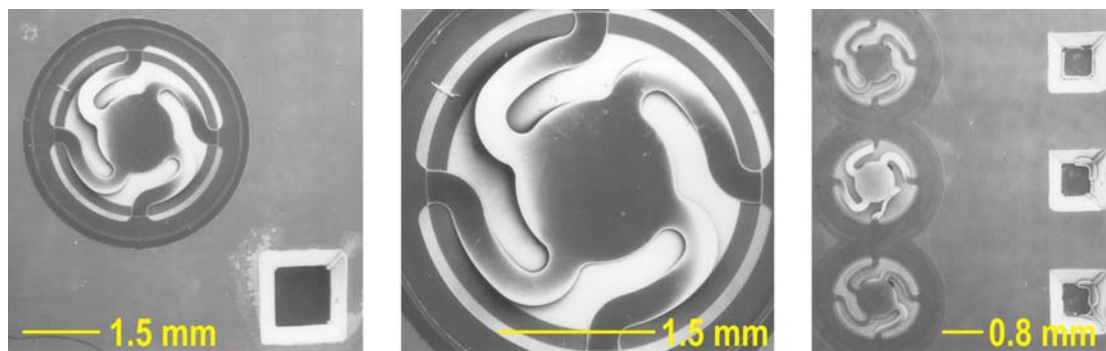


Figure 2-14 SEMs of Fabricated Check Valves

2.2.2 SILICONE RUBBER PUMPING MEMBRANE

Desired properties of pumping membranes are large deflection and good sealing. In addition, to improve the achievable compression ratio, a material that will allow the deflected membrane to efficiently match and conform to the pumping chamber geometry is needed. Silicone rubber has low Young's modulus and durometer, as well as high elongation. These properties make it an excellent choice for this task.

2.2.2.1 SILICONE RUBBER FUNDAMENTALS

Silicone is a general term that refers to a diverse class of partially organic polymers that can be found in multiple forms including elastomers, resins, and liquids. The most notable difference of silicone from most polymers is that it is formed from a silicon-based backbone, not a carbon one. This contributes to the excellent chemical stability and electrically insulating properties valued in this family of materials. Structurally speaking, silicone is composed of a chain of alternating silicon and oxygen atoms (a polysiloxane chain) with hydrocarbon radicals occupying the remaining silicon valences (Figure 2-15). The radical is typically a methyl group ($-\text{CH}_3$) as in polydimethylsiloxanes (PDMS).

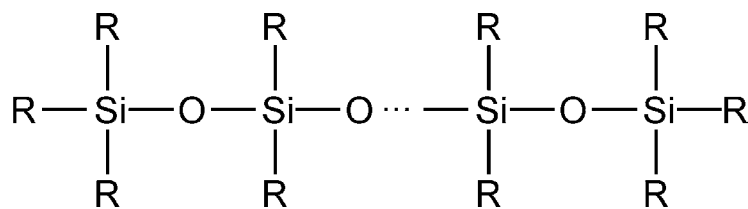


Figure 2-15 A Linear Polysiloxane Chain

The particular type of silicone chosen for the pumping membrane is MRTV1-10E. This is manufactured by Insulcast, a division of American Safety Technologies, and is a room temperature vulcanizing (RTV), addition cure mold making silicone rubber. This particular formulation has a 10% reactive fluid dilution, which has been found to facilitate its application via spin coating and exhibits good adhesion to silicon and silicon nitride [40]. Typical physical parameters are given in Table 2.3. Addition cure vulcanized silicone rubber typically starts as a two-part mixture consisting of a base and curing agent. The curing agent contains a crosslinker. By slightly altering the amount of crosslinker applied in a mixture, the physical properties of the cured silicone can be modified. The recommended mixing ratio for MRTV1-10E is 10 parts of the base to one part of the curing agent.

Table 2.3 Physical Properties of MRTV1 and Sylgard 184

Manufacturer and Product	Durometer, Shore A	Tensile Strength (psi)	Tear Strength (lb./in)	Elongation (%)	Color	Viscosity (cps)
Insulcast MRTV1	40	1030	15	140	Transparent	4000
Dow Corning Sylgard 184	24	500	125	1000	White	60000

2.2.2.2 SILICONE RUBBER PROCESSING

The manufacturer recommended preparation procedure for MRTV1 is outlined in Table 2.4.

Table 2.4 Silicone Preparation Procedure

1. Premix the base and curing agent to reincorporate any settled filler.
2. Weigh parts accurately allowing for one part of catalyst for each 10 parts of base.
3. Mix thoroughly, scraping the container sides and bottom to ensure a homogeneous mixture.
4. Degas the mixture by placing in a vacuum chamber. Draw about 29 inches of mercury allowing the mixture to rise about 3-4 times its original volume and then collapse. Maintain the vacuum for another minute or two and then vent.
5. Apply the pre-cured silicone.
6. Cure at room temperature (25°C) for 16-24 hours or apply heat (3-4 hours at 50°C or 1-2 hours at 65°C) for quicker curing.

2.2.2.3 SILICONE MEMBRANE FABRICATION

Incorporating the mixed silicone rubber precursor into a microfabrication process presents a challenge. The material itself is both difficult to pattern via photolithography or etch after curing. Also, the surface is inert and adhesion to most materials is poor. Special effort must be expended to create silicone rubber structures. Given that adhesion may be compromised during the long processing times required to create bulk micromachined membranes, the most straightforward way to form a silicone membrane is shown in Figure 2-16. Here, a wafer is thermally oxidized (1.8 to 2.0 μm thick) to provide an etch mask. After patterning the masking layer on the backside of the wafer, a thin silicon membrane (10 to 20 μm thick) is formed by etching in KOH. Oxide is stripped on the front side of the wafer, providing a silicon surface

for adhesion to MRTV1. Silicone is spun on this surface and then the entire structure is cured. The remaining silicon is etched away via RIE (reactive ion etching) in a SF_6/O_2 plasma to free the membrane. Alternatively, a silicon nitride masking layer can be used.

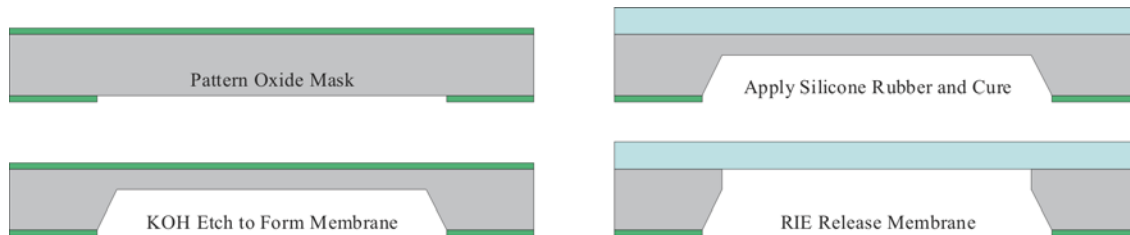


Figure 2-16 A Simple Silicone Membrane Process [40]

A refinement on the above process is shown in Figure 2-17. In this modified process, pillars are integrated in the membrane layer to control the compression of the rubber layer when exposed to clamping force. This process also avoids thickness control difficulties encountered when applying the silicone in a spin coating process. The pillars are formed during an additional patterning step followed by KOH etching. The masking material can be identical to the one used in forming the silicon membrane. Instead of spin coating, the silicone layer is applied by casting. Membranes created using this technique measure $7 \times 7 \text{ mm}^2$ and are $80 \mu\text{m}$ thick. One is shown in Figure 2-18.

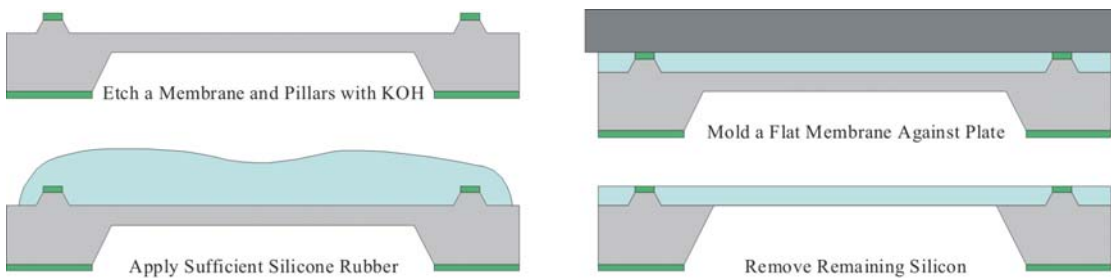


Figure 2-17 Process Flow for Silicone Membrane with Pillars [40]

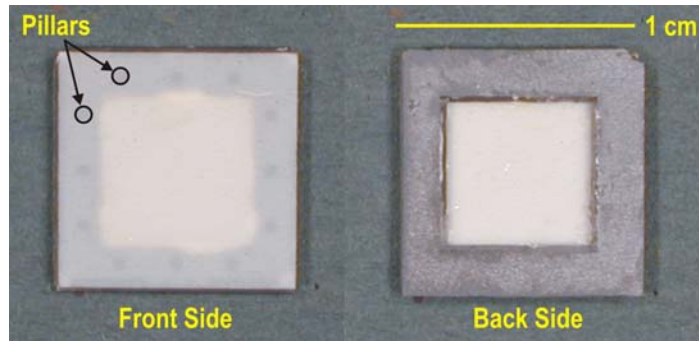


Figure 2-18 Fabricated Silicone Membrane with Pillars

The previous processes all result in square membranes due to the anisotropic etching of silicon. In order to achieve a circular geometry, it is necessary to use deep reactive ion etching (DRIE) to produce the membrane. Circular pumping membranes are able to achieve better compression ratios and thus better pump performance. DRIE is also ideal for creating circular bosses. Bossed membranes can further improve pumping efficiency. Wet anisotropic etching would require complicated mask geometries to achieve a similar structure.

The process flow for fabricating circular silicone membranes is shown in Figure 2-19. Thick photoresist (AZ 4620) is spun and patterned to define the membrane. Thermal oxide can also be used as a mask, however, there is an additional step required to remove the front side oxide prior to the application of silicone. A brief descum in oxygen plasma followed by an HF dip (10 % hydrofluoric acid) is necessary to prevent micrograss formation during DRIE etching. Wafers are then etched via DRIE until a thin silicon membrane ($\sim 20 \mu\text{m}$ thick) remains. Silicone rubber is spun on the backside at 1 krpm for 80 seconds to yield an approximately $140 \mu\text{m}$ thick membrane layer when cured. The remaining silicon is etched away via RIE (reactive ion etching) in a SF_6/O_2 plasma. Circular diaphragms with and without bosses (5, 6, and 7 mm in diameter) and measuring 8 mm in diameter were created using this procedure. They are shown in Figure 2-20.

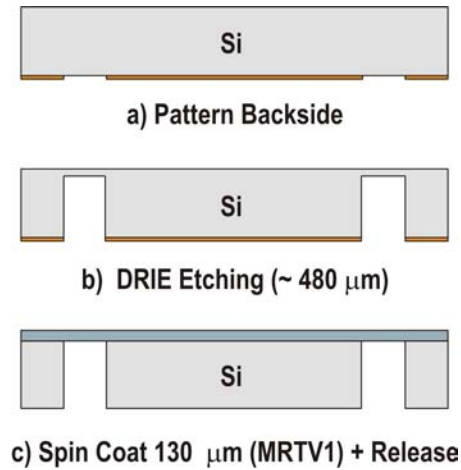


Figure 2-19 Circular Silicone Membrane Fabrication Process

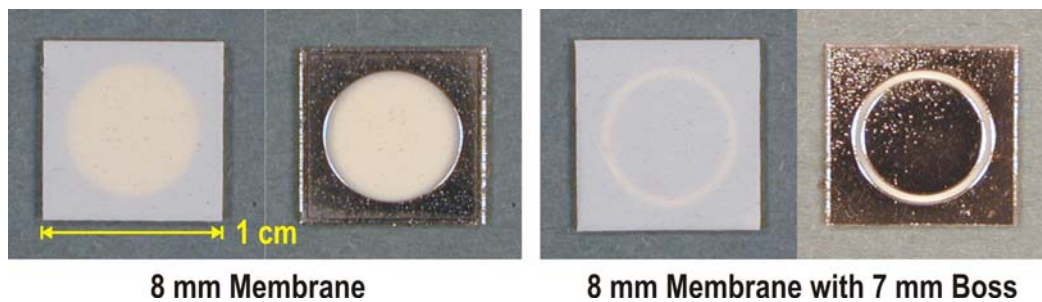


Figure 2-20 Fabricated Circular Membranes

2.2.3 SILICONE RUBBER GASKETS

As previously mentioned, silicone rubber is a suitable material for sealing purposes. Several levels of silicone gaskets were fabricated in the second pump design to seal the assembled pump and serve as spacers. The physical properties of the silicones used are presented in Table 2.3

2.2.3.1 CHECK VALVE TO PUMP SEAT GASKET

Silicone gaskets were introduced in the second pump to seal the check valves to the pump seat. A molding technique is used to create gaskets whereby silicone is molded into a DRIE etched silicon master, cured, and then release from the mold (Figure 2-21). The gasket is designed so as to be self-aligning; cylindrical pegs in the gasket fit pits that are machined into

the Plexiglas pump seat. 10 μm of photoresist (AZ 4620) is spun and patterned to define the alignment pegs. After a brief descum in oxygen plasma and an HF dip, the wafer is etched to a depth of $\sim 300 \mu\text{m}$ via DRIE. A second lithography (10 μm AZ 4620), descum, and HF dip are performed to define the gasket boundaries. Both features are etched together to establish the thickness of the gasket ($\sim 100 \mu\text{m}$) and finalize the height of the pegs ($\sim 400 \mu\text{m}$). Prior to silicone molding, a mold release layer of Parylene or plasma deposited Teflon (CHF_3) can be applied. Sylgard 184 is used for its transparency. Molding is achieved by filling the mold with a layer of silicone precursor and using a flat blade to squeegee the excess material away. This technique is similar to a molding technique used in fabricating valve membrane elements in [41]. The mating alignment structures between the pump seat and gasket can be seen in Figure 2-22.

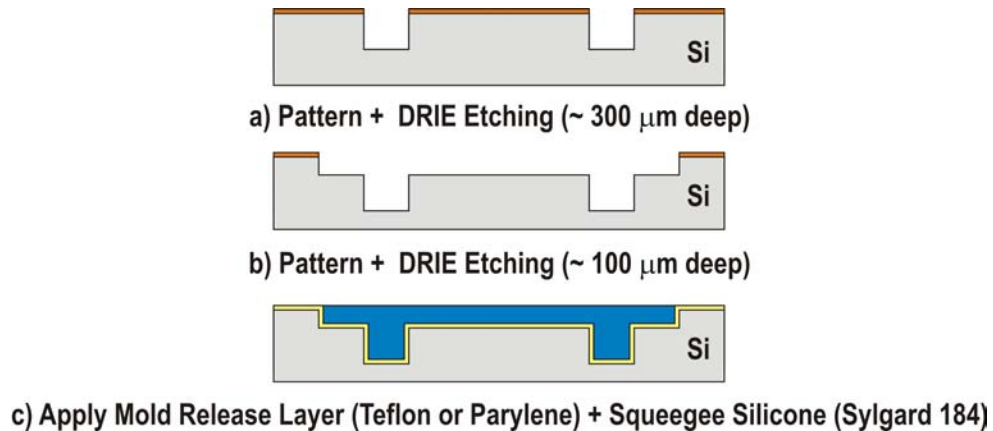


Figure 2-21 Silicone Gasket Fabrication Process

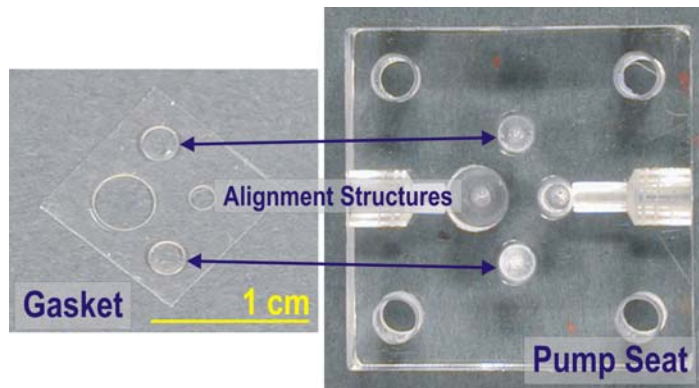


Figure 2-22 Alignment Structures on a Fabricated Gasket and Machined Pump Seat

2.2.3.2 CHECK VALVE TO PUMP CHAMBER GASKET

One complication in using check valves with large cap deflections in a diaphragm pump is that additional structural layers are necessary to prevent damage to the check valves. To prevent silicone membranes from adhering to the check valves during pump operation, a conventionally machined Plexiglas spacer was included in the second pump design. This, however, creates the need for another silicone gasket to seal the spacer to the check valve chip (Figure 2-23). Taking into account the gasket thickness requirement based on the Plexiglas spacer thickness and additional height required to prevent membrane-check valve contact ($> 500 \mu\text{m}$), it is impractical to use a silicon wafer as the mold master for this gasket. Therefore, these gaskets were molded from precision milled Delrin masters. Delrin is similar to Teflon and thus no mold release layer is required. Sylgard 184 was used again for its transparency and applied in exactly the same manner as described for the check valve to pump seat gasket. For the check valve array case, it is difficult to make a machined master for due to tight spacing. Large openings for the check valve array were machined into the master so through holes for the orifices had to be cut by hand using an X-acto knife.

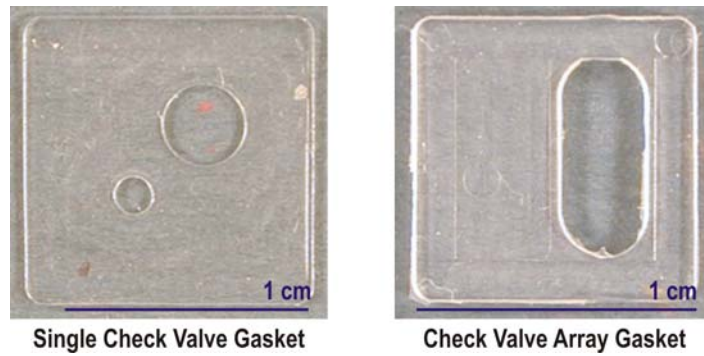


Figure 2-23 As-Molded Silicone Check Valve to Pump Chamber Gaskets

2.2.3.3 PUMP CHAMBER SPACER AND GASKET

The first generation spacer is simply an $8 \times 8 \text{ mm}^2$ orifice etched through a silicon substrate via KOH. The front side is glued to the pump body and the backside is clamped to the pump membrane. Second generation pump spacers are conveniently formed by carefully cutting out the released circular membrane portion of the membrane chips (Figure 2-24). They serve to seal the pumping chamber from leaks as well as define the height of the chamber.

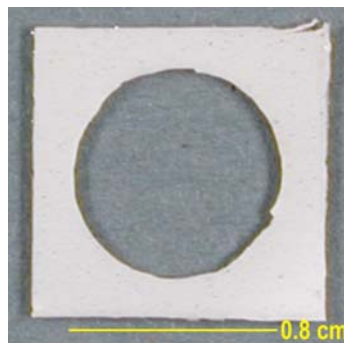


Figure 2-24 Circular Pump Chamber Spacer and Gasket

2.2.4 EXTERNAL ACTUATORS

The choice to go with an external actuator in this design can be understood by evaluating the current state of art in micro actuator technology. The deflections desired are on the order of the thickness of the silicone substrate ($\sim 500 \mu\text{m}$). Thus it is not practical to use a micro

actuator based on the discussion earlier. Ideally, the actuator should have a maximum vertical deflection of 500 μm over a wide range of frequency.

2.2.4.1 SOLENOID VALVE CONTROLLED PNEUMATIC ACTUATION

Pneumatic actuators are a possibility as the membrane deflection is not physically limited by actuator travel but by the pumping chamber dimensions. Hence, it is useful to characterize the pump using pneumatic actuation. An external compressed air source and a Clippard ETO-3-6 three-way solenoid valve are connected together to supply bursts of pressurized air to the pump. One major drawback of this method is that the restoring force experienced by the membrane is solely due to the physical properties of the material from which it is made.

2.2.4.2 SOLENOID PLUNGER ACTUATOR

Another possibility is to use a solenoid actuator. A modified version of the solenoid found in [42] can be made to give deflections of $\sim 250 \mu\text{m}$ (Figure 2-25). The solenoid actuator contains a plunger that is made to produce a reciprocating motion when the supply current to the solenoid is turned on and off (Figure 2-26). The plunger is fully extended when no power is applied by a spring element in the body of the solenoid. When the coil is supplied with current, the induced magnetic field creates a force that retracts the plunger into the body. Thus, in this manner, the restoring force is not completely dependent on the membrane material properties. The plunger can also be outfitted with various tips (Figure 2-27). Special tips were machined conventionally for both generations of pump designs.

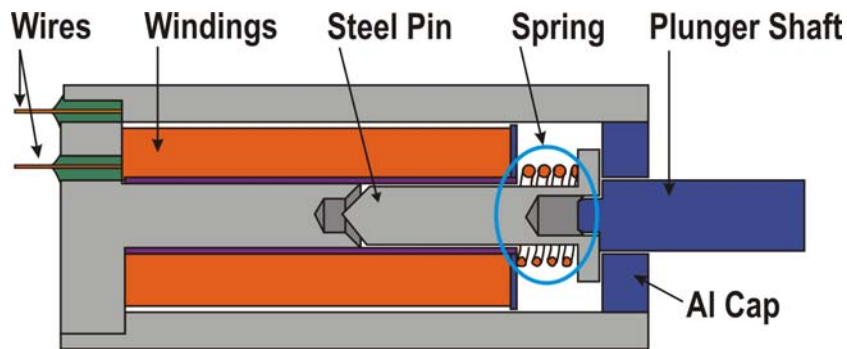


Figure 2-25 Cross Section of Solenoid Actuator

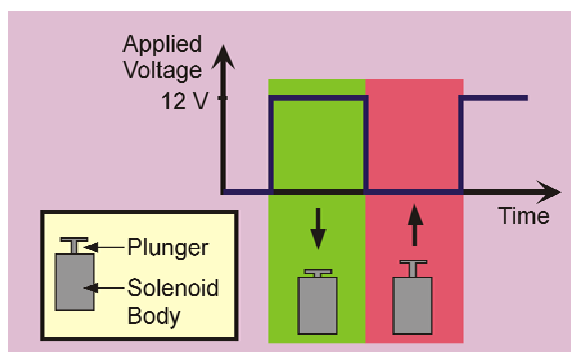
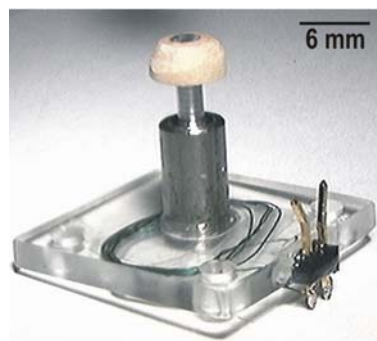
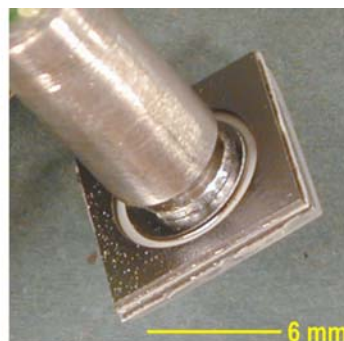


Figure 2-26 Solenoid Actuation Scheme



Rounded Wooden Tip



Flat Al Tip Bonded to Si Boss

Figure 2-27 Two Types of Tips Used on the Solenoid Actuator

2.2.5 ASSEMBLY AND PACKAGING

Pump prototype assembly involves the use of Plexiglas pump seats in addition to a combination of gluing and clamping. The first generation pump was constructed by gluing the component chips together. As this makes it difficult to assemble and repair, the second

generation was designed to eliminate the need for glue by taking advantage of the sealing property of silicone rubbers. Alternating layers of silicone and silicon allowed the pump to be watertight when clamped.

The first generation pump was assembled through a combination of clamping and gluing (Figure 2-28). The membrane chip was glued to a Plexiglas plate and clamped to the rest of the pump, which consisted of chips stacked and glued together. Tygon tubing was connected to the input and output to facilitate testing. A solenoid actuator was then properly positioned beneath the membrane.

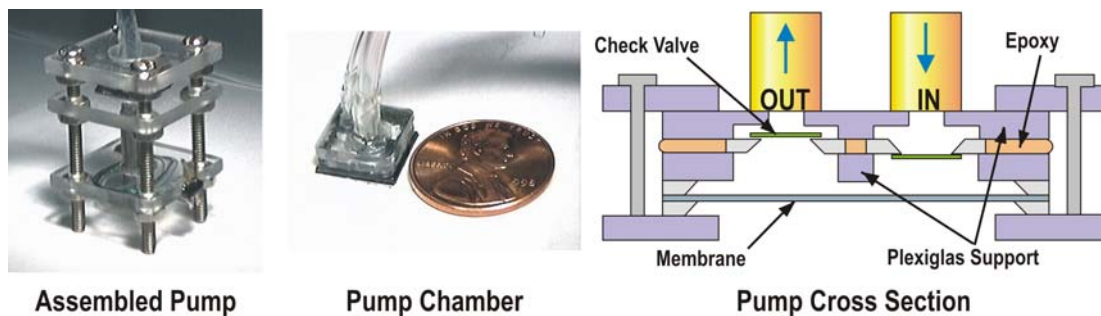


Figure 2-28 Various Views of the 1st Generation Solenoid Driven Pump

The second generation pump was entirely clamped and only required adhesive to connect the tubing and actuator to the packaging (Figure 2-29 & Figure 2-30). This modular design allows easy access to and replacement of individual components. Two different pump seats were precision milled from Plexiglas for the two different check valve configurations. Plexiglas backing plates allowed the pump to be clamped together and provided a means for attaching the actuator. A different backing plate was used during pneumatic testing to allow for attachment to the solenoid valve.

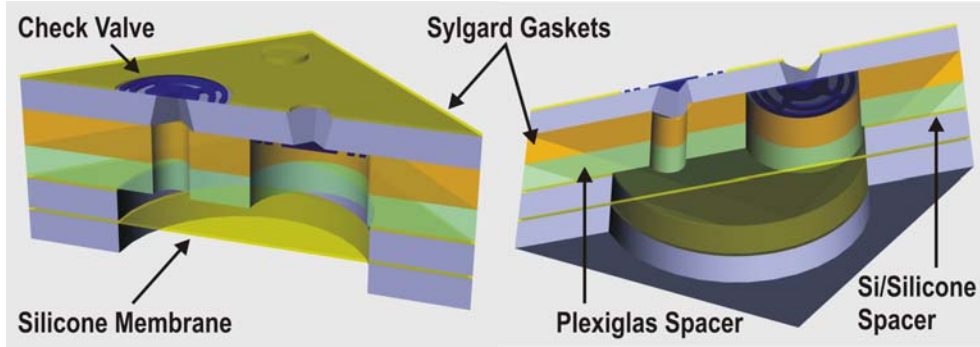


Figure 2-29 Clamped Pump Chamber Structure

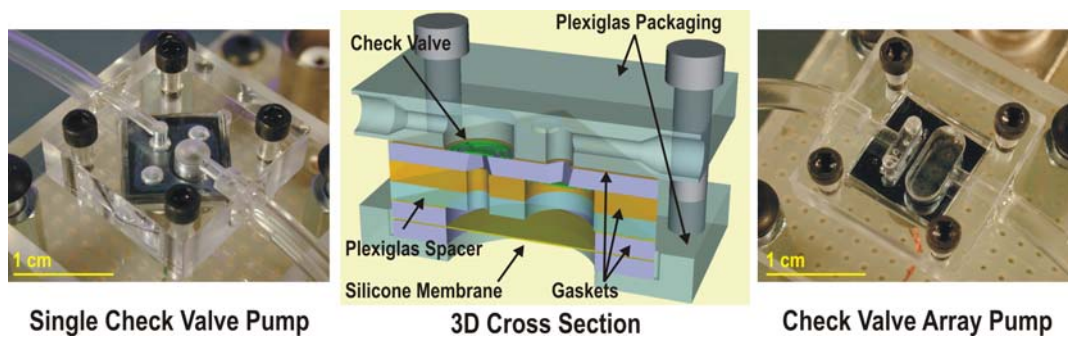


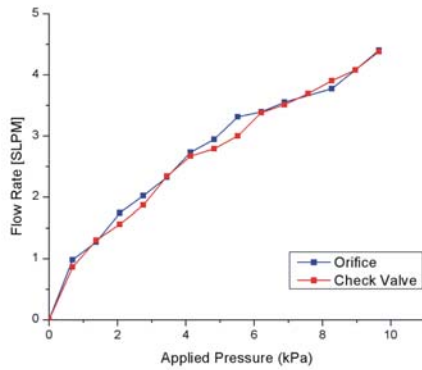
Figure 2-30 Various Views of Clamped Pumps

2.3 PUMP CHARACTERIZATION

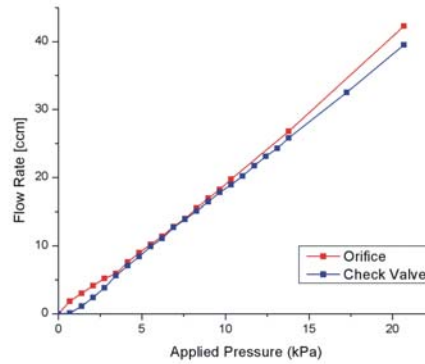
2.3.1 CHECK VALVE PERFORMANCE

Check valves (orifice dimensions of $780 \mu\text{m} \times 780 \mu\text{m}$) used in the first generation pump have been thoroughly tested and analyzed in [36]. Performance of the double-sided check valves was characterized for both air and water. Flow rate versus applied pressure plots with the check valve in place and removed (orifice only) were obtained (Figure 2-31). As shown in [36], the twist-up tether configuration of the check valves allows for enough deflection to achieve nearly atmospheric pressure at the exit. Thus, flow resistance induced by the valve cap is negligible. In comparison to valves of similar size designed with straight tethers, the membrane deflection owing to S-shaped tethers can be up to four times as high. Check valve cracking pressures were below sensor resolution and therefore unknown. As expected, the

BrF_3 roughened silicon surface underneath the valve cap inhibits stiction and surface tension effects from interfering with valve performance.

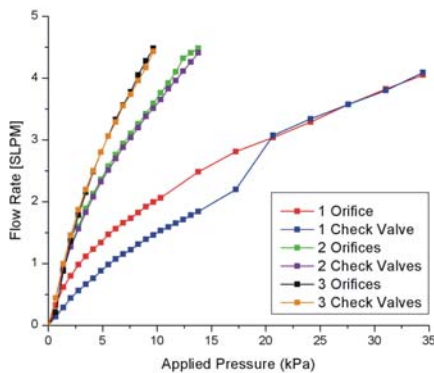


Air Testing Results

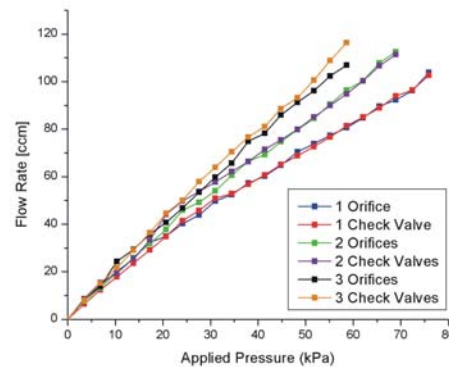


Water Testing Results

Figure 2-31 Single Check Valve Testing Results



Air Testing Results



Water Testing Results

Figure 2-32 Check Valve Array Testing Results

Check valve arrays, consisting of an inlet and outlet with three individual check valves each, were also characterized. Figure 2-32 shows the flow rate increase as the number of check valves was increased. It is evident from Figure 2-33 that a slight advantage in performance for water flow was observed in the array case. The orifice dimensions for the solitary input/outlet

check valves are $770 \mu\text{m} \times 770 \mu\text{m}$ and for each of the check valves in the array, $370 \mu\text{m} \times 370 \mu\text{m}$. Effective orifice areas are $5.93 \times 10^{-3} \text{ mm}^2$ and $4.11 \times 10^{-3} \text{ mm}^2$, respectively. Thus, a check valve array is preferred over a single check valve design to maximize flow rates and decrease flow resistance.

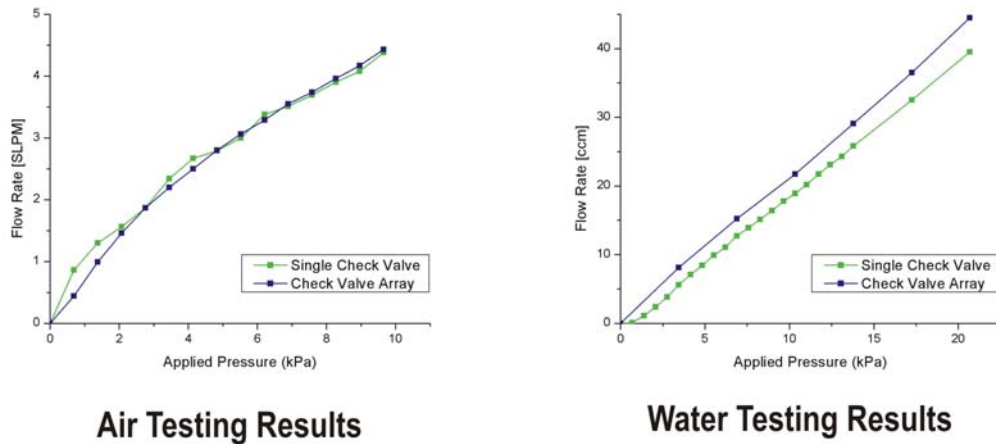


Figure 2-33 Comparison of Check Valve Schemes

2.3.2 PNEUMATIC ACTUATION EXPERIMENTS

Pneumatic actuation was utilized to verify the design of the second generation pump (Figure 2-34). Bursts of compressed air are supplied to control the deflection of the pumping membrane by turning on and off a three-way solenoid valve. This pattern of actuation can achieve pumping action.

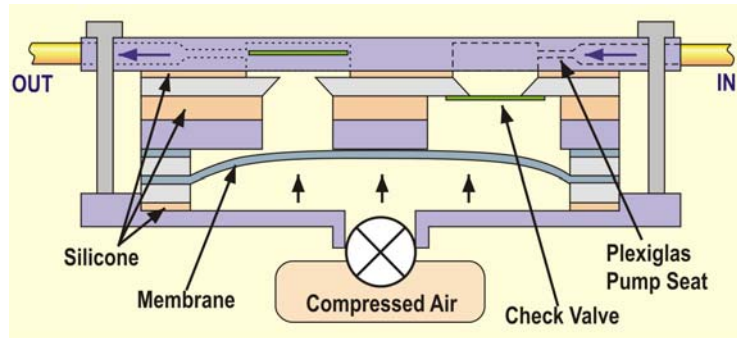
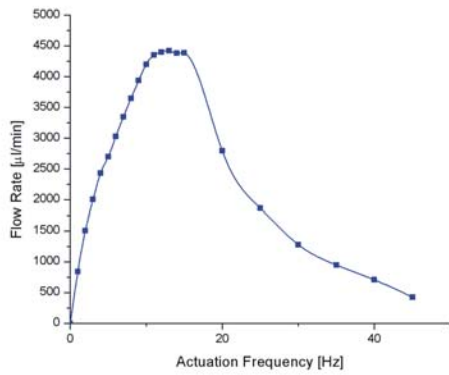
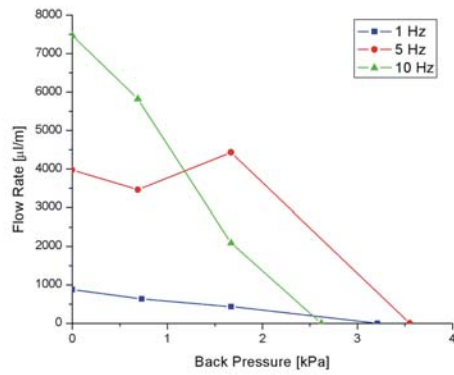


Figure 2-34 Pneumatic Testing Fixture Schematic

Both check valve schemes were tested using an inflation pressure of 6.9 kPa that is regulated by the solenoid valve. The flow rate of deionized water was determined by timing the passage of a bubble through a calibrated pipette downstream from the pump outlet. A maximum flow rate of 4.4 $\mu\text{l}/\text{min}$ at 13 Hz and back pressure of 3.6 kPa at 5 Hz were possible with the single inlet and outlet design (Figure 2-35). A nearly threefold increase in achievable flow rate of 13 $\mu\text{l}/\text{min}$ at 11 Hz and back pressure of 5.9 kPa at 5 Hz were made possible by the array pump (Figure 2-36). Thus, the check valve array pump outperformed the single check valve pump in both categories. Nonlinear behavior in the flow rate dependency on frequency was observed. This is expected as the silicone membrane takes a finite time to return to its original, relaxed position after being deflected. When the frequency of air bursts increases beyond the necessary relaxation time of the membrane material, the efficiency of the pump decreases dramatically. This validates the need for an additional restoring force to operate the pump at higher frequencies and to achieve higher flow throughputs. It is unfortunate that pneumatic actuation cannot be easily optimized to overcome these problems as it provides the best means of attaining the maximum possible stroke volume, which in turn would lead to the best possible compression ratio. No other means of actuation currently available can provide these features.

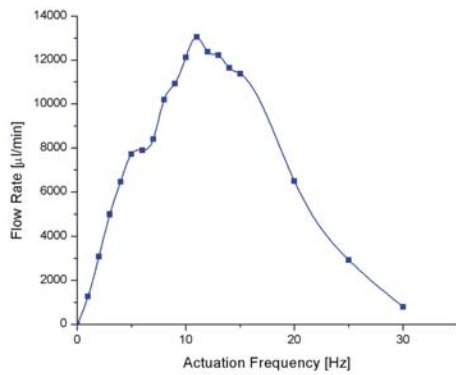


Flow Rate vs. Actuation Frequency

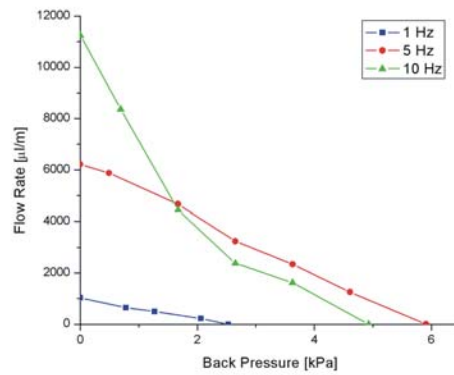


Flow Rate vs. Back Pressure

Figure 2-35 Pneumatic Testing Results of Single Check Valve Pump



Flow Rate vs. Actuation Frequency



Flow Rate vs. Back Pressure

Figure 2-36 Pneumatic Testing Results of Check Valve Array Pump

2.3.3 MECHANICAL ACTUATION EXPERIMENTS

Solenoid actuation produces a reciprocating motion in which an integrated plunger is retracted and extended as current is turned on and off, respectively. By using the plunger to deflect the silicone membrane repeatedly, water pumping is achieved. During solenoid based actuation tests of the micropumps, the actuator was driven using an 11 V square wave signal at various frequencies. This translates into a power consumption of about 700 mW. An assembled pump in its testing jig is shown in Figure 2-37. A BNC receptacle and switch are provided for

control of and connection to a power source. Again, the flow rate of deionized water was determined by timing the passage of a bubble through a calibrated pipette downstream from the pump outlet. Flow rate versus frequency and back pressure plots are displayed in Figure 2-38. This pump is not self-priming and so careful priming is necessary to achieve optimal performance. As expected, flow rate is highly dependent on actuation frequency and is approximately linear for low frequencies. However, above 10 Hz, this linear relationship is lost as the membrane is unable to respond at the speed at which the plunger is actuated. The maximum achievable flow rate was $3.4 \mu\text{l}/\text{min}$ at 10 Hz and maximum sustainable back pressure was 2.1 kPa which occurs for both 10 and 20 Hz.

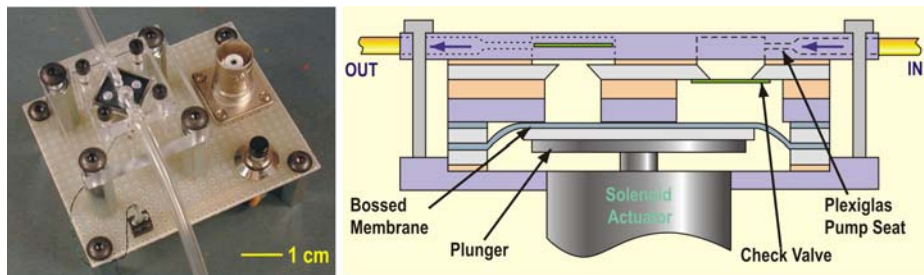


Figure 2-37 Solenoid Actuated Pump Testing Fixture and Schematic

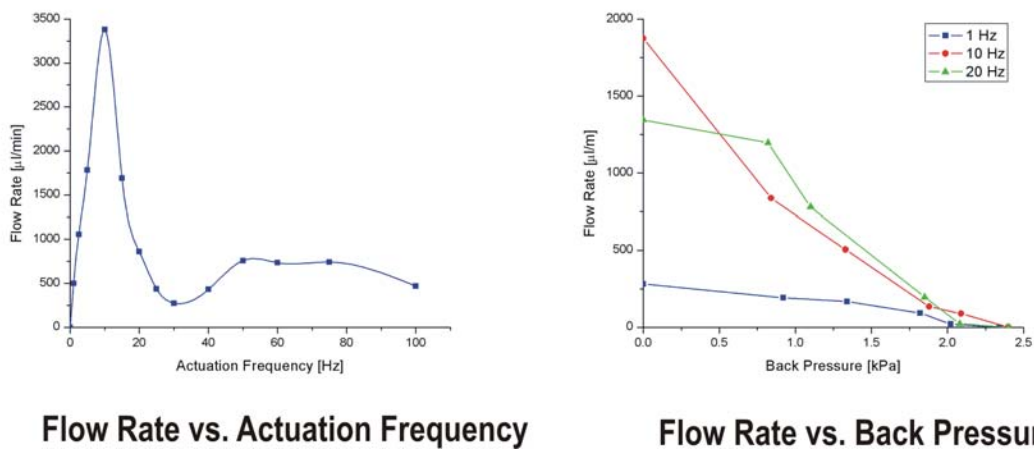
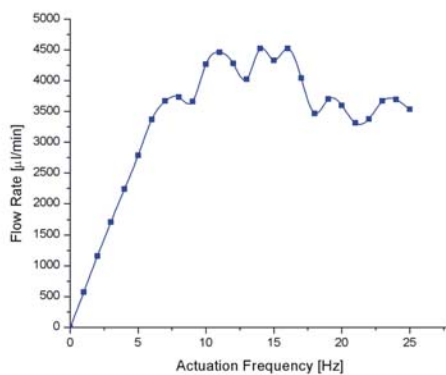
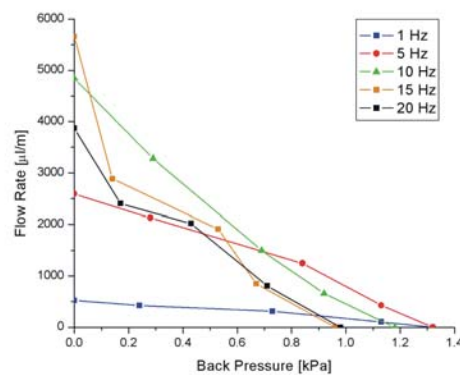


Figure 2-38 Solenoid Actuation Testing Results of Single Check Valve Pump

To eliminate the fall off in flow rate at high frequencies, it is necessary to physically connect the actuator to the pumping membrane. This provides an additional restoring force to pull the membrane back to its relaxed state after being actuated. Thus, a new membrane with a circular silicon boss structure (7 mm in diameter) was implemented in the second design. The surface of cured silicone is inert and not easily bonded to. In order to physically connect the plunger of the actuator to the pumping membrane, a boss structure is necessary. Figure 2-27 shows a 7mm silicon boss is glued to a flat aluminum plunger. The improvement in flow rate versus frequency performance for the single inlet/outlet pump is shown in Figure 2-39. As expected, the flow rate vs. frequency relationship is linear at lower actuation frequencies, and at a critical frequency, the flow rate levels off as it is limited by the maximum fluid flow that can be supplied by the check valves. The additional load placed on the actuator from the physical coupling to the silicone membrane probably affects the pump output to some extent. A maximum flow rate of 4.5 $\mu\text{l}/\text{min}$ at 14 Hz was possible in this configuration. However, the maximum back pressure decreased slightly to 1.32 kPa at 1 and 5 Hz.



Flow Rate vs. Actuation Frequency



Flow Rate vs. Back Pressure

Figure 2-39 Solenoid Actuation Testing Results of Single Check Valve Pump with Bossed Membrane

2.4 DISCUSSION

Table 2.5 summarizes the results of all the pump configurations tested.

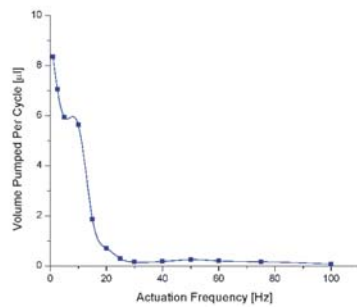
Table 2.5 Summary of Pump Testing Results

Parameter	Symbol	Pump 1	Pump 2	Pump 3	Pump 4
Actuation Method	—	Solenoid	Pneumatic	Pneumatic	Solenoid
Check Valve Type	—	Single	Single	Array	Single
Max. Flow Rate	\dot{Q}_{\max} ($\mu\text{l}/\text{min}$)	3.4	4.4	13	4.5
Max. Back Pressure	p_{\max} (kPa)	2.1	3.6	5.9	1.32
Max. Stroke Volume	ΔV_{\max} (μl)	8.4	14	28	9.5
Pump Chamber Volume	$V_{\text{pump chamber}}$ (μl)	87	50	50	50
Dead Volume	V_0 (μl)	78.6	36	22	40.5
Compression Ratio	ε	0.1	0.4	1.3	0.2
Actuator Power	P_{actuator} (W)	0.7	—	—	0.7
Pump Power	P_{pump} (W)	1.2×10^{-7}	—	—	1.0×10^{-7}
Pump Efficiency	η	1.7×10^{-5}	—	—	1.4×10^{-5}

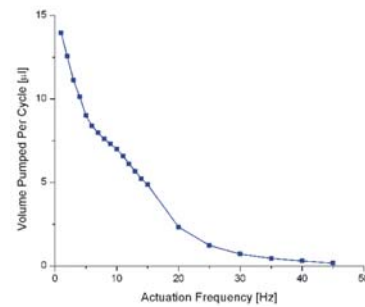
Discrepancies between the maximum flow rate achieved for pneumatic versus solenoid actuation were due to the inability of the solenoid actuator to produce deflections equal to the height of the pump chamber. Also, pneumatically driven pumps have much higher compression ratios. Even though the dead volume was successfully reduced in the second design of the solenoid driven pump, the pump power and pump efficiencies remain roughly the same.

In an ideal micropump, the volume of liquid pumped per actuation cycle is a constant regardless of the actuation frequency. This translates into a linear relationship between flow rate and actuation frequency. However, as can be seen in Figure 2-40, the volume decreases with increasing frequency. In the pneumatically actuated pump, since flow rate is equal to the

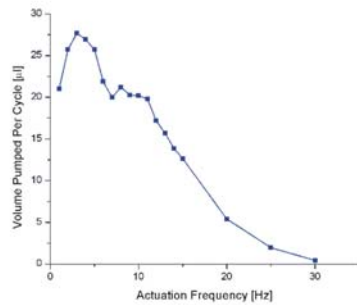
pressure drop over the fluidic resistance ($Q = P/R_{\text{fluid}}$), the volume pumped per cycle is inversely proportional to the frequency. Solenoid actuation, in which the membrane and plunger are physically connected, produces a more complicated behavior that cannot be completely described by this simple analysis. The data suggest that the membrane deflection, which occurs in a finite amount of time, might be a contributing factor as it also decreases with increasing frequency.



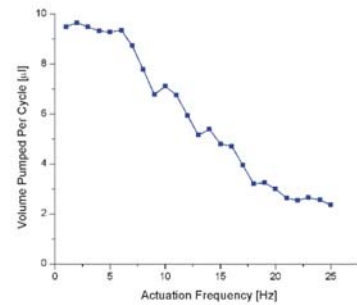
Pump 1



Pump 2



Pump 3



Pump 4

Figure 2-40 Volume Pumped Per Cycle vs. Frequency of the Various Pumps

For the pumps presented, a solenoid actuator was sufficient to demonstrate the device. However, integrated actuators, perhaps either thermopneumatic or piezoelectric ones, would provide a more practical solution for an integrated system. The pump footprint would be reduced, but there would be a trade-off in performance. Both thermopneumatic and

piezoelectric actuators have their advantages and disadvantages as discussed earlier in the chapter. Although much knowledge has been gained on micropumps, much work remains to be done to achieve a practical MEMS micropump for integrated fluidics applications.

2.5 SUMMARY

Two generations of check-valved silicone rubber diaphragm pumps are presented. Significant improvements have been made from pump to pump including the design and fabrication of a double-sided check valve, a bossed silicone membrane, and silicone gaskets. For the first time, check valve arrays were implemented in a micro diaphragm pump. Water flow rates of up to 13 ml/min and a maximum back pressure of 5.9 kPa were achieved through pneumatic operation with an external compressed air source. Using a custom designed solenoid actuator, flow rates of up to 4.5 ml/min and a maximum back pressure of 2.1 kPa have been demonstrated.

REFERENCES

- [1] Chen, C.-H., S. Zeng, J.C. Mikkelsen, Jr., and J.G. Santiago, *Development of a Planar Electrokinetic Micropump*, in *ASME 2000*. 2000: Orlando, FL. p. 523-528.
- [2] Kurosawa, M., T. Watanabe, and T. Higuchi, *Surface Acoustic Wave Atomizer with Pumping Effect*, in *MEMS '95*. 1995: Amsterdam, The Netherlands. p. 25-30.
- [3] Jang, J. and S.S. Lee, *Theoretical and experimental study of MHD (magnetohydrodynamic) micropump*. *Sensors and Actuators A*, 2000. **80**(1): p. 84-89.
- [4] Lemoff, A.V. and A.P. Lee, *An AC magnetohydrodynamic micropump*. *Sensors and Actuators B*, 2000. **63**(3): p. 178-185.
- [5] White, F.M., *Fluid Mechanics*. 3rd ed. 1994: McGraw Hill, Inc.
- [6] Nguyen, N.-T. and S.T. Wereley, *Fundamentals and Applications of Microfluidics*. 2002: Artech House, Inc.
- [7] Nguyen, N.-T. and S.T. Wereley, *Microfluidics for Internal Flow Control: Micropumps*, in *Fundamentals and Applications of Microfluidics*. 2002, Artech House, Inc. p. 293-342.
- [8] Hong, C.-C., J.-W. Choi, and C.H. Ahn, *Disposable Air-Bursting Detonators as an Alternative On-Chip Power Source*, in *MEMS 2002*. 2002: Las Vegas, NV. p. 240-243.
- [9] Grosjean, C. and Y.-C. Tai, *A Thermopneumatic Peristaltic Micropump*, in *Transducers '99*. 1999: Sendai, Japan. p. 1776-1779.
- [10] Chou, H.-P., M. Unger, A. Scherer, and S.R. Quake, *Integrated Elastomer Fluidic Lab-on-a-chip - Surface Patterning and DNA Diagnostics*, in *2000 Solid-State Sensor and Actuator Workshop*. 2000: Hilton Head, SC. p. 111-114.
- [11] Kovacs, G.T.A., *Micromachined Transducers Sourcebook*. 1998: McGraw-Hill Companies, Inc.
- [12] Richter, M., R. Linnemann, and P. Woias, *Robust design of gas and liquid micropumps*. *Sensors and Actuators A*, 1998. **68**(1-3): p. 480-486.
- [13] van Lintel, H.T.G., F.C.M. van de Pol, and S. Bouwstra, *A Piezoelectric Micropump Based on Micromachining of Silicon*. *Sensors and Actuators A*, 1988. **15**(2): p. 153-167.
- [14] van de Pol, F.C.M., H.T.G. van Lintel, M. Elwenspoek, and J.H.J. Fluitman, *A Thermopneumatic Micropump Based on Micro-engineering Techniques*. *Sensors and Actuators A*, 1990. **21**(1-3): p. 198-202.
- [15] Zengerle, R., A. Richter, and H. Sandmaier, *A Micro Membrane Pump With Electrostatic Actuation*, in *MEMS '92*. 1992: Travemunde, Germany. p. 19-24.

- [16] Cole Parmer Instrument Company, *Masterflex tubing pump animation*.
<http://www.coleparmer.com>.
- [17] Folta, J.A., N.F. Raley, and E.W. Hee, *Design, Fabrication and Testing of a Miniature Peristaltic Membrane Pump*, in *1992 Solid State Sensor and Actuator Workshop*. 1992: Hilton Head, SC. p. 186-189.
- [18] Olsson, A., G. Stemme, and E. Stemme, *Micromachined Diffuser/Nozzle Elements for Valve-less Pumps*, in *MEMS '96*. 1996: San Diego, CA. p. 378-383.
- [19] Olsson, A., P. Enoksson, G. Stemme, and E. Stemme, *An Improved Valve-less Pump Fabricated Using Deep Reactive Ion Etching*, in *MEMS '96*. 1996: San Diego, CA. p. 479-484.
- [20] Ahn, C.H. and M.G. Allen, *Fluid Micropumps Based on Rotary Magnetic Actuators*, in *MEMS '95*. 1995: Amsterdam, The Netherlands. p. 408-412.
- [21] Döpfer, J., M. Clemens, W. Ehrfeld, S. Jung, K.-P. Kämper, and H. Lehr, *Micro gear pumps for dosing of viscous fluids*. *Journal of Micromechanics and Microengineering*, 1997. **7**(3): p. 230-232.
- [22] Fuhr, G., R. Hagedorn, T. Müller, W. Benecke, and B. Wagner, *Pumping of Water Solutions in Microfabricated Electrohydrodynamic Systems*, in *MEMS '92*. 1992: Travemünde, Germany. p. 25-30.
- [23] Ahn, S.-H. and Y.-K. Kim, *Fabrication and experiment of a planar micro ion drag pump*. *Sensors and Actuators A*, 1998. **70**(1-2): p. 1-5.
- [24] Gunji, M., T.B. Jones, and M. Washizu, *DEP Microactuation of Liquids*, in *MEMS 2001*. 2001: Interlaken, Switzerland. p. 385-388.
- [25] Manz, A., C.S. Effenhauser, N. Burggraf, J.D. Harrison, K. Seiler, and K. Fluri, *Electroosmotic pumping and electrophoretic separations for miniaturized chemical analysis systems*. *Journal of Micromechanics and Microengineering*, 1994. **4**(4): p. 257-265.
- [26] Jun, T.J. and C.-J. Kim, *Valveless pumping using traversing vapor bubbles in microchannels*. *Journal of Applied Physics*, 1998. **83**(11): p. 5658-5664.
- [27] Ozaki, K., *Pumping Mechanism Using Periodic Phase Changes of a Fluid*, in *MEMS '95*. 1995: Amsterdam, The Netherlands. p. 31-36.
- [28] Sammarco, T.S. and M.A. Burns, *Thermocapillary Pumping of Discrete Drops in Microfabricated Analysis Devices*. *AIChE Journal*, 1999. **45**(2): p. 350-366.
- [29] Tirén, J., L. Tenerz, and B. Hök, *A Batch-Fabricated Non-Reverse Valve with Cantilever Beam Manufactured by Micromachining of Silicon*. *Sensors and Actuators A*, 1989. **18**(3-4): p. 389-396.
- [30] Esashi, M., S. Shoji, and A. Nakano, *Normally Closed Microvalve and Micropump Fabricated on a Silicon Wafer*. *Sensors and Actuators A*, 1989. **20**(1-2): p. 163-169.

- [31] Schomburg, W.K. and B. Scherrer, *3.5 μm thin valves in titanium membranes*. Journal of Micromechanics and Microengineering, 1992. **2**(3): p. 184-186.
- [32] Smith, L. and B. Hök, *A Silicon Self-Aligned Non-Reverse Valve*, in *Transducers '91*. 1991: San Francisco, CA. p. 1049-1051.
- [33] Shoji, S., M. Esashi, B. van der Schoot, and N. de Rooij, *A study of a high-pressure micropump for integrated chemical analysing systems*. Sensors and Actuators A, 1992. **32**(1-3): p. 335-339.
- [34] Wang, X.Q. and Y.C. Tai, *A Normally Closed In-Channel Micro Check Valve*, in *MEMS 2000*. 2000: Miyazaki, Japan.
- [35] Wang, X.-Q., *Integrated Parylene Micro Electro Mechanical Systems (MEMS)*, Ph.D. Thesis in *Electrical Engineering*. 2000, California Institute of Technology: Pasadena, CA.
- [36] Wang, X.-Q., Q. Lin, and Y.-C. Tai, *A Parylene Micro Check Valve*, in *MEMS '99*. 1999: Orlando, FL. p. 177-182.
- [37] Specialty Coating Systems, *Parylene Conformal Coatings Specifications and Properties*. <http://www.scscookson.com/parylene/properties.htm>.
- [38] Specialty Coating Systems, *Discovery and Early History of Parylene*. <http://www.scscookson.com/parylene/origin.htm>.
- [39] Wang, X.-Q., X. Yang, K. Walsh, and Y.-C. Tai, *Gas-Phase Silicon Etching with Bromine Trifluoride*, in *1997 Solid State Sensor and Actuator Workshop*. 1997: Hilton Head, SC. p. 1505-1508.
- [40] Grosjean, C., *Silicone MEMS for Fluidics*, Ph.D. Thesis in *Electrical Engineering*. 2001, California Institute of Technology: Pasadena, CA.
- [41] Yang, X., C. Grosjean, and Y.-C. Tai, *A Low Power MEMS Silicone/Parylene Valve*, in *1998 Solid-State Sensor and Actuator Workshop*. 1998: Hilton Head Island, South Carolina. p. 316-319.
- [42] Slatkin, A.B., *Modeling and experiments for a class of robotic endoscopes*, Ph.D. Thesis in *Mechanical Engineering*. 1999, California Institute of Technology: Pasadena, CA.

CHAPTER 3

MICROFLUIDIC COUPLERS

MEMS devices bring forth new challenges in the interconnectivity between the micro and macro worlds. The microelectronics world has relied heavily on advances in the packaging industry for technological advancement. Without novel breakthroughs in microelectronic package engineering, the continued miniaturization of electronics would not be possible. Microelectronic packages are constantly shrinking and quickly approaching sizes on the order of the device they are protecting. Perhaps one day, fabrication and packaging will be integrated and devices will be ready to plug in and use as soon as they are diced and separated from the wafer! The MEMS world is, however, far from reaching this ideal. While electrical connections are also important in MEMS, a comprehensive packaging technology does not exist. In addition to electrical connections, MEMS devices often require another means of communicating with the environment. For example, it is necessary to provide mechanical inputs to a pressure sensor or guide light into an optical switch. Perhaps the most

confounding example of this dilemma is found in the microfluidics field. The incompatibility of simultaneous electrical and fluid connections is a problem that has not been solved. Many difficult issues exist in defining the connections of micro-devices with the surrounding environment.

3.1 THE NEED FOR MICROFLUIDIC COUPLERS

Micromachined fluidic devices are poised to have a great impact on the field of biology and chemistry. The benefits of adopting microfluidic techniques are many including laminar fluid flow, minimal reagent consumption, minimal power consumption, small footprint, and the possibility of integrating multiple functions within one device. One major problem that has hampered the development and utilization of such devices is the lack of a reliable and efficient means of accessing the input/output fluidic ports. In the infancy of microfluidics, research was primarily focused on the development of discrete devices. With the change in direction towards the development of integrated systems, a means to efficiently connect fluidic devices together is needed. As an off-the-shelf product does not exist, current commercial microfluidic systems require custom connectivity solutions and are, as a result, very expensive. The goal of mass-producing inexpensive, disposable fluidic devices can only be realized when the appropriate connectivity technologies are developed.

The traditional method to provide fluidic connections to micro flow channels is to manually align and glue tubing to ports (Figure 3-1). Needless to say, this method is only practical for making a few one-time connections to prototypes. Batch processing and mass fabrication cannot rely on such a low yield, time consuming method. Other drawbacks include complex assembly, misalignment problems, the large footprint, and instability of the connection. Even

for the purposes of research, the numerous disadvantages of this method can outweigh its usefulness.

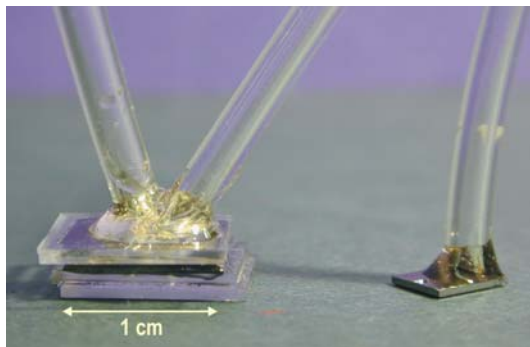


Figure 3-1 Examples of Glued Fluidic Connections Between Fluidic Devices and Tygon Tubing

In the macro world, connections are easily achieved due to the wealth of commercially available plumbing options. Standard prefabricated tubing and fittings are easily configured to achieve the desired result. The microfluidics world, which involves dimensions on the order of millimeters or smaller, does not have a readily available supply of fluidic connection products. Only one manufacturer of microfluidic connections exists [1]. In fact, most of the effort to develop microfluidic connections comes from academic research [2-11].

3.1.1 SEARCH FOR THE IDEAL COUPLER

As fluidic devices grow in diversity, it is entirely possible that a perfect one-size-fits-all type solution does not exist. Instead, a whole suite of connectors may be necessary to accommodate all categories of use. The possible constraints on fluidic coupler designs are many. As a result, making fluidic interconnects is a complex problem that is not well defined. Part of the problem is the lack of a standard in defining fluidic openings. Device prototypes are typically custom designs and fluidic ports are arbitrarily assigned sizes. In addition, other

requirements may exist. Some parameters that should be considered during coupler design are listed in Table 3.1.

Table 3.1 List of Parameters Influencing Fluidic Coupler Design

Temperature Operating Range	Mechanical Strength
Maximum Pressure Requirements	Chemical Resistance
Connection Density	Clogging
Volume Flow Requirements	Ease of Assembly/Alignment
Biocompatibility	Cost
Wetted Surface Properties	Connection Yield
Reusability	Compatibility to Device
Dead Volume	Time to Assemble
Ease of Removal/Replacement	Overall Size

3.1.2 CURRENT MICROFLUIDIC COUPLING SOLUTIONS

3.1.2.1 ACADEMIC WORK

Researchers have explored several different methods of achieving fluidic connections. Each of these methods has benefits and drawbacks.

One of the earliest efforts to create fluidic coupling is a capillary connector designed for a chemical analysis system [12]. This connection is created by a combination of wet and dry etching techniques. Capillaries are glued directly to a fitted port with a built-in tubing stop (Figure 3-2).

By taking advantage of the crystalline structure of silicon and the resultant geometries of wet etching, both an in-plane and out-of-plane interconnect were realized in [11] (Figure 3-2). The in-plane connector consists of two symmetrically etched halves that are bonded together to form an edge-protruding fluid channel to which flexible tubing can be press-fitted onto. A vertical interlocking coupler is formed by etching interlocking fins around a fluidic port. A mating piece is pressed into place over a gasket sealing the fluid pathway. The requirement of

stacking in the construction of these interconnects can needlessly complicate device design. High density connections are difficult given the space requirements for each coupling. Also, the pressure range of these couplers is low due to the low sealing force of the press-fittings.

Another group proposed a fluidic ribbon cable equivalent as a means to connect surface micromachined channels from device to device (Figure 3-2). The flexible cable is made of embedded polymer channels with openings at the ends and is directly glued to channels on a device.

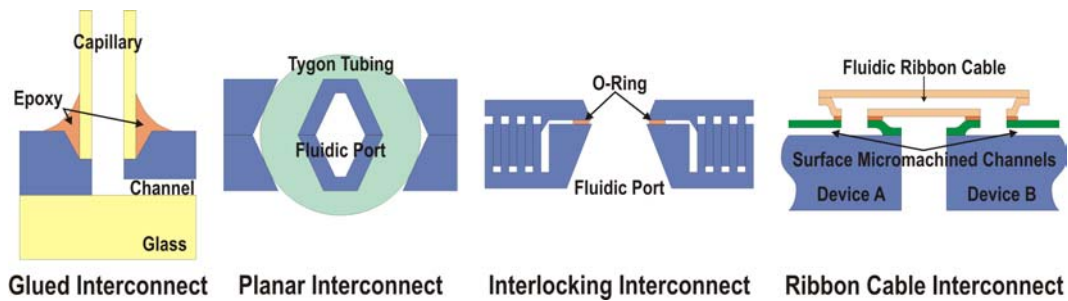


Figure 3-2 Early Examples of Fluidic Interconnect Research

A method of making a micro fittings system is presented in [9]. This is perhaps the most unique coupling solution in that only conventional machining techniques are required to fabricate the components. The concept behind this method is to mimic commonly available threaded fittings that are used to hold precision machined PEEK connectors via compression. Fluidic devices are stacked and clamped into a housing into which is machined the necessary mating connections. Three different types of interconnects were designed of which two are snap-in connectors and one is a ferrule based connector (Figure 3-3).

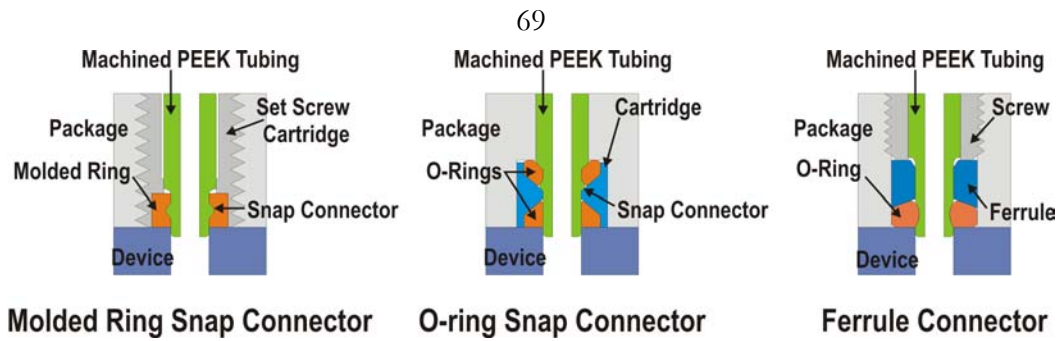


Figure 3-3 Precision Machined PEEK Connectors

Another stacked system can be found in [8]. Here silicon fusion bonding is used to connect a DRIE etched layer with coupler receptacles to another layer with channels (Figure 3-4). Fused silica tubing is fitted into a pit or sleeve structure on the coupler layer and glued into place. In an effort to move away from gluing connections, an injection molded plastic connector was also designed for use in the same multi-layer system.

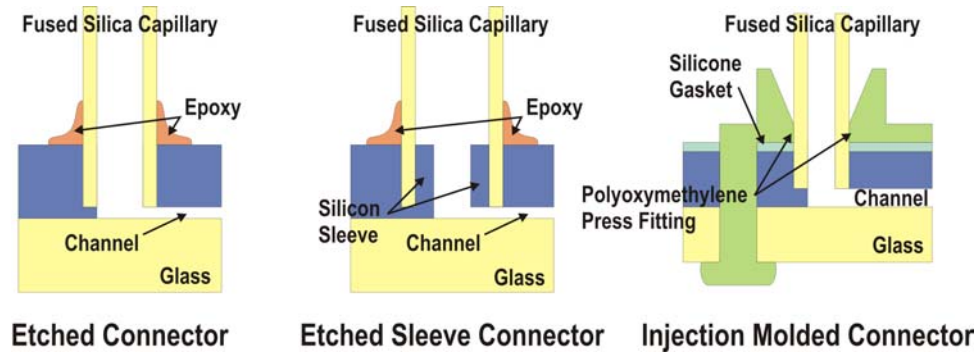


Figure 3-4 Various DRIE Etched Connectors

Recent work involves the use of polymer materials to make connections (Figure 3-5). All of these are designed to avoid the use of adhesive or prevent adhesive from entering the fluid path. An integrated silicone o-ring coupler is presented in [13]. Couplers are inserted into a slightly smaller silicone orifice and held in place by the compressed silicone ring. Another group directly fused polyethylene tubing onto the roughened surface surrounding a fluidic port then reinforced the connection with epoxy [7]. This coupler was specifically designed for use

with a valveless pump. A similar approach is found in [5]. Again epoxy is used to reinforce a temporary connection. Adhesive coated mylar sheets or layers are used to mate a capillary with a fluidic port before being sealed into place permanently by epoxy. Two techniques are developed for making discrete connections or for making multiple connections.

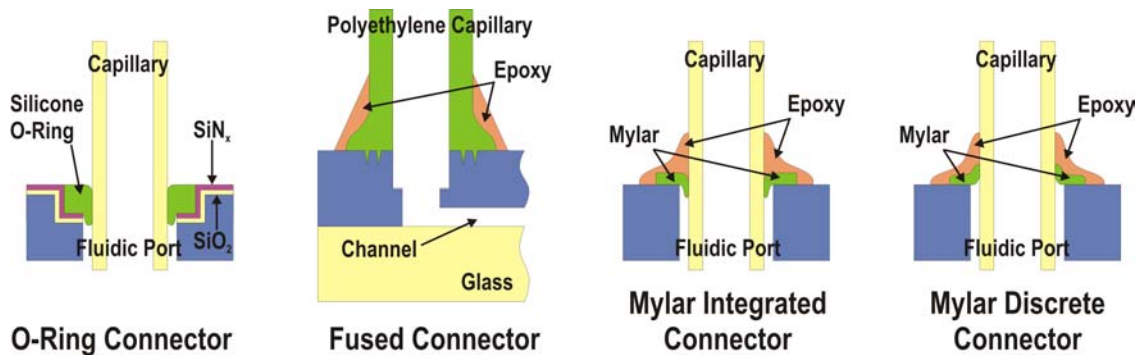


Figure 3-5 Various Polymer Based Connectors

A polymer/glass connection scheme is given in [4]. PEEK tubing, thermoplastic flanges, and a polycarbonate or glass substrate are used to create interconnects. Compression molding and thermal treatment are used to create connections. Again, both discrete and integrated solutions were developed (Figure 3-6).

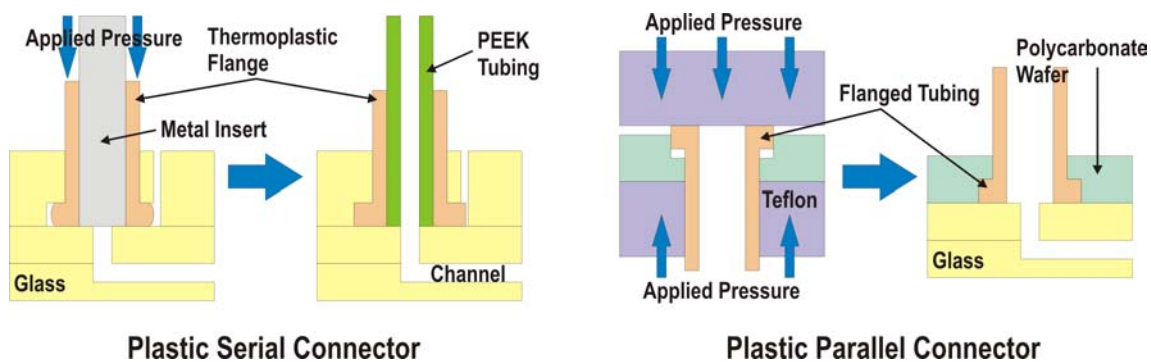


Figure 3-6 Compression Molded Polymer Connectors

3.1.2.2 COMMERCIAL PRODUCTS

Upchurch Scientific makes the only commercial product line available for making microfluidic connections. NanoPort™ Assemblies are specifically listed in their catalog as being for Lab-on-a-Chip applications (Figure 3-7). Assembly involves aligning and gluing a base unit to a fluidic port. Once in place and cured, the base unit provides a means to connect a variety of tubing (360 μm, 510 μm, or 1/32 inch in outer diameter) or itself can serve as a reservoir for fluid. Several cleverly designed features are available in their product. First, adhesive can conveniently be purchased in pre-formed rings and is absent from the wetted path after application. The adhesives were selected to bond well to silicon, quartz, glass, and polymers, all of which are commonly encountered materials in microfluidics. In addition the connection is dead volume free and made of PEEK (polyetheretherketone) which is both inert and biocompatible. As Upchurch Scientific provides specialty connections for HPLC (high pressure liquid chromatography) end users, it is not surprising that these microfluidic connections are also rated to withstand pressures up to 1500 psi. While this solution is an excellent first entry in the market, it can still be improved. The major drawbacks are that the adhesive requires a high temperature cure and the connectors take up a large amount of space. Reservoir units are 9.7 mm in diameter and port bases are 8.4 mm. Assembled connections can extend upwards of 1cm. Many devices are still designed around a 1 cm × 1 cm die, in which there is only enough space for one NanoPort™ connection. A high density connector that can be applied in a parallel fashion is still sought.

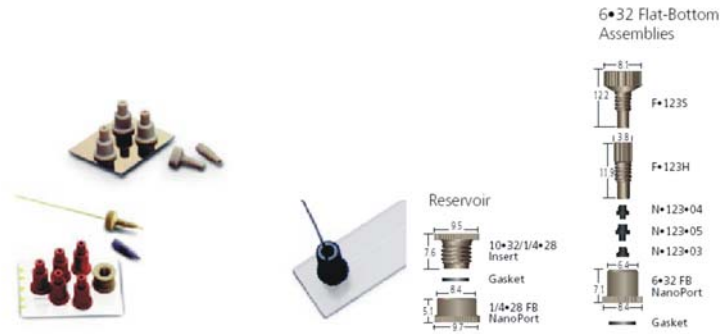


Figure 3-7 Upchurch Scientific NanoPort™ Assemblies

3.2 DESIGN AND FABRICATION

3.2.1 DESIGN CONSIDERATIONS

Since the microfluidics field emerged out of MEMS, the fabrication processes through which fluidic ports are created are based in micromachining techniques. When dealing with micromachined channels, two options are available for making fluidic connections: (1) front-to-back through-substrate fluidic pathways or (2) front side fluidic connections, typically to surface micromachined channels. Surface micromachined channels are fragile and can easily be crushed or otherwise damaged. This makes front side coupling a non-trivial task. Bulk channels are more robust and more forgiving of inelegant coupling solutions.

Access to channels can be made in different ways. Prior to the invention of DRIE, wet etching and mechanical drilling were the only practical ways to create front-to-back openings. Drilling can be quick and convenient for make a few connections but alignment and high density can be difficult to achieve. Also, not all connections are possible by drilling access ports. Usually, only bulk micromachined channels can accommodate drilling. For wet etching, anisotropic etching is preferred to “conserve” real estate, as only large openings are possible by isotropic etching due to lateral undercut. Structures produced by using KOH, EDP, or TMAH to etch silicon have the characteristic geometry predicted by the slowest

etching plane in the crystalline material, which, in the case of (100) silicon wafers, happens to be the (111) plane. This results in geometries that are square and tapered at an angle of 54.74° (Figure 1-3). It is possible that in some applications, this shape may have undesirable effects on fluid flow. Given that tubing is typically round, a geometrical mismatch is present between the tubing and the port (Figure 3-8). While it is possible to glue tubing directly to pyramidal pits, leakage paths due to mismatch (non-interlocking halves) may result in clogging by adhesives. By using DRIE, the geometry of fluidic ports is no longer restricted in such a manner. Also lower dead volumes can be achieved by machining matched and interlocking structures.

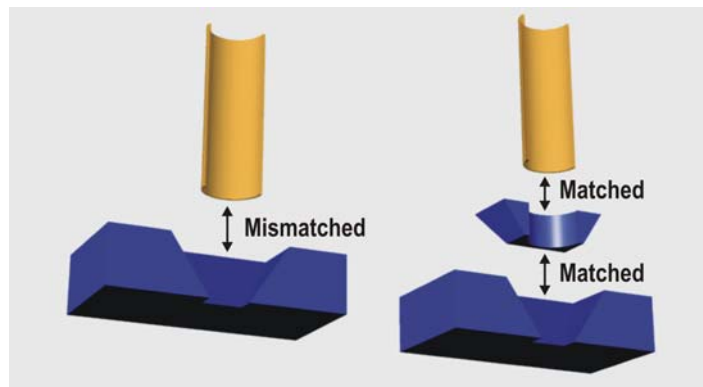


Figure 3-8 Cross Section of Mismatched and Matched Tubing-to-Fluidic Port Connections

Fluidic ports cannot be designed without considering the tubing that will be used in the final connection. It is important to select the appropriate tubing type and tubing material. Only certain materials and sizes of tubing are commercially available so if, for example, a system requires the channel and tubing diameters to be matched, this should be taken into account when putting a device through the design phase. Given this information, the maximum connection density is limited by the tubing selected. Connection density is also hampered by human dexterity and visual capabilities. Requiring adhesive to create bonds further

complicates the issue. At some point, it will be necessary to use mechanical micromanipulators or automated machines to assemble fluidic connections.

The usage of adhesive in fluidic coupling can be a controversial issue. While biocompatibility issues may preclude the usage of glue in some applications, high-pressure connections are difficult to achieve using press-fitting techniques. Most microfluidic connections rely on perpendicular coupling between ports and tubing. Given the small surface contact area, adhesive is usually required to form the connection or provide mechanical strength to the connection, even when using press-fittings. It is important in these situations to prevent adhesive from entering the fluid path. Not only do out-of-plane schemes cause difficulty for fluidic coupling, they can also complicate fluid flow or get in the way of electrical interconnects. Ideally, connections could be made in plane but the limited area in which to do so makes it difficult; the thickness of a silicon wafer is typically only 500 μm . Stacking dies helps but is not always an option. For these reasons, vertical connections are still the most popular method.

3.2.2 MICROMACHINED FLUIDIC COUPLERS

To meet some of the aforementioned challenges, several types of fluidic couplers have been designed, fabricated, and tested. The approach taken here is to introduce an intermediate mechanical structure to provide geometrically matched, interlocking connections between the tubing and the fluidic port. Both silicon and polymer materials can be used to fabricate this mating connector. In the case of silicon, bulk micromachining and DRIE techniques have been explored to yield couplers capable of being used with most microfluidic ports. Virtually any two-dimensional geometry can be etched using DRIE and so nearly any arbitrary fluidic port shape can be accommodated. Polymer couplers can be molded from etched silicon

masters. To take advantage of the wealth of pre-existing commercial tubing products, these couplers interface with PEEK and fused silica capillary tubing. Tubing types were selected for their small size, common acceptance in HPLC applications, and for versatility. A wide variety of supporting products include adapters and fittings are readily available making them a convenient choice. PEEK also has excellent chemical resistance.

Features have been added to facilitate and guide assembly. Fittings are designed to include alignment structures and if necessary, stepped sleeves that serve as a tubing insertion depth guide. Couplers are joined to pre-existing fluidic ports via these fittings. In addition to restraining the tubing insertion depth, it may also be necessary to control the coupler insertion depth. When interfacing to devices with delicate membrane structures at the other end of a fluidic port, couplers with shoulders can be used. These shoulders can effectively limit the penetration depth of a coupler into a port.

Adhesive can be used to connect couplers to tubing, but, when the dimensions of the mating receptacle are appropriately calibrated, cryogenic insertion is also an option (Figure 3-9). This approach is time consuming, inconsistent, and extremely inconvenient. To mitigate these issues, a batch adhesive application and bonding process was developed. By using Crystalbond, a thermoplastic adhesive, wafer level spray coating to thousands of couplers at once is achieved (Figure 3-10). The thermoplastic nature of Crystalbond allows easy attachment and removal of parts through thermal cycling. Applying epoxy to the formed joint can strengthen the connection. Alternatively, couplers can also be molded with a thermoplastic material and subsequently reflowed to form a connection. It is also possible to use other adhesive joining methods as well as solder and eutectic bonding at the coupler-to-

I/O port interface. Modified couplers with fitting structures at both ends of the capillary can also be used to concatenate microfluidic devices.

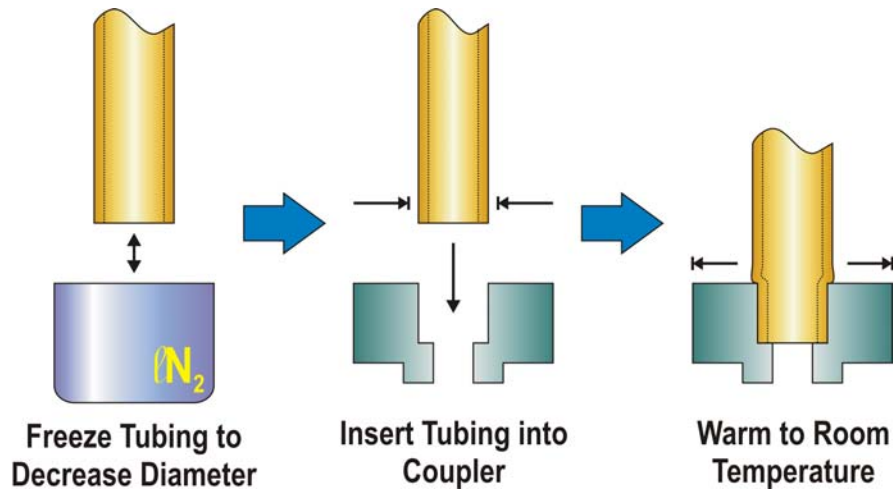


Figure 3-9 Cryogenic Insertion Process

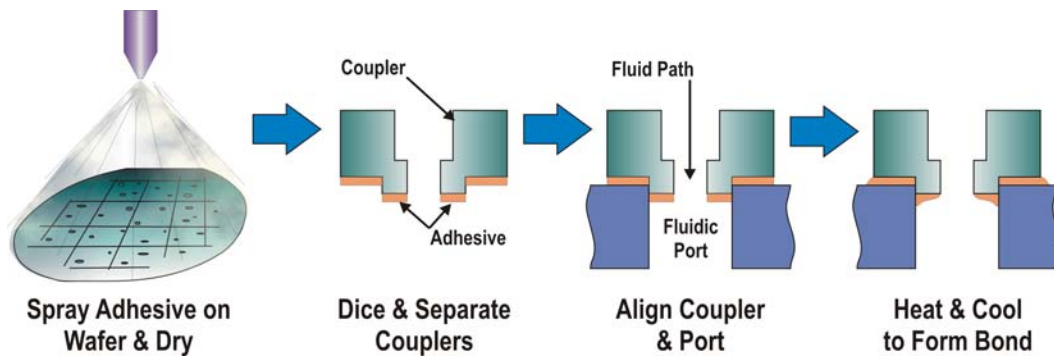


Figure 3-10 Spray Coating Process

A comparison of traditional manual coupling techniques with our new approach is demonstrated on thermopneumatic valves from [14] in Figure 3-11. The space savings are readily apparent in this photography. Fused silica capillaries attached to silicon bulk couplers are used to create inlet/outlet access in the valve on the left. The valve on the right has tygon tubing directly glued to the inlet and outlet.

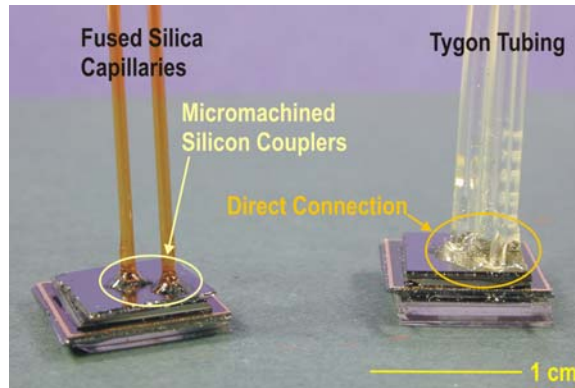


Figure 3-11 Comparison of Fluidic Coupling Techniques

Four types of couplers using various sizes of capillary and PEEK tubing have been fabricated. Process flows for the various types of couplers are described below.

3.2.3 BULK COUPLERS

Bulk couplers are designed to match the geometry of anisotropically wet etched fluidic ports. The fabrication process (Figure 3-12) for bulk micromachined silicon couplers starts with the thermal oxidation of silicon wafers ($\sim 1.5 \mu\text{m}$). Then, the overall geometrical structure of the coupler is defined by a patterning step followed by etching in KOH (potassium hydroxide). Mesas of about $270 \mu\text{m}$ high are formed in this manner. Each mesa will eventually become an individual bulk coupler. On the other side of the wafer, press-fit pits for tubing are etched via DRIE to a depth of about $450 \mu\text{m}$. This method will leave a tubing stop structure so as to prevent the tubing from piercing through the other side of the coupler during assembly (Figure 3-13). Alternatively, for simplicity of fabrication, the pit can be etched through the wafer. An additional shoulder is useful as an insertion guide and is depicted in Figure 3-13.

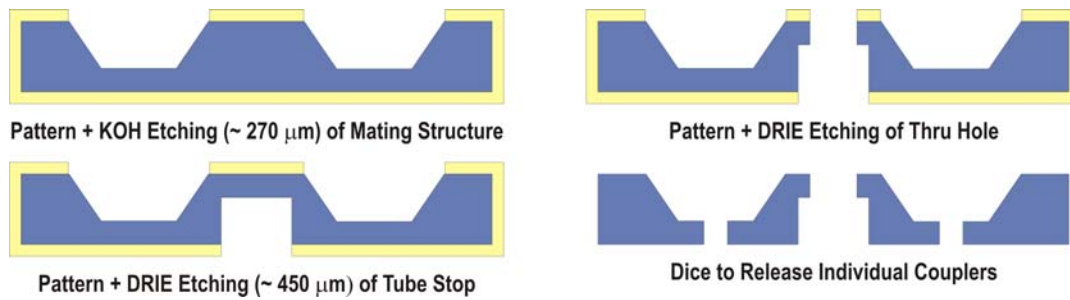


Figure 3-12 Bulk Coupler Fabrication Process

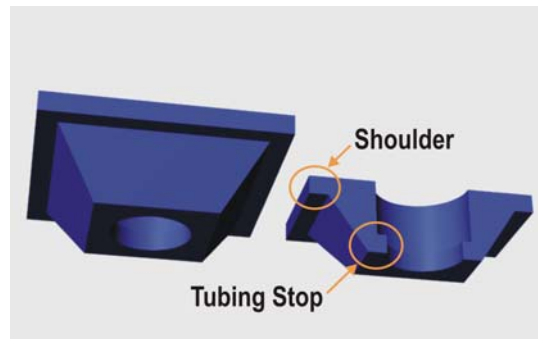


Figure 3-13 Three Dimensional Rendering of a Bulk Coupler

As evident from the desired geometry and given the properties of KOH etching, corner compensation is required to achieve sharp corners on the mesas. Two corner layout schemes were investigated with the respective etching results are shown in Figure 3-14. The merits of each method are described in [15] and [16], respectively. Additional features in the rightmost figure are artifacts attributed to the DRIE of masking gaps due to poor photoresist step coverage. While both convex corners exhibit a certain degree of undercut, slight modifications to the etch mask and careful attention to etching progress should eliminate these features.

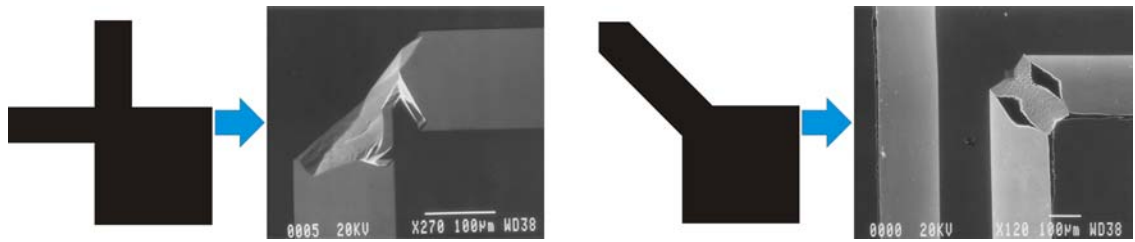


Figure 3-14 Corner Compensation Schemes and Results

Different sizes of bulk couplers were fabricated based on the outer diameters of fused silica capillary available (440 μm , 680 μm , and 850 μm in outer diameter). Various SEMs of bulk couplers are shown in Figure 3-15. Bulk couplers are assembled by using the cryogenic insertion technique to achieve a press-fit between the capillary and coupler. A coupler attached to a capillary is shown in Figure 3-16. This assembly is placed in contact with a matching fluidic port and then fixed in place with adhesive. A cross section of a coupler connected to a fluidic port is shown in Figure 3-17. Although adhesive was used to fill the inside of the coupler and tubing for the purposes of the photo, it can be seen that adhesive does not enter the fluid path in this interconnect implementation.

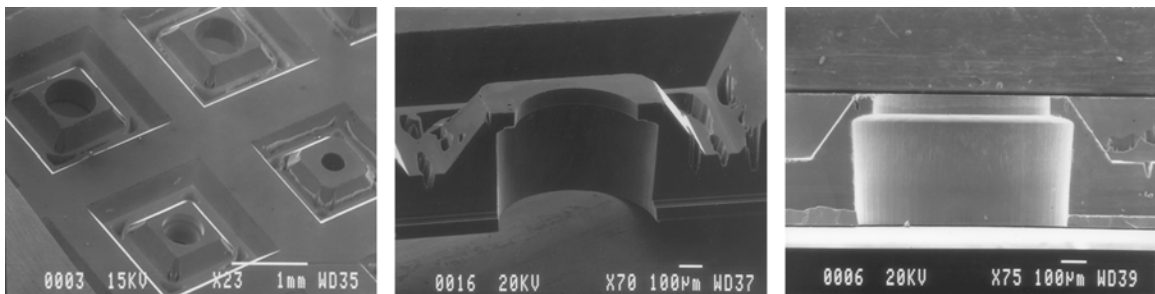


Figure 3-15 SEMs of Bulk Couplers

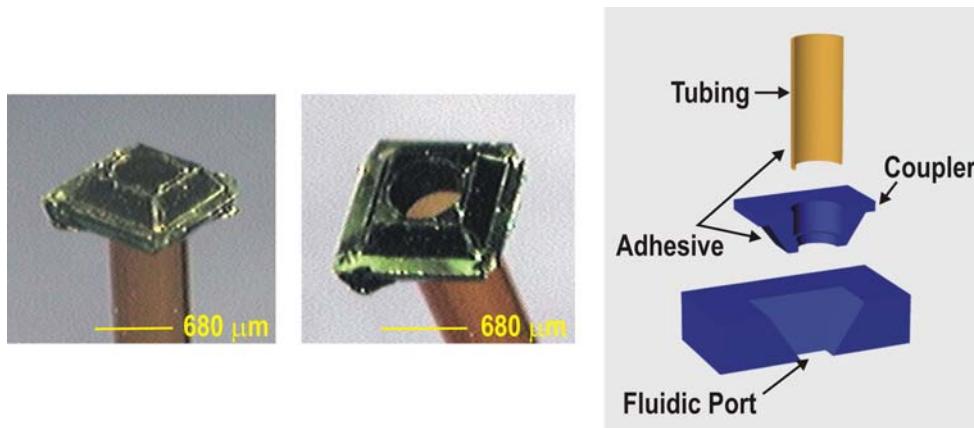


Figure 3-16 Bulk Couplers with Fused Silica Tubing and Assembly Process

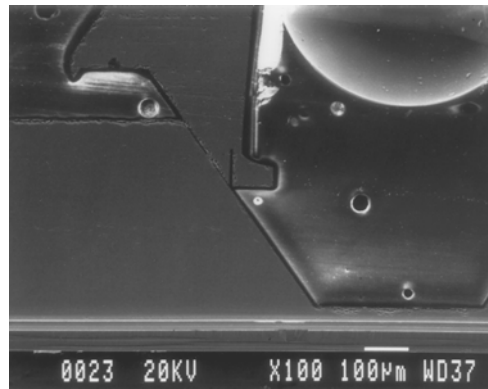


Figure 3-17 Cross Sectional SEM of a Glued Bulk Coupler

3.2.4 MOLDED COUPLERS

Molds for polymer couplers are created by bonding two etched wafers together. One wafer defines the geometry of the coupler while the other provides posts to hold tubing in place during the molding process. The fabrication process for molds is summarized in Figure 3-18. The “body” mold wafer starts with a thermally oxidized silicon wafer ($\sim 1.5 \mu\text{m}$). It is then patterned and etched through in KOH. The mating “post” wafer also starts with a thermally oxidized silicon wafer ($\sim 1.5 \mu\text{m}$). Circular pegs about $300 \mu\text{m}$ tall are etched by DRIE. After the remaining oxide is removed by BHF (buffered hydrofluoric acid), the wafers are diced and the two mating dies are bonded together using adhesive. A PTFE (polytetrafluoroethylene)

based mold release layer is then sprayed onto the assembled mold. The release layer facilitates removal of the molded coupler from the mold structure and prevents adhesion of the molded coupler to the mold. It is also possible to substitute for other types of mold release layers. Plasma deposited teflon and parylene C are also candidates for mold release layers. Moldings are realized by melting raw material such as a hot-melt polyolefin around fused silica tubing fitted on mold posts. When the polyolefin material has cooled, couplers can be release simply by pulling them away from the mold. Released structures are then attached to fluidic ports simply by re-heating polyolefin, allowing it to reflow and adhere to the silicon port. In applications where heating is unacceptable, adhesive joining can be used.

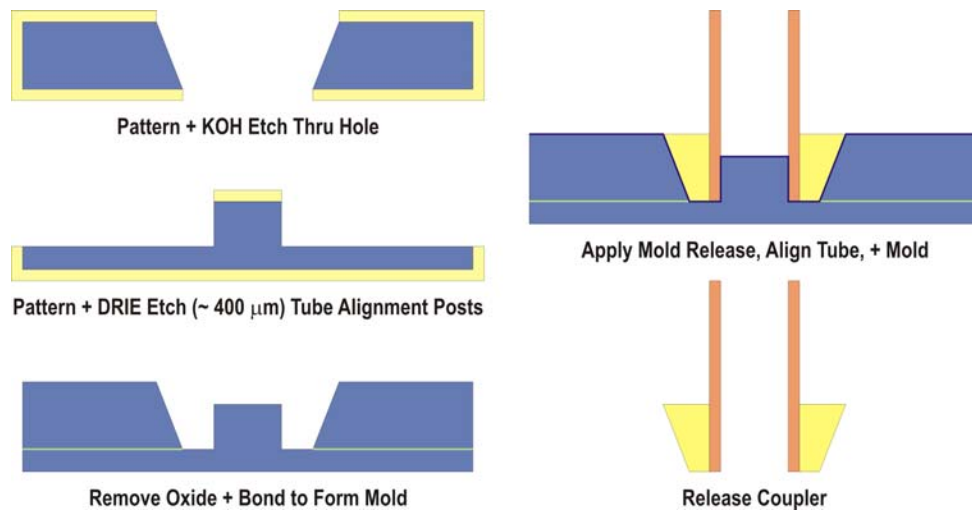


Figure 3-18 Molded Coupler Fabrication Process

Different sizes of bulk couplers were fabricated based on the inner diameters of fused silica capillary available (320 μm , 545 μm , and 700 μm in inner diameter). Various SEMs of coupler molds are shown in Figure 3-19. A coupler attached to a capillary is also shown (Figure 3-20).

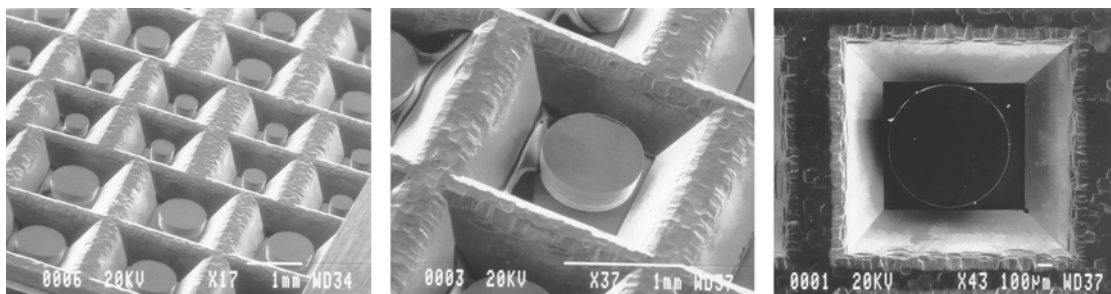


Figure 3-19 Views of Coupler Molds

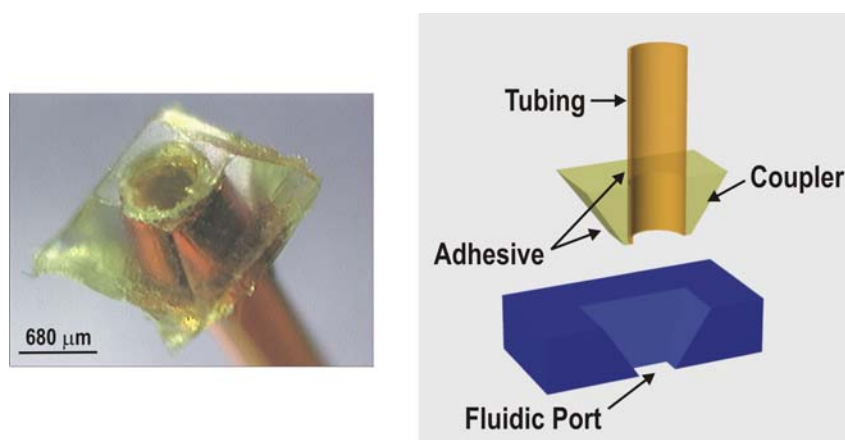


Figure 3-20 Molded Coupler with Fused Silica Capillary and Assembly Process

3.2.5 POST COUPLERS

The nature of DRIE processing allows flexibility in creating two-dimensional geometries across a wafer surface. A two-dimensional feature corresponding to the desired coupler geometry can be defined and etched in silicon. Thus, post couplers can be used with virtually any fluidic port and tubing. For example, if an odd coupling geometry such as the one depicted in Figure 3-21 is desired, it would be easy to fabricate by generating the appropriate masks and using DRIE to etch the structure. Cylindrical couplers were fabricated here for use specifically with PEEK tubing and fused silica capillaries.

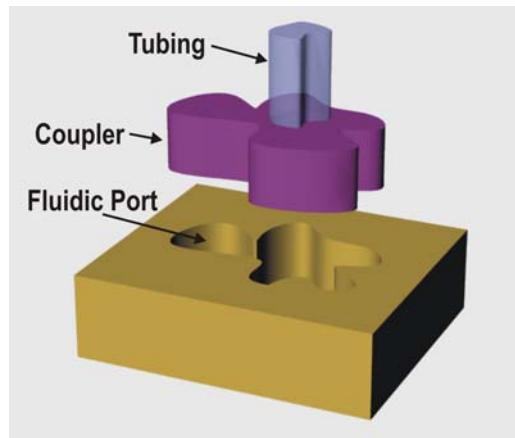


Figure 3-21 Example of a Possible Coupler System

The procedure for fabricating post couplers is given in Figure 3-22. Fabrication starts with the thermal oxidation of a silicon wafer ($\sim 1.5 \mu\text{m}$). The thermal oxide serves as a masking layer during etching. First, the alignment ring feature is patterned. Then a shoulder, which also serves as a bonding surface, is patterned and etched $100 \mu\text{m}$ deep using photoresist as a mask. A release ring is also patterned and etched in the same step. The remaining photoresist is removed, exposing the alignment structures. Another etch is performed to define the height of the alignment ring ($\sim 60 \mu\text{m}$). The total etched depth of the central opening that eventually becomes the through hole and the release ring is approximately $160 \mu\text{m}$. However, the opening is typically etched slightly deeper than the release ring due to geometrical loading effects common to DRIE systems. This ring allows individual couplers to be snapped off the wafer at the end of the process. On the other side of the wafer, a tubing stop and the other half of the release ring are patterned. These structures are etched until the central fluid path is completed. Individual couplers are snapped away from the wafer. Then, PEEK tubes or fused silica capillaries are press-fitted into the mating receptacles and the entire structure is then ready to be joined to a fluidic port.

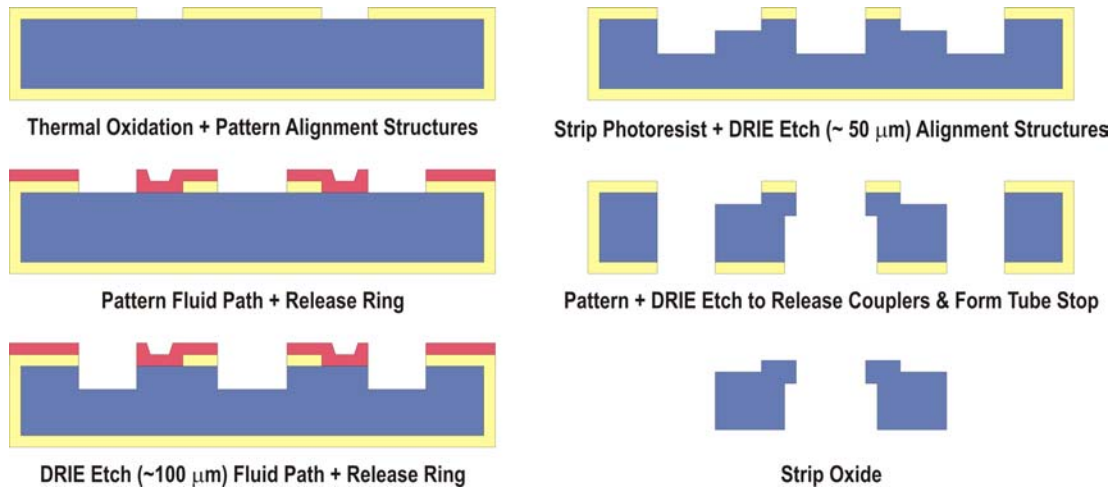


Figure 3-22 Post Coupler Fabrication Process

Several different sizes of post couplers were fabricated based on the outer diameters of fused silica capillaries ($440 \mu\text{m}$, $680 \mu\text{m}$, and $850 \mu\text{m}$ in outer diameter) and PEEK tubing available ($363 \mu\text{m}$, $508 \mu\text{m}$, and $1/16$ inch in outer diameter). Also the central opening is matched to the tubing inner diameter. SEMs of fabricated post couplers are shown in Figure 3-23. A coupler attached to tubing and an assembled system is shown in Figure 3-24.

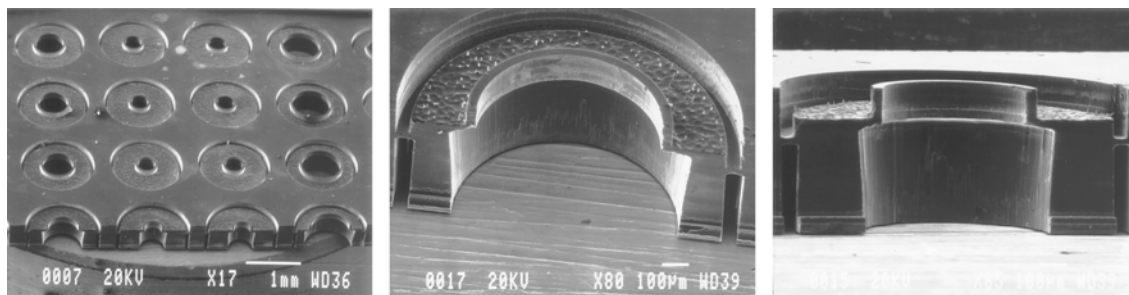


Figure 3-23 SEMs of Post Couplers

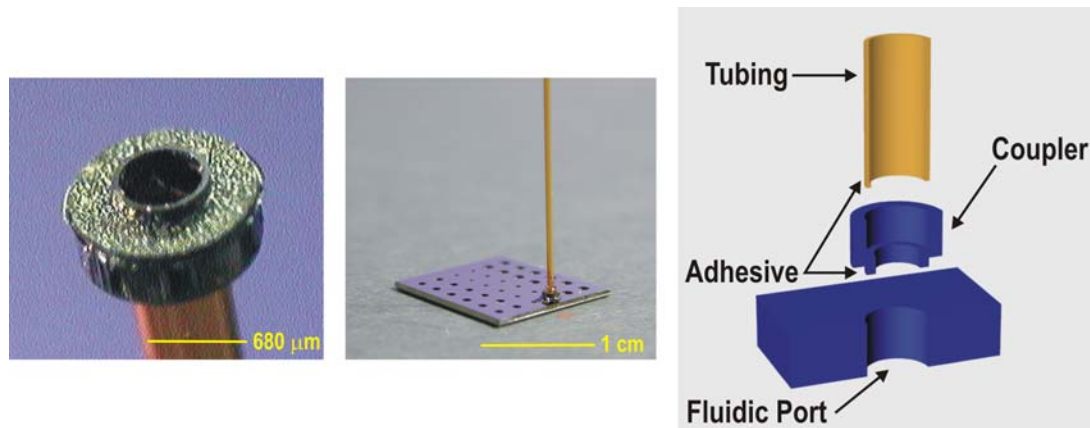


Figure 3-24 Post Couplers and Assembly Process

3.2.6 FLANGED COUPLERS

The final type of coupler is designed to sit flush against the surface to which it will be bonded. This geometry is convenient for use with devices having densely packed ports with small openings. Here, the density of the connections does not allow for alignment features to be included in the device. The lack of alignment features, however, means that this coupler has to be manually aligned. The flange is grooved so as to provide a greater surface area for bonding. Also, the grooves serve to guide adhesive away from the central opening to prevent clogging.

An abbreviated process flow for the fabrication of flanged couplers is illustrated in Figure 3-25. A wafer is thermally oxidized ($\sim 1.5 \mu\text{m}$) then the tubing receptacles and flange are patterned and etched in DRIE $350 \mu\text{m}$ deep. On the other side of the wafer, the tracks in the flange are patterned. Then the through hole and release ring are patterned and etched $100 \mu\text{m}$ deep by DRIE with photoresist as a mask. This release ring serves the same purpose as in the post coupler fabrication process. After the remaining photoresist is stripped, the tracks are exposed and a global etch is performed until the fluid pathway is etched through. The oxide mask layer is stripped in BHF then individual couplers are removed. PEEK tubing is attached using adhesive and the assembly is mated to a fluidic port.

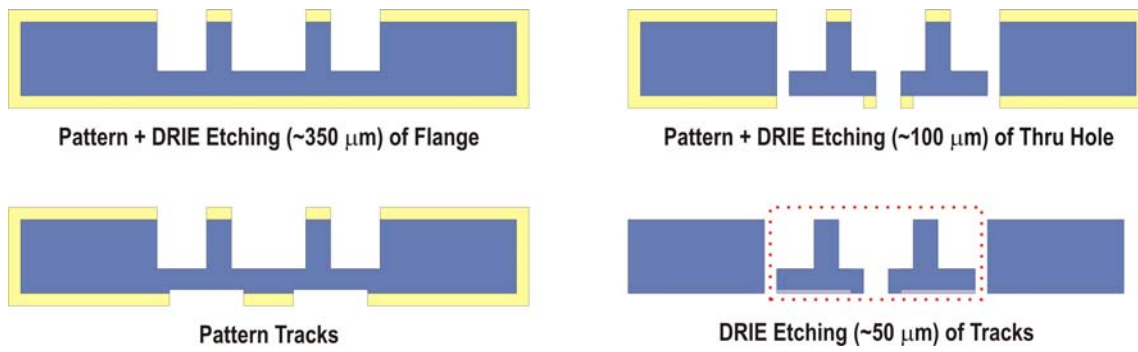


Figure 3-25 Flanged Coupler Fabrication Process

The various sizes of flanged couplers were fabricated based on the outer diameters of smallest diameter PEEK tubing available ($363 \mu\text{m}$ and $508 \mu\text{m}$). Tubing inner diameters are matched to the central opening of the couplers. Fabricated couplers were observed using an SEM and are shown in Figure 3-26. A coupler attached to tubing is shown in Figure 3-27.

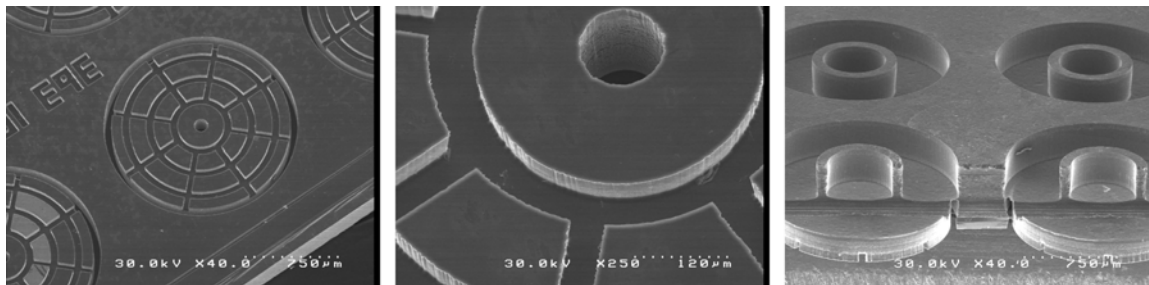


Figure 3-26 SEM Views of Flanged Couplers

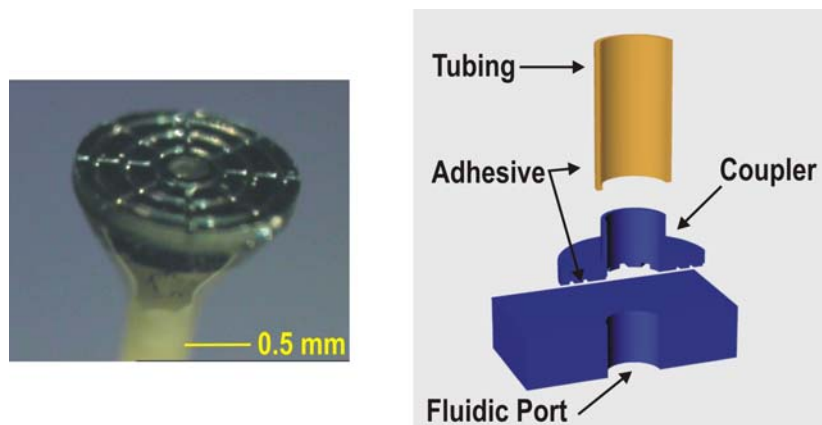


Figure 3-27 Flanged Coupler with PEEK Tubing and the Assembly Process

3.3 COUPLER TESTING

Two custom high-pressure testing setups were designed to determine the failure point and operating range of the fabricated couplers. The first setup is rated to pressures of 9×10^3 kPa (1300 psi) and filters particles in nitrogen gas down to $0.1 \mu\text{m}$. The second improved design is capable of sustaining pressures of 1.4×10^4 kPa (2000 psi) and filters down to $0.5 \mu\text{m}$. A graphical depiction of the testing setups is given in Figure 3-28. The actual setups are shown in Figure 3-29 and Figure 3-30. Testing setups were constructed of stainless steel Swagelok plumbing and components to sustain high-pressure operation. PEEK and Valco stainless steel high pressure liquid chromatography (HPLC) fittings were used to connect the small diameter PEEK and fused silica capillary tubing from the coupler to the rest of the pressure testing setup. Pressurized nitrogen gas is controlled through metering valves and monitored using an Omega PX120-2KGV pressure transducer in conjunction with an Omega DP25-S Strain Gage Panel Meter. The operating pressure range of the couplers is determined by gradually increasing the pressure on a blocked coupler.

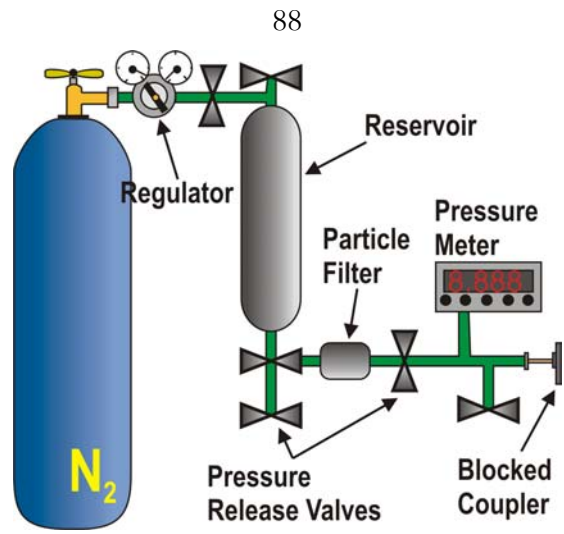


Figure 3-28 Schematic of Coupler Pressure Testing Apparatus



Figure 3-29 Original Testing Setup

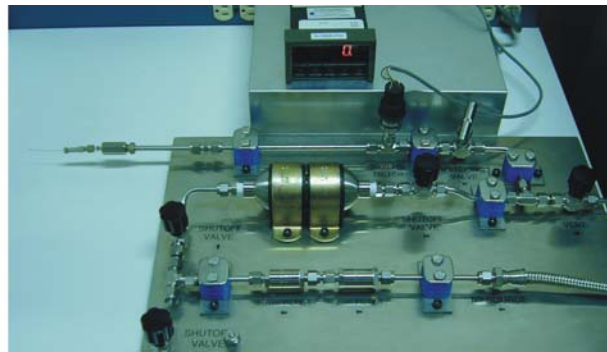


Figure 3-30 Improved Testing Setup

Bulk and post couplers with capillary tubing were tested using the first setup and were able to withstand at least 9×10^3 kPa (1300 psi). This corresponds to the maximum measurable

pressure of the experimental apparatus. Flanged couplers were tested on an improved setup and were able to withstand at least 1×10^4 kPa (1500 psi). Post couplers with cryogenically inserted PEEK tubing were also tested and are identical in performance to couplers with glued tubing (at least 9×10^3 kPa or 1300 psi). Molded couplers, however, failed at about 6.2×10^3 kPa (900 psi) due to bond failure between the molding material and capillary. Using adhesive to strengthen the bond should improve the pressure rating. These results are summarized and compared to other work in Table 3.2.

Table 3.2 Coupler Testing Results Compared to Other Work

Coupler Description	Operation Range	Reference
Polyethylene Coupler/Tubing and Epoxy Reinforcement	> 5 kPa (0.7 psi)	[7]
Mylar Sealant and Epoxy Reinforcement with Capillary	~ 190 kPa (28 psi)	[5]
Polyimide/Parylene Ribbon Cable Style Interconnect	~ 200 kPa (29 psi)	[10]
Silicon Finger Microjoint with Silicone Gasket & Tygon Tubing	> 210 kPa (30 psi)	[11]
Thermoplastic Retaining Flange with PEEK Tubing	> 210 kPa (30 psi)	[4]
Silicon/Plastic Coupler with Silicone Gasket & Capillary	~ 410 kPa (60 psi)	[8]
Silicone Gasket Sealed Silicon Coupler with Capillary	~ 550 kPa (80 psi)	[13]
Silicon Sleeve Coupler with Capillary	~ 3.6×10^3 kPa (500 psi)	[8]
Polymer Coupler with Fused Silica Capillary	~ 6.2×10^3 kPa (900 psi)	This Work
Silicon Bulk Coupler with Fused Silica Capillary	> 9×10^3 kPa (1300 psi)	This Work
Silicon Post Coupler with Fused Silica Capillary or PEEK Tubing	> 9×10^3 kPa (1300 psi)	This Work
Silicon Flanged Coupler with PEEK Tubing	> 1×10^3 kPa (1500 psi)	This Work
Mismatched Silicon Coupler with Capillary	> 1.2×10^3 kPa (1740 psi)	[12]

3.4 DISCUSSION OF RESULTS

Determination of the failure load of the adhesive joint between the coupler and fluidic port is a difficult problem due to complex joint geometry and the inability to ascertain the exact failure mechanism(s). However, general observations concerning the design and resultant mechanical behavior of the joints can be made. Four types of stresses are considered when referring to adhesively bonded joints: (1) normal (or direct) stresses (including tensile and compressive), (2) shear stresses, (3) cleavage stresses, and (4) peel stresses.

Stress concentrations, as always, should be minimized. Also, to maximize strain capability and toughness of adhesives, joints are ideally designed to operate under compression and shear. Tension, cleavage, or peel stresses should be avoided as much as possible. Given these factors for consideration, post couplers are expected to have better performance since compression and shear have the largest stress contributions under loading. In addition, the surface roughness accumulated during the DRIE process promotes mechanical interlocking in addition to increasing the surface area available for bonding. This is also true of flanged couplers that not only provide a large flat surface for bonding but grooves for further increasing surface area available for bonding. Flanged and bulk-type couplers experience a combination of tension and shear stresses. By using liquid adhesives, the excess adhesive squeezed from the joint, or spew fillet, can provide the added benefit of reducing the stress concentration at the edges of joints and further increase overall strength [17].

Couplers have been successfully implemented with microchannels and flow sensors [18-20]. Packaged devices with couplers are shown in Figure 3-31 and Figure 3-32.

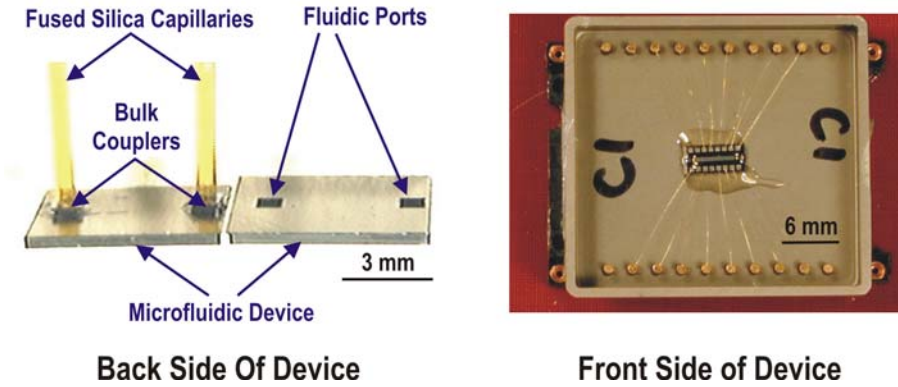


Figure 3-31 Silicon Bulk Couplers with Polyimide Coated Fused Silica Capillaries in a Microchannel Device [18]

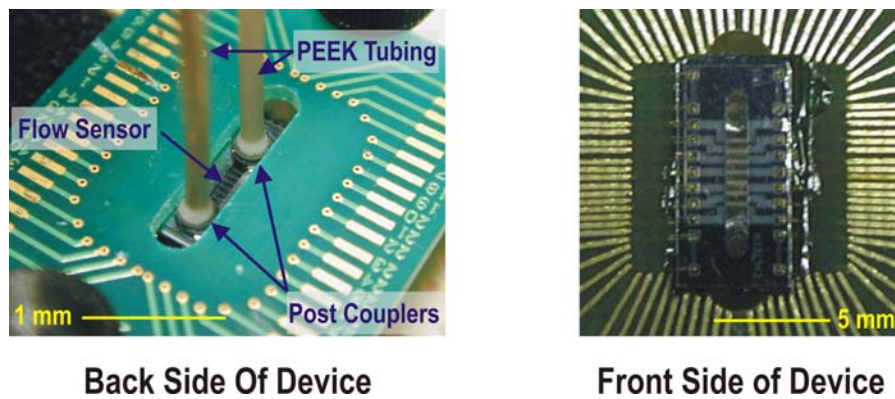


Figure 3-32 Silicon Post Couplers with PEEK Tubing in a MEMS Flow Sensor [20]

3.5 SUMMARY

In order to implement successful microfluidic systems, there is a need to create micro-to-macro world interconnects. In an effort to create standardized microfluidic connections to MEMS fluidic devices/systems, micromachined fluidic couplers have been designed, fabricated, and tested. These couplers are compatible with PEEK and fused silica capillary tubing and are capable of withstanding pressures up to 1×10^4 kPa (1500 psi). Furthermore, these couplers can be used with typical fluidic ports and can be customized for use with special geometries if necessary.

REFERENCES

- [1] Upchurch Scientific, *Micro Fluidic Connections Brochure*. <http://www.upchurch.com/>.
- [2] VerLee, D., A. Alcock, G. Clark, T.M. Huang, S. Kantor, T. Nemcek, J. Norlie, J. Pan, F. Walsworth, and S.T. Wong, *Fluid Circuit Technology: Integrated Interconnect Technology for Miniature Fluidic Devices*, in *1996 Solid State Sensor and Actuator Workshop*. 1996: Hilton Head, South Carolina. p. 9-14.
- [3] Darling, R.B., *Development of a High Density, Planar, Modular Microfluidic Interconnect System*, in *Transducers '01*. 2001: Munich, Germany. p. 974-977.
- [4] Puntambekar, A. and C.H. Ahn, *Self-aligning microfluidic interconnects for glass- and plastic-based microfluidic systems*. *Journal of Micromechanics and Microengineering*, 2002. **12**(1): p. 35-40.
- [5] Tsai, J.-H. and L. Lin, *Micro-to-macro fluidic interconnects with an integrated polymer sealant*. *Journal of Micromechanics and Microengineering*, 2001. **11**(5): p. 577-581.
- [6] Meng, E., S. Wu, and Y.-C. Tai, *Silicon couplers for microfluidic applications*. *Fresenius Journal of Analytical Chemistry*, 2001. **371**(2): p. 270-275.
- [7] van der Wijngaart, W., H. Andersson, P. Enoksson, K. Noren, and G. Stemme, *The First Self-Priming and Bi-Directional Valve-less Diffuser Micropump for Both Liquid and Gas*, in *MEMS 2000*. 2000: Miyazaki, Japan. p. 674-679.
- [8] Gray, B.L., D. Jaeggi, N.J. Mourlas, B.P. van Driehuisen, K.R. Williams, and N.I. Maluf, *Novel interconnection technologies for integrated microfluidic systems*. *Sensors & Actuators A*, 1999. **77**(1): p. 57-65.
- [9] Benett, W. and P. Krulevitch. *A flexible packaging and interconnect scheme for microfluidics systems*. in *SPIE Conference on Micro- and Nanofabricated Structures and Devices for Biomedical Environmental Applications II*. 1999. San Jose, CA.
- [10] Man, P.F., D.K. Jones, and C.H. Mastrangelo, *Microfluidic Plastic Interconnects For Multi-bioanalysis Chip Modules*, in *SPIE-Int. Soc. Opt. Eng. Proceedings of SPIE- Micromachined Devices and Components III*. 1997: Austin, TX. p. 196-200.
- [11] González, C., S.D. Collins, and R.L. Smith, *Fluidic interconnects for modular assembly of chemical microsystems*. *Sensors and Actuators B*, 1998. **49**(1-2): p. 40-45.
- [12] Spiering, V.L., J.N. van der Moolen, G.-J. Burger, and A. van den Berg, *Novel microstructures and technologies applied in chemical analysis techniques*, in *Transducers '97*. 1997: Chicago, IL. p. 511-514.

- [13] Yao, T.J., S.W. Lee, W. Fang, and Y.C. Tai, *A Micromachined Rubber O-Ring Microfluidic Coupler*, in *MEMS 2000*. 2000: Miyazaki, Japan. p. 624-627.
- [14] Yang, X., C. Grosjean, and Y.-C. Tai, *A Low Power MEMS Silicone/Parylene Valve*, in *1998 Solid-State Sensor and Actuator Workshop*. 1998: Hilton Head Island, South Carolina. p. 316-319.
- [15] Jiang, F., Y.-C. Tai, C.-M. Ho, R. Karan, and M. Garstenauer, *Theoretical and Experimental Studies of Micromachined Hot-Wire Anemometers*, in *International Electron Devices Meeting (IEDM)*. 1994: San Francisco. p. 139-142.
- [16] Enoksson, P., *New structure for corner compensation in anisotropic KOH etching*. *Journal of Micromechanics and Microengineering*, 1997. **7**(3): p. 141-147.
- [17] Kinlock, A.J., *Adhesion and Adhesives: Science and Technology*. 1987, London: Chapman and Hall.
- [18] Wu, S., J. Mai, Y. Zohar, Y.C. Tai, and C.M. Ho, *A Suspended Microchannel with Integrated Temperature Sensors for High-Pressure Flow Studies*, in *MEMS '98*. 1998: Heidelberg, Germany. p. 87-92.
- [19] Wu, S., Q. Lin, Y. Yuen, and Y.-C. Tai, *MEMS flow sensors for nano-fluidic applications*. *Sensors & Actuators A*, 2001. **89**(1-2): p. 152-158.
- [20] Meng, E., S. Gassmann, and Y.-C. Tai, *A MEMS Body Fluid Flow Sensor*, in *Micro Total Analysis Systems 2001*. 2001: Monterey, CA. p. 167-168.

CHAPTER 4

A MICRO FLOW SENSING ARRAY

Flow measurement is a centuries old science that dates back the ancient Romans. Perhaps like no other, the field of flow sensing embodies the motivations for microfabrication and MEMS. Previously, it has been difficult, if not impossible, to monitor small flows ($\mu\text{l}/\text{min}$ and lower) with conventional sensors. By scaling down conventional sensors, higher sensitivity in low flow ranges (down to nl/min) as well as lower power consumption can be achieved. Many diverse applications for flow sensing exist in the macro world. However, they serve a more important role in the micro realm. In microfluidics, flow sensors can complement valves and pumps in the role of flow control. With the advent of micro flow sensors, the precise flow control needed for micro total analysis systems or lab-on-a-chip is now possible. As interest in miniaturizing biological and chemical equipment continues to grow, flow sensing research will continue to advance and develop, becoming more sensitive and broader in operational range.

4.1 FLOW MEASUREMENT METHODS

Two standard flow measurement problems are flow velocity measurement and fluidic transport rate determination. The first case is for the flow velocity measurement in a flow field. Fluidic transport rate refers to the mass or volumetric flow rate of fluid that is confined in, for example, a pipe or channel. Both are possible using MEMS devices. For the purpose of microfluidics, the major interest lies in measuring flow restricted to microchannels.

4.1.1 PHYSICAL PRINCIPLES OF FLOW MEASUREMENT

Flow sensing is amenable to wide variety of physical sensing principles. A list of principles, along with some associated methods, is given in Figure 4-1, which is an adapted from [1]. This list is by no means comprehensive.

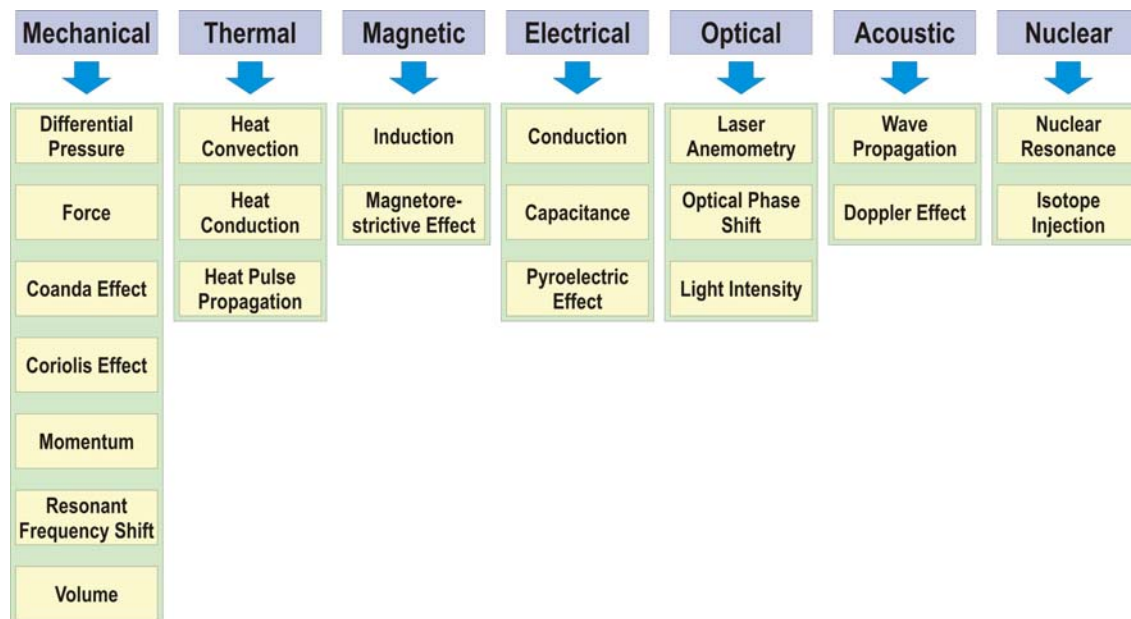


Figure 4-1 Physical Principles Used in Flow Measurement

It makes sense to categorize flow sensors as either non-thermal or thermal as heat and mass transfer are inseparably intertwined. In addition, nearly all of the physical flow sensing

methods are temperature dependent. A brief exploration of some of the more common types of flow sensors follows.

4.1.2 NON-THERMAL FLOW MEASUREMENT METHODS

A few non-thermal flow measurement methods are described here. Schematics of some common flowmeters are depicted in Figure 4-2 [2].

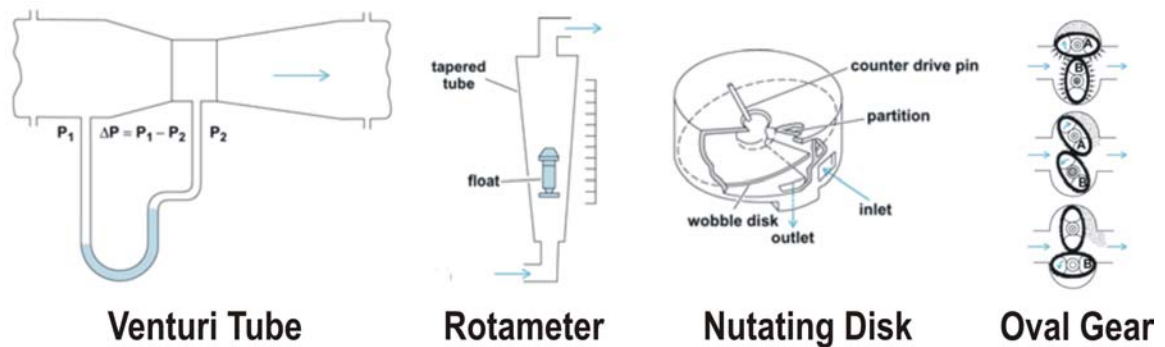


Figure 4-2 Examples of Conventional Flowmeters

4.1.2.1 DIFFERENTIAL PRESSURE FLOWMETERS

Differential pressure flowmeters rely on the pressure difference that results when a restriction is placed in a pipe. At the restriction, the flow velocity increases which in turn decreases the static pressure downstream. The pressure difference generated is a measure of the fluid flow rate through the restriction and the pipe as well. The two standard components found in differential pressure flowmeters are a differential producer (the restriction) and a differential pressure transducer.

This observation, that a differential pressure is produced by a restriction placed in a pipe, was made by Bernoulli. He also developed a useful relationship that describes the relationship between pressure, velocity, and elevation in a frictionless flow. This relation is known as the

Bernoulli equation and is helpful in understanding the operation of differential pressure flowmeters. For an inclined pipe, the generalized form of the Bernoulli equation holds [3]:

$$\frac{p_1}{\rho g} + \frac{v_1^2}{2g} + h_1 = \frac{p_2}{\rho g} + \frac{v_2^2}{2g} + h_2 \quad (4.1)$$

where:

p_1 = fluid pressure at point 1

v_1 = fluid velocity at point 1

h_1 = elevation at point 1

p_2 = fluid pressure at point 2

v_2 = fluid velocity at point 2

h_2 = elevation at point 2

ρ = fluid density

g = acceleration due to gravity.

In a horizontal pipe ($h_1 = h_2$), the equation reduces to:

$$\frac{p_1 - p_2}{\rho} = \frac{v_2^2 - v_1^2}{2} \quad (4.2)$$

By conservation of mass:

$$v_1 A_1 \rho = v_2 A_2 \rho \quad (4.3)$$

Equations 4.2 and 4.3 can be used to show how flow rate is measured by using a restriction in a pipe. The volumetric fluid flow rate, Q , can be determined by rearranging the equations:

$$Q = v_1 A_1 = \frac{A_2}{\sqrt{1 - \left(\frac{A_2}{A_1}\right)^2}} \sqrt{\frac{2(p_1 - p_2)}{\rho}} \quad (4.4)$$

This illustrates the basic principle behind differential pressure flowmeters.

4.1.2.1.1 ORIFICE PLATE

The simplest, least expensive variety of differential pressure flowmeter is an orifice plate. It is a thin plate with a hole cut into it that is inserted and then clamped between pipe flanges. Pressure taps before and after the orifice allow for the measurement of differential pressure. Although calibration is not needed, orifice plates suffer from limited range and sensitivity to flow disturbances.

4.1.2.1.2 VENTURI TUBE

The oldest form of differential pressure flowmeters is the Venturi tube (Figure 4-2). The differential producer here is a section of tubing having a converging inlet, cylindrical mid-section, and diverging outlet. Venturi tubes are characterized by less permanent pressure loss but lower differential pressures compared to orifice plates.

4.1.2.1.3 NOZZLE

Nozzle type flowmeters use a converging inlet as a differential producer. It combines beneficial features from both the orifice plate and Venturi tube.

4.1.2.2 VARIABLE AREA FLOWMETERS

As the name implies, variable area flowmeters achieve either a constant or variable differential pressure by forcing flow through a restriction that varies in size with the flow rate.

4.1.2.2.1 ROTAMETER

The most common variable area flowmeter is a rotameter (Figure 4-2). The basic rotameter consists of an element that changes its elevation with flow rate until gravitational, buoyancy, and drag forces are at balance on it.

4.1.2.2 MOVABLE VANE

Movable vane meters correlate flow rate to the position of a spring-loaded vane. At zero flow, the vane is held shut by the spring. Angular displacement of the vane occurs when flow forces the vane open. The resting angle of the vane results from balance of the dynamic flow force and spring restoring force and is, thus, flow rate dependent.

4.1.2.3 WEIR/FLUME

As opposed to rotameters or movable vane meters, weirs and flumes are designed for measuring flow in open-channel situations. Flow rate measurement is achieved by measuring the difference in height of the fluid level at an obstruction spanning the channel and at a point sufficiently upstream. Weirs cause water to rise upstream by providing flow resistance. Flumes are a low-pressure loss alternative to weirs. Instead of causing a rise in fluid level, a restriction in the channel causes the fluid level to sink due to the increase in flow velocity.

4.1.2.3 POSITIVE DISPLACEMENT FLOWMETERS

Positive displacement meters monitor the capture of discrete quantities of flow that are later released downstream. Flow rate is determined by looking either at the number of capture events over a set time period or at the number per unit time. Several types of positive displacement, or PD, meters are discussed below.

4.1.2.3.1 SLIDING-VANE

A sliding-vane meter traps fluid in known volumes in pockets defined by radially arranged vanes. Spring-loaded vanes are mounted eccentrically and rotate to pass volumes of flow.

4.1.2.3.2 BIROTOR & TRI-ROTOR

Both birotor and tri-rotor meters trap fluid between the rotors and an outer wall defined by the meter casing.

4.1.2.3.3 OVAL GEAR

Oval gear flowmeters deliver precise quantities of flow each revolution (Figure 4-2). Fluid is trapped between the gears and the chamber wall. Fluids that vary greatly in viscosity can be measured using this device.

4.1.2.3.4 NUTATING-DISK

The nutating-disk flowmeter consists of a circular disk on a spherical center that is confined in such a manner that is not permitted to rotate (Figure 4-2). When oriented correctly, the disk nutates when fluid strikes the disk. Fluid eventually escapes the chamber when the disk rotates to allow access to the outlet.

4.1.2.4 TURBINE AND IMPELLER FLOWMETERS

Turbine and impeller flowmeters use the conversion of velocity to proportional rotational speeds in order to measure flow rate. The rotating axis in turbine meters is parallel to the flow whereas in impellers, they are transverse to the flow.

4.1.2.5 ELECTROMAGNETIC FLOWMETERS

Electromagnetic flowmeters are only applicable to fluids that are conductive. By treating fluid as a conductor, when flowing fluid crosses a magnetic field applied to a tube, a voltage is generated between two electrodes on opposite sides of the tube. The induced voltage as a function of flow rate can be derived from Faraday's law of induction:

$$e = \frac{4BQ}{\pi D} \quad (4.5)$$

where:

e = induced voltage

B = magnetic field flux density

Q = volumetric flow rate

D = pipe diameter.

The two most commonly encountered electromagnetic flowmeters are AC and DC types.

4.1.2.6 VORTEX SHEDDING FLOWMETERS

When an obstacle is placed in a flow fluid, vortices form behind the obstacle and shed downstream. An array of vortices, or a von Karman street, result as a vortex forms on one side of the object followed by the formation of another vortex with opposite rotation on the other side in an alternating, repetitive manner. Vortex shedding flowmeters operate on the principle that the frequency of vortex shedding is proportional to and increases with flow velocity. This relationship is expressed as:

$$Q = \frac{f}{K} \quad (4.6)$$

where:

$$K = \frac{St'}{(A \times d)}$$

f = vortex shedding frequency

St' = meter Strouhal number

A = cross sectional area of pipe

d = width of shedding body.

4.1.2.7 ULTRASONIC FLOWMETERS

Like electromagnetic flowmeters, ultrasonic flowmeters also measure flow rate without pressure or head losses. Ultrasonic meters, however, can be applied to any fluid type. The five

types of ultrasonic flowmeters commonly found are transit time (sonic pulse tracking), Doppler (frequency shift due to interaction with flow), cross-correlation (sonic energy absorption), phase shift (of transmitting and receiving signal directed at flow), and drift (sonic signal attenuation) types.

4.1.2.8 DRAG FORCE FLOWMETERS

Drag force flowmeters measure the force exerted on the fluid by a drag element exposed to fluid flow. The expression for the drag force is:

$$F_D = \frac{C_D \rho A v^2}{2} \quad (4.7)$$

where:

F_D = drag force

C_D = overall drag coefficient

ρ = fluid density

A = projected area of body normal to flow

v = fluid velocity.

4.1.3 THERMAL FLOW MEASUREMENT METHODS

Thermal flow measurement methods work on the conversion of mechanical variables (flow) to thermal variable (heat transfer) and then finally to electrical signals (current or voltage) for practical sensing. This does not require any moving parts and so thermal flow sensors are perhaps the easiest to miniaturize. The heat transfer variables that are typically monitored to deduce flow rate are temperature, temperature difference, heating power, and thermal signal transfer. Thermal flow sensors consist of a combination of heaters and temperature sensors. The six possible operational modes of thermal sensors are given in Table 4.1 [1].

Table 4.1 Operational Modes of Thermal Mass Flow Sensors

<i>Heater Control</i> → <i>Evaluation</i> ↓	Constant Heating Power	<i>Heater Control</i> → <i>Evaluation</i> ↓	Constant Heater Temperature
Heater Temperature Difference	Hot-wire/Hot-film Time-of-flight Calorimetric	Heating Power Temperature Difference	Hot-wire/Hot-film Time-of-flight Calorimetric

Based on this observation, there are three types of thermal flowmeters: hot-wire/hot-film, calorimetric, and time-of-flight. They are described below.

4.1.3.1 HOT-WIRE AND HOT-FILM

Both hot-wire and hot-film sensors operate on the heat loss from a hot body when exposed to fluid flow. The components of such sensors include a flow channel, sensing element, and electronics for control and/or evaluation. The sensor element can be fabricated from a variety of materials with different temperature dependencies. Metals such as platinum or platinum alloys are frequently used. For most materials, the temperature dependence is expressed as:

$$R(T) = R(T_0)[1 + \alpha(T - T_0)] \quad (4.8)$$

where:

$R(T)$ = resistance at temperature T

T = temperature

α = temperature coefficient of resistivity (TCR).

The thermal flow characteristics of four operational modes covered by these sensors are shown in Figure 4-3 [4].

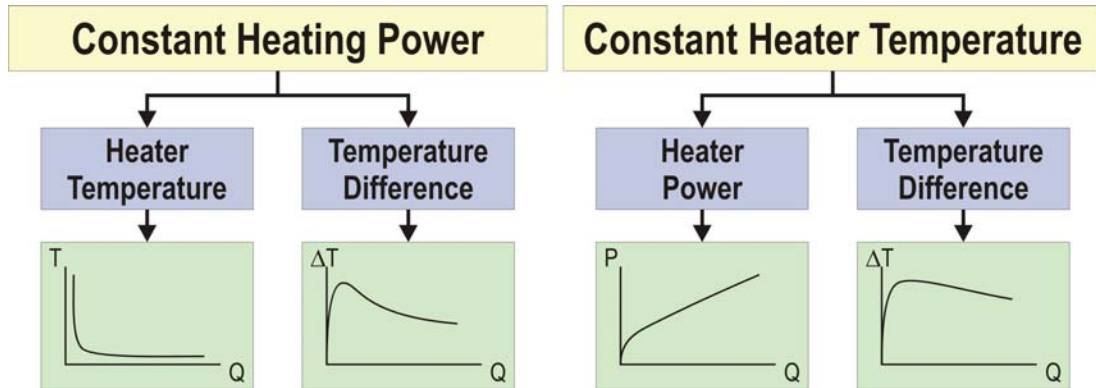


Figure 4-3 Hot-Film Operational Modes

4.1.3.2 CALORIMETRIC

Calorimetric sensors monitor the flow induced temperature profile asymmetry around a heating element. At least one sensor upstream and downstream is required to implement calorimetric sensing. This technique is sensitive to small flows and amenable to production by microfabrication techniques. Also, the presence of multiple sensors allows for the detection of flow direction. An analytical analysis of micro calorimetric flow sensors is given in [5]. For a simple, one-dimensional model of a micro sensor, the heater temperature is expressed as:

$$T_h = \frac{P}{k_F w_h \left(\frac{l_h}{\delta} + \sqrt{\frac{v\delta^2}{4a^2} + 4\kappa} \right)} \quad (4.9)$$

where:

T_h = heater temperature for constant heat power

P = heat power

k_F = thermal conductivity of fluid

w_h = heater width

l_h = heater length

δ = boundary layer thickness

v = average flow velocity

a = thermal diffusivity of fluid

$\kappa = \frac{1}{2} + \frac{k_{Si}t_d}{k_F\delta}$ = dimensionless factor

k_{Si} = thermal conductivity of silicon substrate

t_d = diaphragm thickness.

The temperature difference between temperature sensors is given by:

$$\Delta T = T_h [\exp(\gamma_2 l_d) - \exp(\gamma_1 l_u)] \quad (4.10)$$

where:

ΔT = temperature difference

$$\gamma_{1,2} = \frac{v \pm \sqrt{v^2 + 16a^2\kappa/\delta^2}}{4a\kappa}$$

l_u = distance to upstream sensor

l_d = distance to downstream sensor.

4.1.3.3 TIME-OF-FLIGHT

Time-of-flight flowmeters consist of a heater and one or more temperature sensors downstream. A pulse of heat is imposed on the fluid by the heater and detected downstream.

The time difference between the generation of the heat pulse to when it the maximum temperature at the downstream heater is reached is determined by the diffusivity of the fluid at low flow rates and by the heater-sensor distance ratio and average flow velocity at higher flow

rates. By approximating the heater as a line source, the analytical solution for heat transport is [6]:

$$T(x, t) = \frac{q_0}{4\pi kt} \exp\left[-\frac{(x - vt)^2}{4at}\right] \quad (4.11)$$

where:

T = temperature distribution at time t

x = distance from heater

t = time

q_0 = pulse signal input strength

k = thermal conductivity of fluid

v = average flow velocity

a = thermal diffusivity.

The top time is defined as the point where the maximum temperature is reached at the sensor. The time of flight of the heat pulse is deduced from the top time and if the heater-sensor distance is d_{hs} , it can be expressed as:

$$v = \frac{d_{hs}}{t} \quad (4.12)$$

On microfluidic scales, diffusion effects will dominate over forced convection and so the top time is given by:

$$\tau = \frac{-2a + \sqrt{4a^2 + v^2 d_{hs}^2}}{v^2} \text{ for } v \neq 0 \quad (4.13)$$

$$\tau = \frac{d_{hs}^2}{4a} \text{ for } v = 0 \quad (4.14)$$

4.1.4 FLOW SENSING PARAMETERS

Several parameters are commonly referred to when considering flow sensors. Most importantly, the quantity measured, or volumetric flow rate, is given as:

$$Q = \frac{dV}{dt} = vA \quad (4.15)$$

where:

Q = volumetric flow rate

V = volume through in time t

t = time

v = average velocity

A = cross-sectional area of channel.

The range of operation, or the maximum and minimum flow rate measurable, is often used to evaluate flowmeters. Another figure of merit is the sensitivity, which is the derivative of sensor signal with respect to flow rate or flow velocity:

$$S = \frac{dV}{dQ} \quad \text{or} \quad S = \frac{dV}{dv} \quad (4.16)$$

In the case of nonlinear flow characteristics, the sensitivity at zero flow is used:

$$S_0 = \left. \frac{dV}{dQ} \right|_{Q \rightarrow 0} \quad \text{or} \quad S_0 = \left. \frac{dV}{dv} \right|_{v \rightarrow 0} \quad (4.17)$$

The response time, or amount of time a sensor takes to stabilize after a change in flow rate, can vary as a result of a variety of factors including biasing conditions, construction materials, and sensor geometry. Power consumption will vary based on the sensor principle applied.

Flow in microchannels is typically laminar due to the small channel size and Reynolds number. The Reynolds number is a dimensional number used in fluid mechanics to show the relative importance of inertial effects to viscosity effects. It is expressed as:

$$\text{Re} = \frac{vL}{\nu} \quad (4.18)$$

where:

Re = Reynolds number

v = average flow velocity

L = characteristic length

$\nu = \frac{\mu}{\rho}$ = kinematic viscosity

μ = dynamic viscosity

ρ = fluid density.

For microchannels, the cross-sections encountered can be rectangular, circular, or whatever shape is desired. The characteristic length is determined by the channel geometry. For rectangular cross-section channels, the hydraulic diameter, D_h , is used. It is a function of the cross-sectional area, A , and wetted perimeter, U , and is expressed as:

$$D_h = \frac{4A}{U} = \frac{2wh}{w+h} \quad (4.19)$$

where:

w = width of channel

h = height of channel.

Finally, pressure loss can also be a factor. A derivation of the pressure loss in a microchannel of rectangular cross section can be found in [7]. The resulting expression is a linear function of flow velocity:

$$\Delta p = \frac{12\mu l}{h^3 w} Q \quad (4.20)$$

where:

Δp = pressure drop along channel

l = length of channel.

4.1.5 A BRIEF HISTORY OF MICROMACHINED FLOW SENSORS

Micromachined flow sensors have close to 30 years of developmental history with the goal of producing inexpensive, accurate, and reliable sensors in mind. During this time, flow sensors have evolved with the advancement of microfabrication technology and to meet new needs. The first silicon based flow sensor was presented in 1974 and is based on thermal sensing principles [8]. Research on discrete, monolithic sensors continued into the 1980's until the first sensor with an integrated channel was introduced in 1985 [9]. Prior to this work, sensors were brought into contact with the flowing medium. By fabricating channels to constrain fluid flow, even smaller flow rates could be measured. The recent trend in flow sensor research has been towards integration into complex microfluidic systems that include valves and pumps [10-13].

Arguably the most popular implementation of micro flow sensors is of the heat transfer type. It is the most promising flow sensing principle for measuring very low flow rates (< 1 ml/min). Other factors contributing to the continued popularity of thermal flow sensing are that thermal sensors can be simple in both structural and electronic implementation. It is no wonder that the bulk of micro flow sensor research has been focus on thermal principles. Several types of hot-film, calorimetric, and time-of-flight flow sensors have been implemented on the micro scale [5, 14-16]. Materials such as platinum, permalloy, gold, silicon, and doped polysilicon are used as sensing elements and heaters. While micromachined thermal flow sensors have a vast number of potential applications, sensor drift and the dependence on chemical properties of the fluid need can be problematic. Thermal flow sensors in certain configurations are also capable of determining thermal properties of the sensed fluid, such as thermal diffusivity and thermal conductivity [6, 17].

4.2 DEVICE DESIGN

Two iterations of a biocompatible MEMS thermal flow sensing array have been developed. Flow sensing is achieved by measuring the forced convective heat transfer from a thermal sensing element to the fluid in three different modes: hot-film, calorimetric, and time-of-flight. In this implementation, a linear array of seven metallic sensing elements is placed on a membrane that forms one side of a channel measuring $1 \text{ mm} \times .5 \text{ mm} \times 8 \text{ mm}$ (Figure 4-4). The resistive sensors are spaced $500 \text{ }\mu\text{m}$ apart, center-to-center. By implementing a resistive-sensing array, it is possible to use the three operational modes in the same device.

Materials for the different components were carefully chosen for this device. The membrane is made of parylene C, the properties and merits of which were discussed in detail in Chapter 2. It serves to prevent the flow from directly interacting with the sensors while minimizing

thermal losses. Platinum is chosen as the sensor for reasons that will be discussed in the next section.

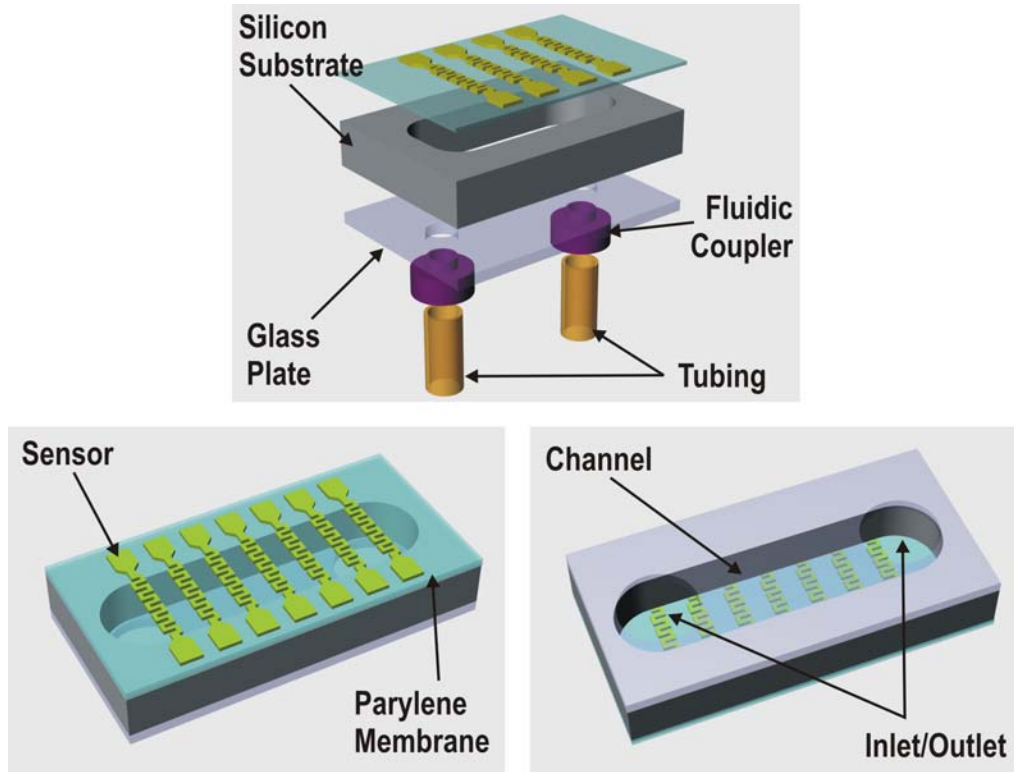


Figure 4-4 3D Views of the Flow Sensor

4.2.1 PLATINUM AS A THERMAL SENSING MATERIAL

Platinum is commonly found in temperature sensing devices for its stability, accuracy, and high temperature coefficient of resistivity (TCR). It is known for its excellent corrosion and oxidation resistance, biocompatibility, temperature stability, and wide temperature range. Unlike some metals, resistance dependence on temperature is quite linear (Figure 4-5) [18]. While Pt does not have the highest resistivity that can be found in metals, a reasonable TCR and other favorable characteristics make it a favorite in temperature sensing applications [19-22]. The properties of platinum are summarize in Table 4.2 [23] and a comparison of TCR and resistivity of common metals is found in Table 4.3 [18].

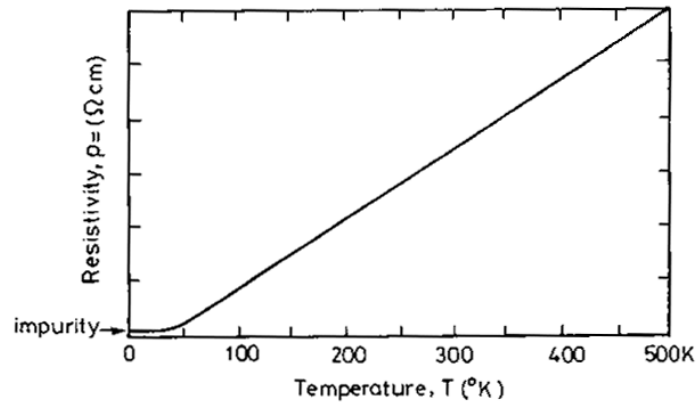


Figure 4-5 Electrical Resistivity of Platinum vs. Temperature

Table 4.2 Mechanical, Physical, and Thermal Properties of Platinum

Material Property	Value
Density (g/cm^3)	21.45
Hardness - Vickers	40-100
Bulk Modulus (GPa) (polycrystalline)	276
Tensile Modulus (GPa) (polycrystalline)	170
Tensile Strength (MPa)	125-300
Yield Strength (MPa)	14-185
Melting Point ($^{\circ}\text{C}$)	1772
Thermal Conductivity ($\text{W}/\text{m}/^{\circ}\text{K}$)	71.6
Specific Heat @ 25 $^{\circ}\text{C}$ ($\text{J}/^{\circ}\text{K}/\text{kg}$)	133
Coefficient of Thermal Expansion @ 0-100 $^{\circ}\text{C}$ ($10^{-6}/^{\circ}\text{K}$)	9.0

Table 4.3 TCR and Resistance Characteristics of Common Metals

Material	Resistivity, ρ ($10^8 \Omega \cdot \text{m}$) at 20 $^{\circ}\text{C}$	TCR, α ($10^{-4}/^{\circ}\text{K}$)
Aluminum	2.69	42.0
Copper	1.67	43.0
Gold	2.30	39.0
Iron	9.71	65.1
Nickel	6.84	68.1
Palladium	10.8	37.7
Platinum	10.6	39.2
Silver	1.63	41.0
Tungsten	5.50	46.0

Thin film platinum in microfabricated devices is typically deposited using one of three techniques: ac sputtering, magnetron evaporation, and electron beam evaporation. While nitrogen annealing may be required for Pt to adhere well to some materials, it is noted in [24] that Pt adheres very well to parylene C. Patterning platinum is typically done either by lift-off, as is standard with metal microfabrication, or wet etching in aqua regia. Wet etching, however, is difficult to control and can result in lateral undercut.

In this particular sensor, the presence of parylene C requires that the maximum process temperature to be kept lower than about 150 °C. This does not allow for the annealing of platinum to improve the TCR. As noted in [21], the TCR of thin film platinum is lower than in bulk platinum. This is especially true in sputtering and magnetron deposition techniques. The TCR of electron-beam evaporated Pt is quite close to that of the bulk material but high temperatures can be encountered during this process. Thus, sputtered Pt is used to fabricate these sensors.

4.3 FABRICATION

Two separate device runs were processed. The first sensor process flow was plagued by various problems. These issues were solved in the second run through a special platinum lift-off process and electroless gold plating of the contacts.

4.3.1 PROCESS FLOW 1

The first fabrication process is illustrated in Figure 4-6 and begins with a thermally oxidized (~ 1.8 μm) wafer. Although the actual channel is not etched until the end of the process, an etch stop must be placed down prior to depositing the membrane and sensors. A groove to contain the channel etch stop material is patterned and etched 4 μm deep by DRIE. The

groove is then filled in and planarized to the wafer surface with photoresist. Perfect planarization is difficult to achieve in this situation and is the result of many problems later in the process.

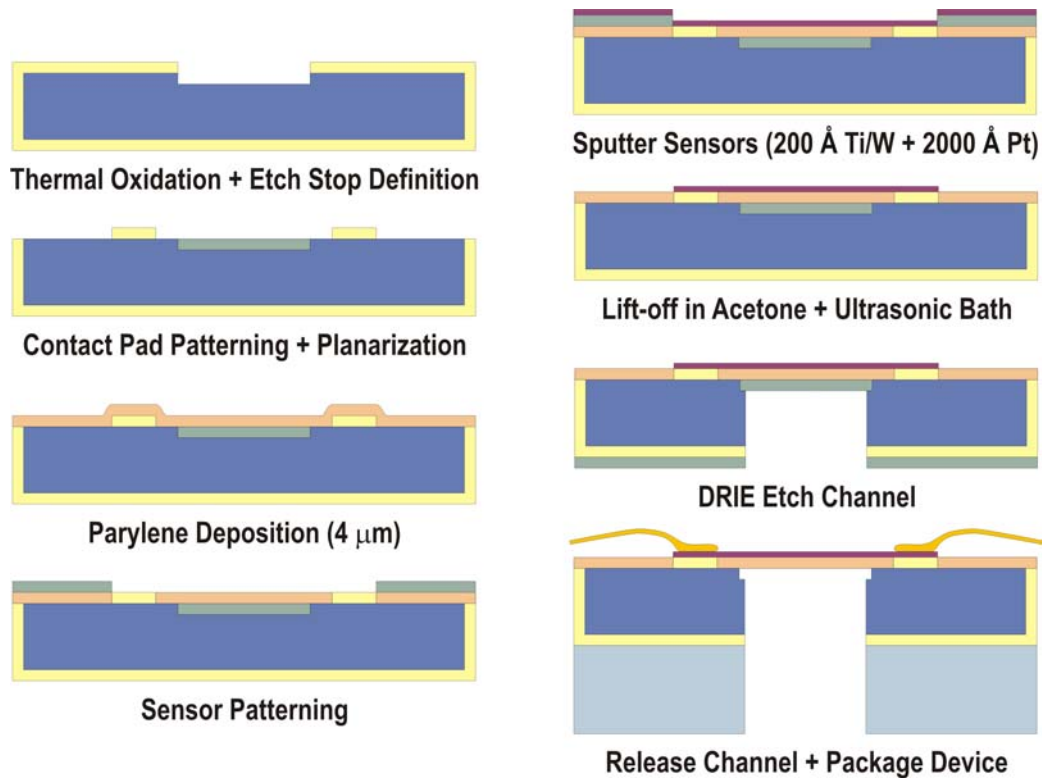


Figure 4-6 First Run Fabrication Process for Flow Sensor

The entire wafer is covered in a 4 μm thick layer parylene C. The parylene is patterned and etched away in oxygen plasma to expose oxide in the contact pad regions. This step anticipates Au wire bonding to the Pt pads that occurs during the packaging process. Wire bonding requires that the pad be on a rigid and hard material. If, for example, a soft material such as parylene is used below the metal pad, the wire bonding process will puncture and destroy the pad before a connection can be made.

A thick 6 μm layer of photoresist is spun, exposed, and developed in preparation for sensor patterning via lift-off. Thicker photoresist is required when lifting-off sputtered metal layers, as the coating tends to be more conformal than evaporated layers. For lift-off to occur, the deposited metal layer needs to be discontinuous. Pt sputtering is performed by the Lance Goddard Associates. A 200 \AA layer of Ti/W adhesion is sputtered first as an adhesion layer and then 2000 \AA of Pt is sputtered on top. The actual lift-off process involves dissolving away the photoresist underneath the metal, removing the metal at the same time. Wafers were immersed in acetone and placed in an ultrasonic bath. The agitation was supplemented by using a cleanroom swab or paintbrush to brush away loose metal flakes. Ideally, only the metal deposited directly on the parylene survives this process. However, the degree to which sputtering yields a conformal layer was underestimated, making this part of the process very difficult. Also, the non-uniformity in the parylene surface due to the texture of underlying layers made it difficult for the metal to cover certain portions of the wafer. The resulting patterned sensors were riddled with shorts and discontinuities that had to be removed manually. This entails manually connecting the metal traces using silver paste and a fine paintbrush. Photographs of the lift-off results are shown in Figure 4-7. This concludes processing on the front side of the wafer.

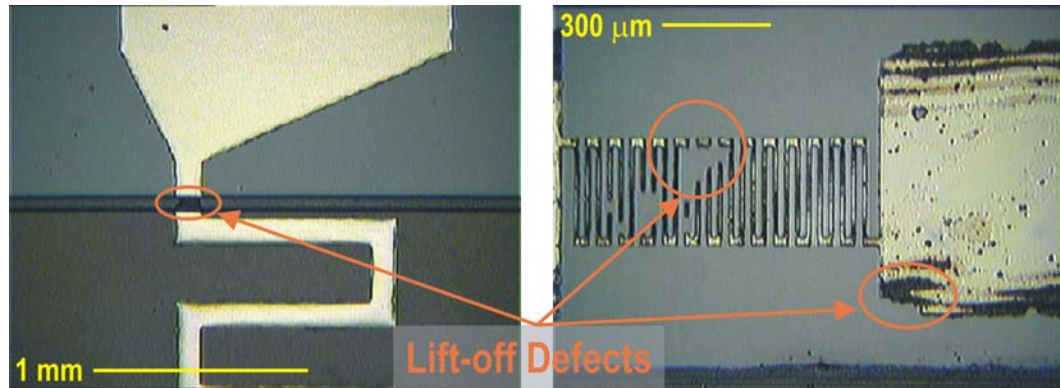


Figure 4-7 Lift-Off Results of First Fabrication Run

After protecting the features on the front side with a layer of photoresist, the channel is patterned on the backside. The channel is then etched through the wafer to the etch stop via DRIE. The wafer is diced and then membranes are released by removing the photoresist etch stop layer. Individual dies are cleaned thoroughly to remove any remaining photoresist and are prepared for packaging.

4.3.2 PROCESS FLOW 2

The improved and streamlined process flow begins in the same manner as the original process (Figure 4-8). Wafers are thermally oxidized ($\sim 1.8 \mu\text{m}$). This layer later serves as an etch stop and etch mask during channel formation by DRIE. Parylene adhesion promotion to the oxide layer is performed and then parylene C is deposited ($2 \mu\text{m}$). Again contact pads are patterned and the parylene in these areas is etched away by oxygen plasma for the same reasons previously mentioned. Next, sensors are patterned using a special lift-off patterning technique.

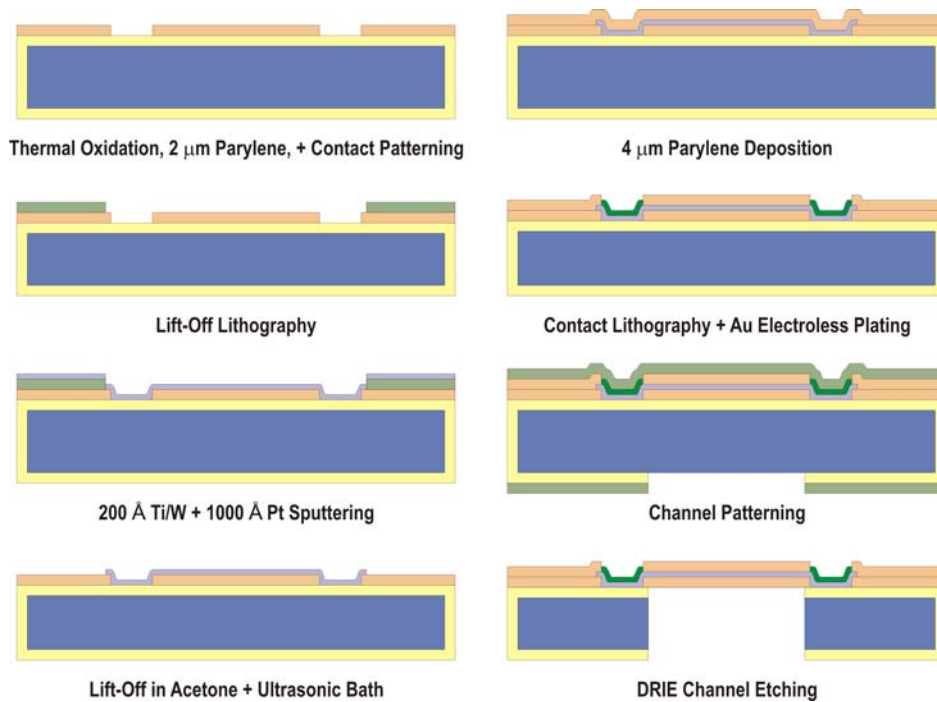


Figure 4-8 Second Run Fabrication Process for Flow Sensor

In the previous run, the conformal nature of the sputtered Pt prevented uniform lift-off. To avoid having the problem reoccur, an undercut photoresist lift-off mask is used. This specially designed technique is illustrated in Figure 4-9. The purpose of this process is to prevent the sputtered Pt layer from continuously covering the sidewalls of the photoresist lift-off pattern. The strategy here is to use a double photoresist layer to modify the edge profile. First, a thin layer of photoresist is spun (AZ1518 at 4 krpm for 40 s) and globally exposed. On top of this layer, a second, thicker layer of photoresist is spun (AZ4400 at 4 krpm for 40 s). The combined thickness of these two layers is approximately 4 μm . A 0.4 s exposure is sufficient to process this composite layer. Evidence of undercut of the first layer of photoresist is evident in exposure test patterns shown in Figure 4-10. A comparison is shown between a test pattern that has been perfectly exposed and developed and one that has been completely undercut during development.

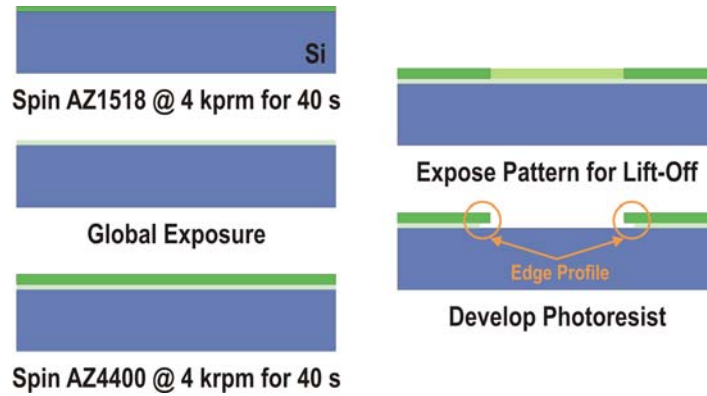


Figure 4-9 Process Steps for New Lift-Off Technique

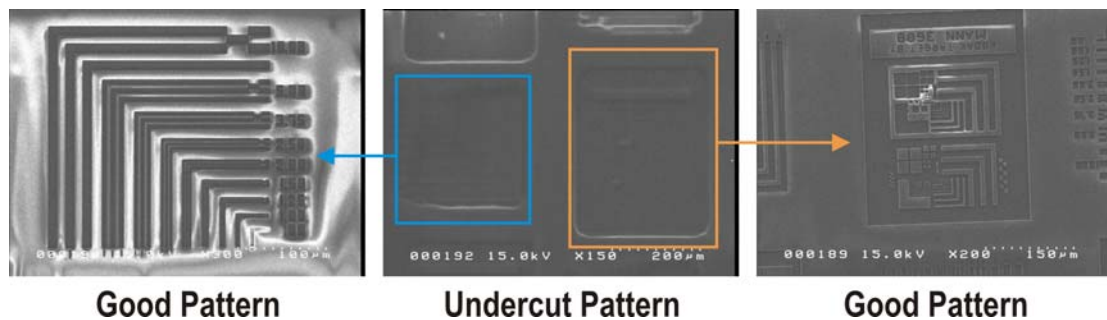


Figure 4-10 Comparison of Lithography Results for New Lift-Off Technique

Another process modification to avoid lift-off problems is that the Pt layer thickness was reduced. A 200 Å Ti/W adhesion layer and 1000 Å layer of Pt were sputtered offsite (Lance Goddard Associates). Lift-off is accomplished using the same technique discussed previously. The results are much improved over the first run (Figure 4-11). To protect these sensors, a second parylene layer is deposited (4 μm). Prior to the deposition, the wafer surface is briefly cleaned in oxygen plasma. Contact pads are patterned a second time and parylene is etched away, exposing Pt bonding pads. These pads are plated with electroless gold, a process that is described in more detail in the next subsection.

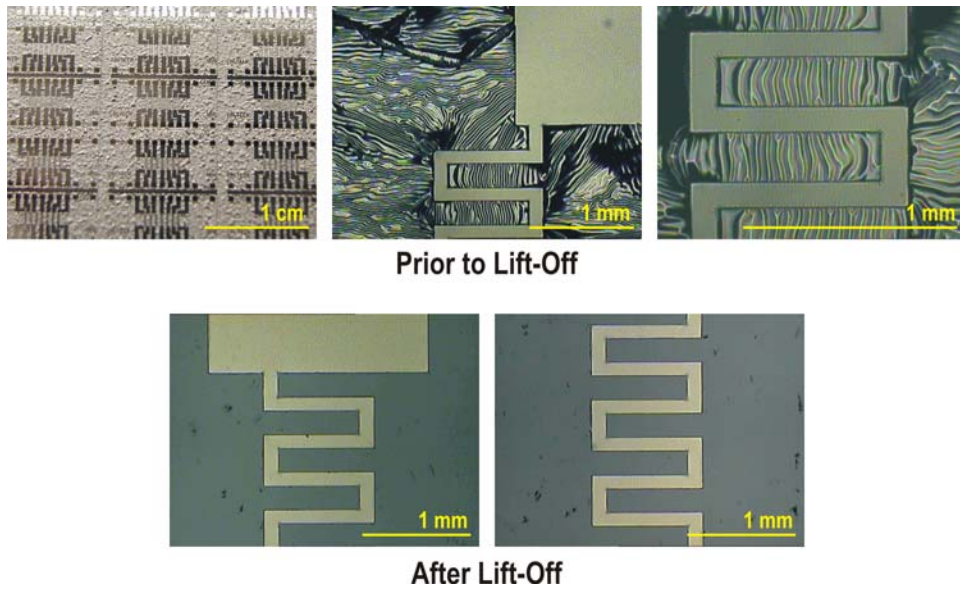


Figure 4-11 Lift-Off Results of Second Fabrication Run

After plating, the front side of the wafer is protected with a layer of photoresist. The backside is patterned to define the channel. DRIE is then used to etch the channel all the way through to the oxide etch stop. BHF vapor etching is performed to release membranes. Prior to releasing, the stress in the oxide layer is obvious upon visual inspection (

Figure 4-12). Finally, the wafers are diced to separate individual devices. Each device is cleaned thoroughly before packaging.

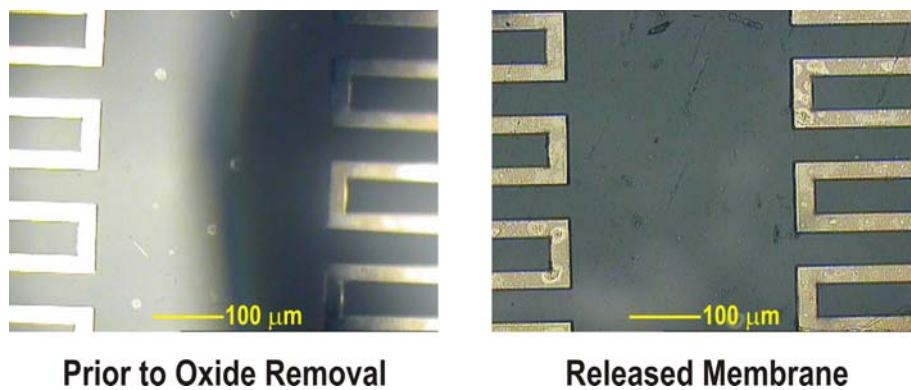


Figure 4-12 Effects of Oxide Stress on Sensor Membrane

4.3.2.1 ELECTROLESS GOLD PLATING

While it is possible to wire bond directly to platinum bond pads, it is by no means a trivial task. The Au-Au bonding systems are common and fairly well understood. One method to deposit Au onto Pt is electroless Au plating. The major benefit of using this technique for this particular application is that it is a low-temperature process. The autocatalytic Microgold Additive Deposition System (usually used with Al) produced by Stapleton Technologies Inc. was adapted for use with Pt. It is also possible to deposit solderable Au using this system. The process for electroless Au plating onto Pt bond pads is given in Table 4.4.

Table 4.4 Process for Electroless Au Plating on Pt

Process Step	Description
1. Residue Removal	If the wafer has been exposed to the ambient environment or handled extensively, it is necessary to remove built up residue. This can be achieved by immersing in citric acid of 20 g/l at 40 °C for 10 minutes. Adding a few milliliters of the MICRO 204 wetter into the citric acid solution will facilitate this process.
2. Oxide Removal	If the wafer has been exposed to the ambient environment, it is necessary to remove built up oxide. This can be achieved by immersing in a solution of 20% HCL at 40 °C for about 30 seconds.
3. Ni Plating	Plate an Au adhesion promoting Ni layer to about 5000 Å or for a few minutes at 83 °C. The solution make up is 500 ml/l of deionized water and 500 ml/l of MICRO 282SX.
4. Immersion Au	Plate a monolayer of Au onto the Ni undercoat. This step requires a 200 second immersion in a solution of 880 ml/l of deionized water and 120 ml/l MICRO 290B at 88 °C.
5. Auto-Catalytic Au	Plate Au until the desired thickness is reached. The solution make up is 400 ml/l of deionized water, 500 ml/l of MICRO 294A, and 100 ml/l of MICRO 294B where the optimal concentration of Au in the solution is 4g/l. Thick plates will require a concentration of 5 – 6 ml/l. The process temperature is set at 70 °C.

The first two steps clean and deoxidize the surface to be plated. A descum and oxygen plasma ashing process can further improve the surface properties prior to plating. Following cleaning, an adhesion layer is grown. A thin Ni layer allows Au to stick to the bonding pad. Then Au is deposited in two steps. First, an immersion Au is used. The purpose of this solution is to

prevent Ni contamination from affecting the regular, auto-catalytic Au plating bath. In addition, the immersion solution is cyanide based. During plating, the solutions need to be stirred for maximum film uniformity. The plating process is highly dependent on temperature and pH. Frequently, temperatures may need to be lowered in order to protect the device being processed. While plating will still occur, the rate will be reduced drastically.

4.4 PACKAGING

Both electrical and fluidic connections are required to operate the flow sensor. First, to complete the micro channel, a glass backing plate with inlet and outlet holes is necessary. Glass plates are cut to match the die and the fluidic ports are drilled into them by using small diameter diamond mandrels on a Servo mini drill stand. Epoxy is applied to seal the glass plates onto the sensor dies. This assembly can then be mounted onto a printed circuit board for making electrical connections. To do this, a slot is conventionally milled into the PCB to allow access to the sensor inlet and outlet. Assembled channels are then glued to PCB and positioned such that channel is over the milled slot. In this configuration, one side of the PCB is used for electrical connections and the other side allows for fluidic access. Once the chip is secured to the PCB, gold wire bonding is performed to electrically connect the sensor to the PCB. Later, wires can be soldered to the board for easy electrical access to the sensors. Finally, fluidic connections are made using silicon micromachined couplers described in the previous chapter. PEEK tubing is used in conjunction with silicon post couplers to provide fluid to the channel. Fully packaged sensors are shown in Figure 4-13.

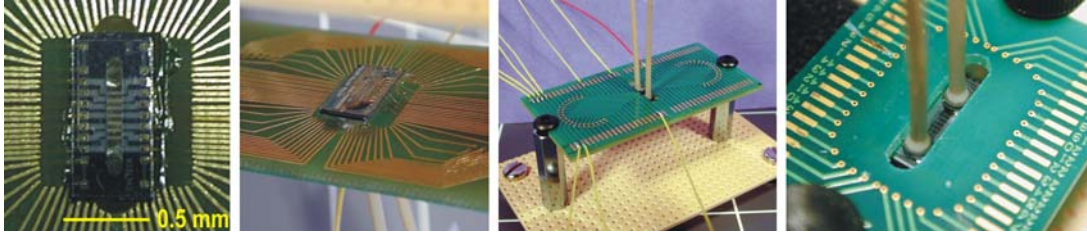


Figure 4-13 Views of Packaged Sensors With Electrical and Fluidic Connections

4.5 DEVICE CHARACTERIZATION

Devices from both process runs were calibrated and characterized against fluid flow.

4.5.1 TEMPERATURE CALIBRATION

The resistance dependence on temperature is given by Equation 4.8. To determine the TCR empirically, sensors subjected to known temperatures in a Delta Design 9010 Oven and their resistances at these temperatures were measured with an HP 34970A Data Acquisition System. Results for sensors from both process runs are given in Figure 4-14. The TCRs are 1.2×10^{-3} /°C (0.12 %/°C) and 1.0×10^{-3} /°C (0.1 %/°C), respectively. The relation is linear as expected, however a second order polynomial fit gives slightly better results.

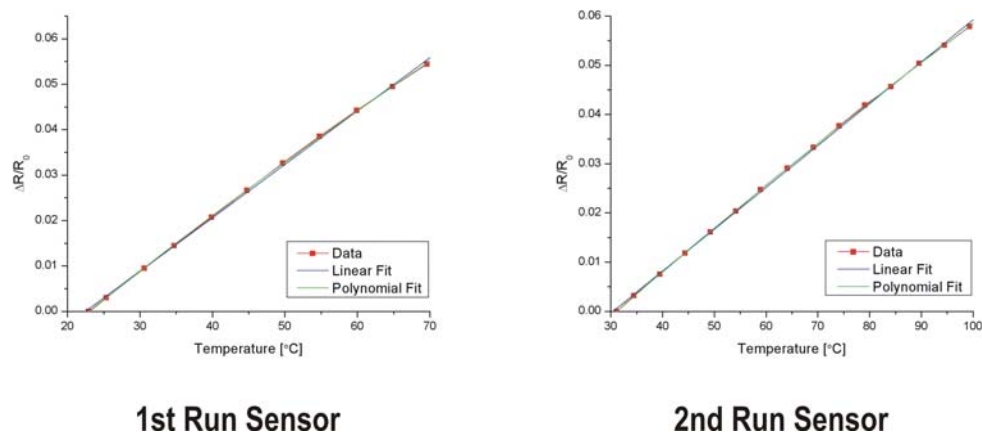


Figure 4-14 Temperature Calibration Curves for Both Flow Sensors

As previously mentioned, this measured TCR of thin film Pt is much less than bulk Pt ($3.92 \times 10^{-3} / ^\circ\text{C}$ or $0.392 \% / ^\circ\text{C}$). It is possible that contributions from the gold wire bonds and other electrical connections account for some part of this difference. However, it is well noted in Pt resistance temperature detector (RTD) fabrication, which uses Pt wire, that the best TCR values are obtained for only for the purest, unstrained Pt.

The IV curve for the first generation sensor is shown in Figure 4-15. As expected, it reflects the positive TCR coefficient of platinum and is relatively linear.

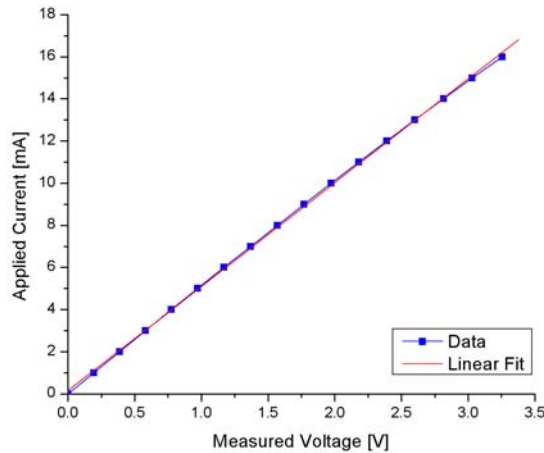


Figure 4-15 Flow Sensor IV Characteristics

The overheat ratio allows the temperature rise of the resistor to be calculated. It is the ratio of the change in resistance to the original resistance and is derived from Equation 4.8:

$$\frac{R(T) - R(T_0)}{R(T_0)} = \alpha(T - T_0) \text{ or } \frac{\Delta R}{R} = \alpha \Delta T \quad (4.21)$$

Typically, the overheat ratio is made as high as possible to maximize frequency response and sensitivity. However, in applications where temperatures must be kept low, tradeoffs are

necessary. The relationship of resistance and overheat temperature to the applied current for the first sensor is given in Figure 4-16. As this sensor is designed to be biocompatible and to be used with biological agents, an overheat temperature limit of about 10 °C is imposed. According to the graph, this condition can be met using a bias current of 8 mA which corresponds to an overheat temperature of 11 °C.

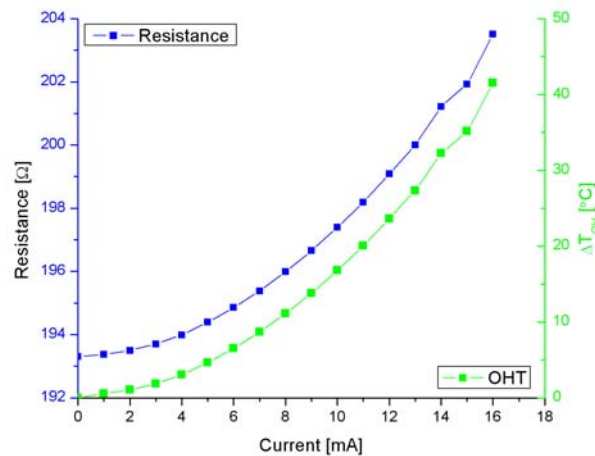


Figure 4-16 Resistance and Overheat Temperature Dependence on Current

4.5.2 HOT FILM MODE FLOW TESTING

Hot film mode flow sensors can be operated using two bias schemes: (1) constant heating power or constant heater current and (2) constant heater temperature. The latter requires additional feedback circuitry to main the heater temperature and is thus more difficult to implement. However, compared to constant current operation, constant temperature operation usually has better frequency response. Here, only constant current biasing is considered.

4.5.2.1 CONSTANT CURRENT OPERATION

The testing setup for constant current operation of the first generation sensor is given in Figure 4-17. An HP 34970A Data Acquisition System monitors the output voltage of the sensor while fluid is forced through the channel by a compressed nitrogen source. The flow rate is adjusted by a metering valve and calibrated using a stopwatch and precision pipette. An HP 3245A Universal Source holds the sensor bias constant at 30 mA. This corresponds to an overheat ratio of 1.9% and power consumption of 36 mW.

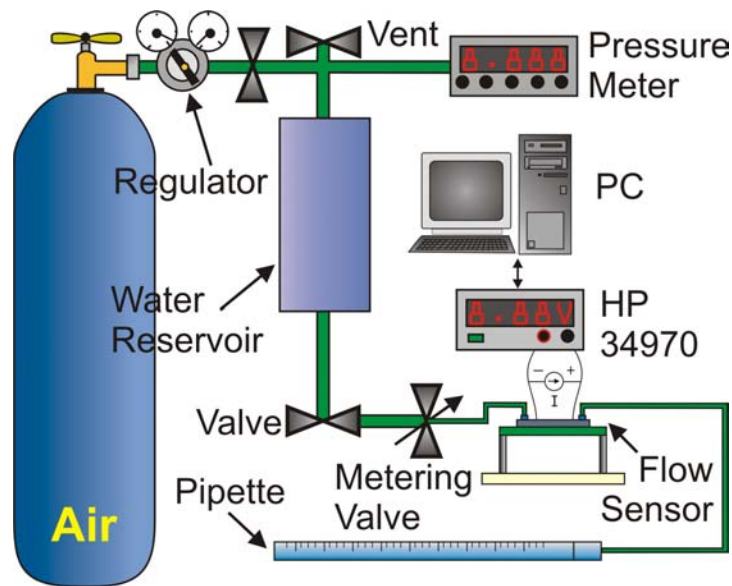


Figure 4-17 Flow Sensor Testing Setup

The sensor response to flow rate was adjusted to remove the effects of ambient temperature fluctuations and is shown in Figure 4-18. The sensor can resolve up to $10 \mu\text{l}/\text{min}$ flow. Commercial devices with such resolution are not currently available.

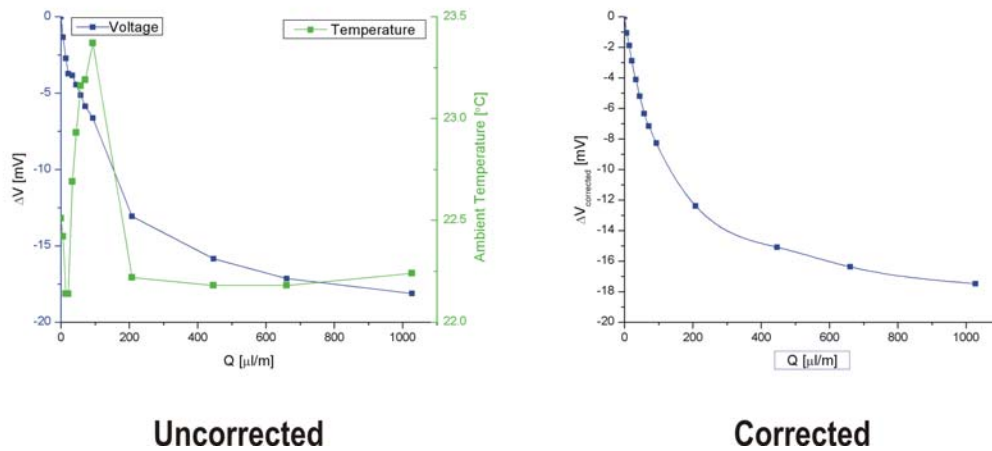


Figure 4-18 Uncorrected and Corrected Sensor Output vs. Flow Curves

The second generation sensor was tested with an improved testing setup (Figure 4-19). Instead of using compressed nitrogen to force fluid past the sensor, a syringe pump is used to accurately supply filtered deionized water. During flow testing, the sensor is placed in a thermally isolating enclosure to reduce adverse effects from ambient temperature fluctuations. In addition to hot-film mode operation, these sensors were also tested under the calorimetric and time-of-flight modes. Results for these modes will be discussed later. For hot-film operation, the sensors were biased at constant current and placed in a half bridge for temperature compensation purposes. The bridge is zeroed using a precision multi-turn potentiometer. The bridge output vs. flow rate was observed for three different overheat ratios Figure 4-20.

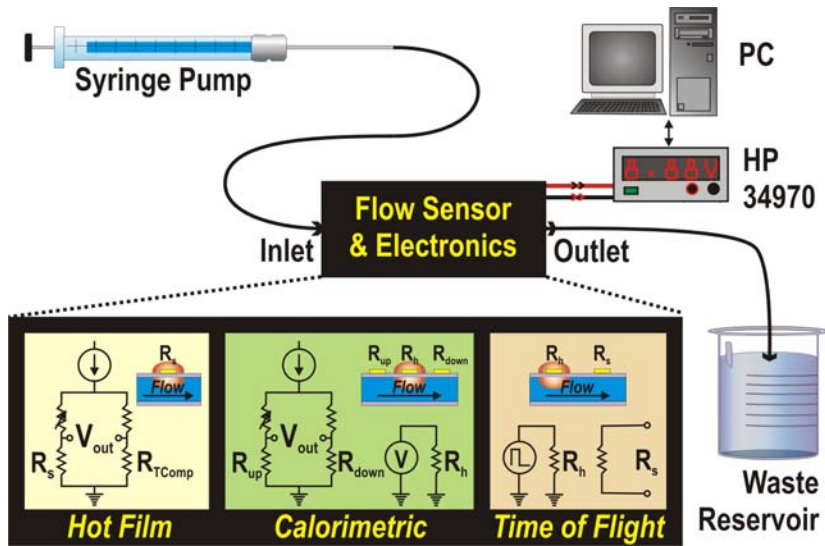


Figure 4-19 Improved Flow Sensor Testing Setup

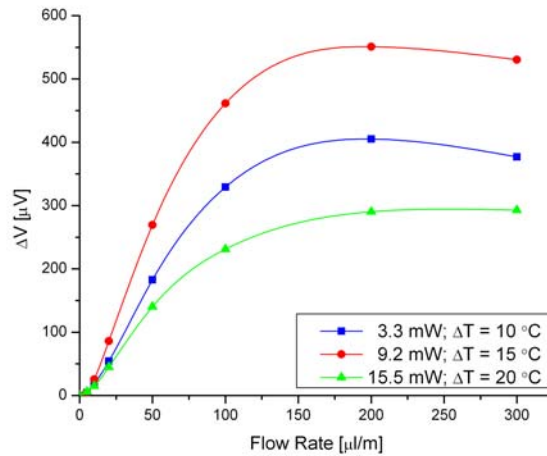


Figure 4-20 Flow Sensor Output at Three Different Overheat Ratios

Sensitivity values can be calculated for the sensors from Equation 4.17. The following table summarizes the sensitivity performance of the sensors based on the above results.

Table 4.5 Sensitivities in Hot-Film Mode

	1 st Sensor	2 nd Sensor ($\Delta T_{OH} = 10^{\circ}C$)	2 nd Sensor ($\Delta T_{OH} = 15^{\circ}C$)	2 nd Sensor ($\Delta T_{OH} = 20^{\circ}C$)
Units	[mV/ μ l/min]	[μ V/ μ l/min]	[μ V/ μ l/min]	[μ V/ μ l/min]
Sensitivity	0.10	3.45	5.11	2.67

4.5.2.2 KING'S LAW

It is useful to compare the sensor output results with King's Law. This heat transfer law for hot wire anemometry describes heat transfer from a cylinder of infinite length:

$$\Delta V(v) = a + bv^n \quad (4.22)$$

where:

ΔV = flow induced voltage difference

v = velocity

a, b, n = constants.

For the first sensor, good agreement with King's Law is obtained for the following constant values (Figure 4-21):

$$a = 0.8559$$

$$b = -0.8788$$

$$n = 0.51.$$

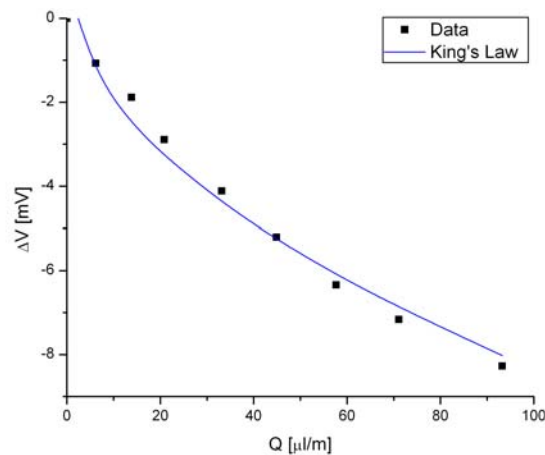


Figure 4-21 Agreement of Sensor Output With King's Law

4.5.2.3 TRANSIENT RESPONSE

The transient response was also evaluated for the first sensor. Results for sensor response at zero flow and non-zero flows are given in Figure 4-22. As expected, the device responds more quickly to higher flow rates.

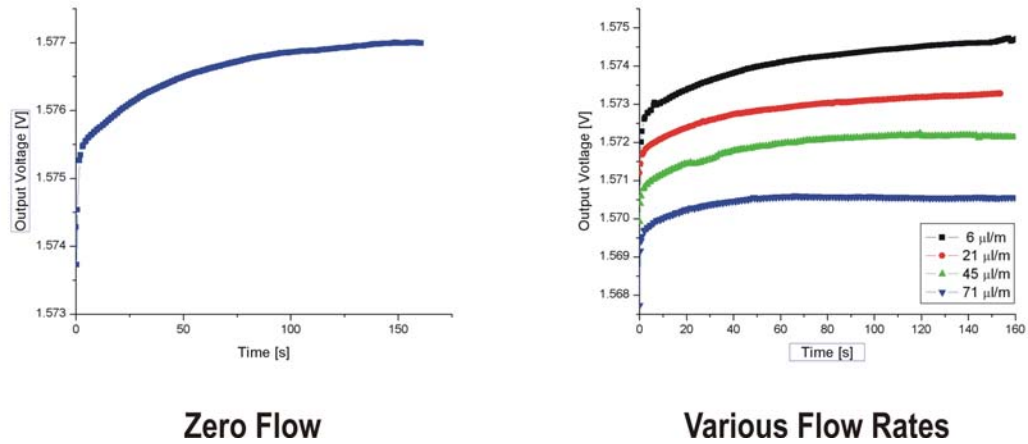


Figure 4-22 Sensor Response at Various Flow Rates

Based on the behavior seen above, the transient output voltage is governed by two time constants. In other words, it can be expressed as the superposition of a short and long time response (two exponentials). Time constants were measured for various flow rates and fitted (Figure 4-23). The shorter time constant follows this relationship:

$$\tau_1(Q) = 0.987 - 0.0266Q^{1/2} + 0.00026Q$$

The longer time constant can be estimated by:

$$\tau_2(Q) = 57.419 - 3.811Q^{1/2} + 0.064543Q$$

The first time constant is typically less than 1 s and the second ranges from 10 to 60 s. These decrease as flow rate increases.

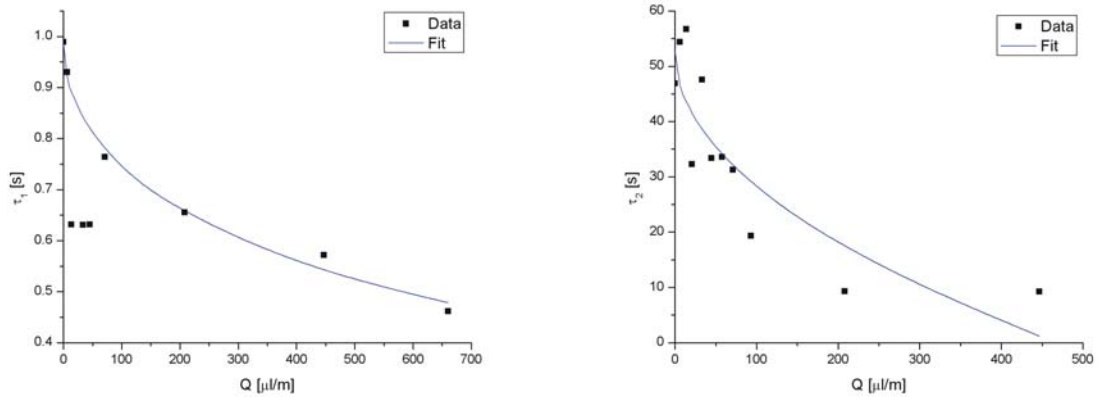


Figure 4-23 Short and Long Sensor Time Constants

4.5.3 CALORIMETRIC MODE FLOW TESTING

Calorimetric testing involves measuring the displacement of the temperature profile around a heating element. As the flow sensor consists of an array of resistive sensors, calorimetric operation can be achieved by converting a sensing element into a heater. The responses from sensors on either side of the heater are simultaneously monitored. Both symmetrical and asymmetrical upstream and downstream sensor arrangements can be investigated. The heater is biased at 5 mA, which corresponds to a local rise in temperature of 15 °C. Both the upstream and downstream sensors are placed in a bridge. The bridge output for sensors spaced asymmetrically around a heater is shown in Figure 4-24.

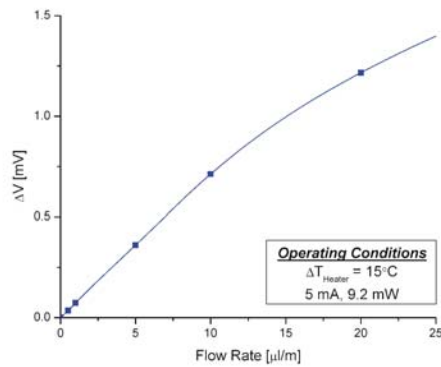
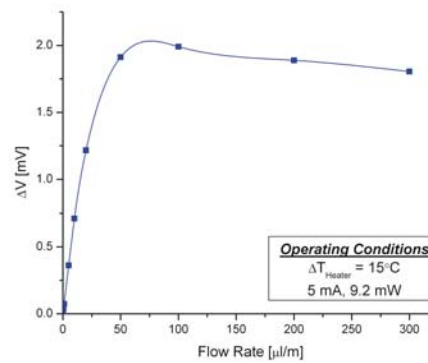
**Zoomed In On Low Flow Range****Entire Flow Range**

Figure 4-24 Calorimetric Testing Results

4.5.4 TIME-OF-FLIGHT MODE FLOW TESTING

Time-of-flight flow sensing involves tracking a heat pulse from an upstream heater. Again, a resistive sensing element can be converted to a heater for this mode of operation. The sensor response to a single heat pulse (3 V in amplitude and 1 s duration) is shown in Figure 4-25. The local temperature rise is approximately 24 °C for these settings. A bridge is not required and the sensor output is read directly using the data acquisition system.

The quantity of interest in time-of-flight operation is the “top time,” or time at which the maximum temperature is reached at the sensor. This corresponds to the time at which the heat pulse response of the sensor peaks. The top time is plotted against flow rate in Figure 4-25. The temperature sensed at the heater is calculated and also displayed. It is also interesting to superimpose all of the detected heat pulses in one graph. The difference in heat dissipation between lower and higher flow rates can easily be seen (Figure 4-26).

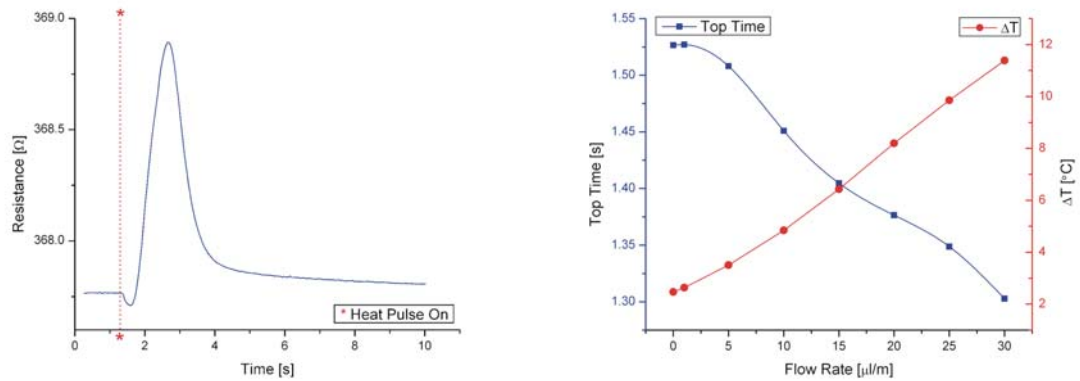


Figure 4-25 Heater Response to a Heat Pulse and Time-of-Flight Results

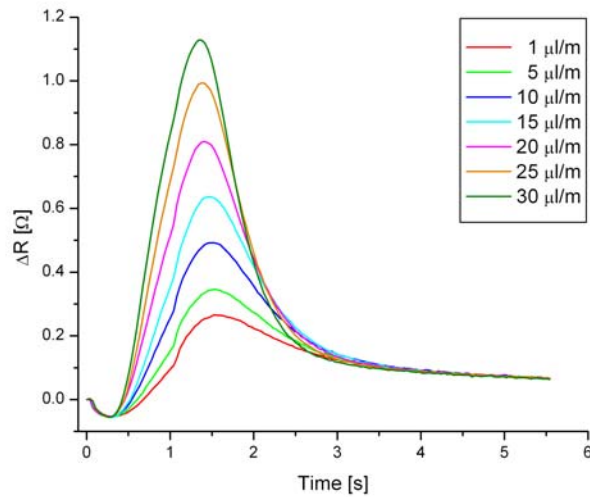


Figure 4-26 Superimposed Detected Heat Pulses at Different Flow Rates

4.5.5 BUBBLE DETECTION

As the heat capacities of air and water are quite different, the heat transfer when an air bubble passes a biased sensor drops off dramatically. This phenomenon is potentially useful for determining the passage of solid particles. The signal output during the passage of a bubble train was recorded (Figure 4-27). Bubble events are clearly indicated. In addition, the widths of the bubble event peaks roughly correspond to the size of the bubble.

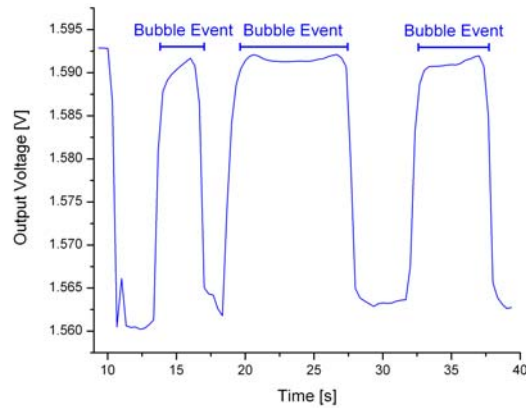


Figure 4-27 Sensor Response to the Passage of an Air Bubble Train

4.6 DISCUSSION OF MULTI-MODE TESTING RESULTS

A comparison of the testing results of the various operational modes shows that the calorimetric principle yields the best results in terms of sensitivity over a wide range of operation (0.5 to 300 $\mu\text{l}/\text{m}$). The hot-film technique lacks resolution at lower flow rates, and below 5 $\mu\text{l}/\text{m}$, flows are difficult to observe. Time-of-flight sensing yields good results for a specific flow range that is neither high nor low. While it was not shown using this sensor, it is also possible to determine the direction of fluid flow using a combination of two sensors.

One of the drawbacks of using thermal sensing is that a calibration must be performed for each type of liquid that needs to be measured. The variation in response due to heat capacity differences between fluids can be exploited. If a library of calibration curves for different fluids is compiled, the sensor can then be used to determine the identity of unknown samples. It is also possible to configure the sensor to measure different thermal quantities of the fluids.

4.7 SUMMARY

The first parylene MEMS thermal sensor array capable of detecting small flows down to 0.5 $\mu\text{l}/\text{min}$ has been demonstrated. Because of the array design, for the first time we are able to study and compare the insightful results from three different methods of flow sensing using one single device. By using parylene and platinum to construct the device, it is suitable in applications requiring biocompatibility and minimal heating ($<20\text{ }^{\circ}\text{C}$) of the sensed medium.

REFERENCES

- [1] Nguyen, N.-T. and S.T. Wereley, *Fundamentals and Applications of Microfluidics*. 2002: Artech House, Inc.
- [2] AccessScience, *Flow Measurement*. http://www.accessscience.com/server-java/Arknoid/science/AS/Encyclopedia/2/26/Est_261700_printable.html.
- [3] White, F.M., *Fluid Mechanics*. 3rd ed. 1994: McGraw Hill, Inc.
- [4] Nguyen, N.T. and R. Kiehnscherf, *Low-cost silicon sensors for mass flow measurements of liquids and gases*. Sensors and Actuators A, 1995. **49**(1-2): p. 17-20.
- [5] Nguyen, N.-T. and W. Dötzel, *Asymmetrical locations of heaters and sensors relative to each other using heater arrays: a novel method for designing multi-range electrocaloric mass-flow sensors*. Sensors & Actuators A, 1997. **62**(1-3): p. 506-512.
- [6] van Kuijk, J., T.S.J. Lammerink, H.-E. de Bree, M. Elwenspoek, and J.H.J. Fluitman, *Multi-parameter detection in fluid flows*. Sensors & Actuators A, 1995. **47**(1-3): p. 369-372.
- [7] Wu, S., *Integrated Polysilicon Thermistors for Microfluidic Sensing*, Ph.D. Thesis in *Electrical Engineering*. 2000, California Institute of Technology: Pasadena, CA.
- [8] Van Putten, A.F.P. and S. Middelhoek, *Integrated Silicon Anemometer*. Electronics Letters, 1974. **10**(21): p. 425-426.
- [9] Petersen, K., J. Brown, and W. Renken, *High-Precision, High-Performance Mass-Flow Sensor With Integrated Laminar Flow Micro-Channels*, in *Transducers '85*. 1985: Philadelphia, PA. p. 361-363.
- [10] Lee, S.W., W.Y. Sim, and S.S. Yang, *Fabrication and in vitro test of a microsyringe*. Sensors and Actuators A, 2000. **83**(1-3): p. 17-23.
- [11] Lammerink, T.S.J., M. Elwenspoek, and J.H.J. Fluitman, *Integrated Micro-Liquid Dosing System*, in *MEMS '93*. 1993: Fort Lauderdale, FL. p. 254-259.
- [12] Laurell, T., L. Wallman, and J. Nilsson, *Design and development of a silicon microfabricated flow-through dispenser for on-line picolitre sample handling*. Journal of Micromechanics and Microengineering, 1999. **9**(4): p. 369-376.
- [13] Gass, V., B.H. Vanderschoot, S. Jeanneret, and N.F. Derooij, *Integrated Flow-Regulated Silicon Micropump*. Sensors and Actuators A, 1994. **43**(1-3): p. 335-338.
- [14] van Oudheusden, B.W., *Silicon thermal flow sensors*. Sensors and Actuators A, 1992. **30**(1-2): p. 5-26.

- [15] Yang, C.Q. and H. Soeberg, *Monolithic Flow Sensor For Measuring Milliliter Per Minute Liquid Flow*. Sensors and Actuators A, 1992. **33**(3): p. 143-153.
- [16] Nguyen, N.-T., *Thermal Mass Flow Sensors*, in *The Measurement, Instrumentation, and Sensors Handbook*, J.G. Webster, Editor. 1999, CRC Press: Boca Raton, Florida.
- [17] van Baar, J.J., R.W. Wiegerink, T.S.J. Lammerink, G.J.M. Krijnen, and M. Elwenspoek, *Micromachined structures for the thermal measurements of fluid and flow parameters*. Journal of Micromechanics and Microengineering, 2001. **11**(4): p. 311-318.
- [18] Gardner, J.W., *Microsensors: Principles and Applications*. 1994: John Wiley & Sons, Inc.
- [19] Dittmann, D., R. Ahrens, Z. Rummler, K. Schlote-Holubek, and W.K. Schomburg, *Low-cost flow transducer fabricated with the AMANDA-process*, in *Transducers '01*. 2001: Munich, Germany. p. 1472-1475.
- [20] Kreider, K.G. and F. DiMeo, *Platinum/palladium thin-film thermocouples for temperature measurements on silicon wafers*. Sensors & Actuators A, 1998. **69**(1): p. 46-52.
- [21] Mailly, F., A. Giani, R. Bonnot, P. Temple-Boyer, F. Pascal-Delannoy, A. Foucaran, and A. Boyer, *Anemometer with hot platinum thin film*. Sensors & Actuators A, 2001. **94**(1-2): p. 32-38.
- [22] van Honschoten, J., J. van Baar, H.E. de Bree, T. Lammerink, G. Krijnen, and M. Elwenspoek, *Application of a microflown as a low-cost level sensor*. Journal of Micromechanics and Microengineering, 2000. **10**(2): p. 250-253.
- [23] Goodfellow, *Material Information Platinum*.
<http://www.goodfellow.com/csp/active/static/A/PT00.HTML>.
- [24] Vaeth, K.M. and K.F. Jensen, *Transition metals for selective chemical vapor deposition of parylene-based polymers*. Chemistry of Materials, 2000. **12**(5): p. 1305-1313.

CHAPTER 5

A MEMS FLUID DOSING SYSTEM

Recently, there has been a great deal of interest in creating microfluidics for use in the chemistry and biology. The possibility of systems level microfluidics promises improved performance and functionality. By virtue of miniaturization alone, traditional processes can benefit from faster processing times and lower consumption of expensive reagents. There is also the intriguing possibility that new solutions to studying interesting problems in chemistry and biology will be available by using microfluidic techniques.

5.1 MICROFLUIDIC SYSTEMS

Few question the benefits of moving towards microfluidic systems for biological and chemical applications. In fact, several commercial efforts have embraced the new technology and are actively marketing pioneering products in the field. Agilent's now has a whole line of Lab-on-a-Chip products aimed at bioanalysis. Their primary product relies on a single platform to perform processes from protein purification to RNA isolation. Caliper Technologies

Corporation produces a high throughput screening system that allows for tens of thousands of experiments on a single chip that require only nanoliters of reagent. Academic researchers have also made significant contributions to the advancement of systems level microfluidics. One area of interest is in fluid dosing applications [1-4].

Micro-dosing systems are referred to as micro-dispensers, micro-injectors, and micropipettes. One might typically use a dosing system at the front end of an analysis system to provide accurate fluid doses or flow rates. There are two categories of dosing systems: (1) open loop and (2) closed loop. Open loop systems can actually be a single device that generates identical droplets or in-channel dispensers that deliver fixed flow volumes. While simplistic and easy to implement in massively parallel dosing schemes, open loop systems are not suitable for continuous flow applications. Closed loop systems are ideal for continually monitoring and adjusting the flow rate. An electrical signal from the sensor is fed back to the fluid actuator to make this adjustment. The components required to implement a closed loop fluid dosing system are a fluid actuator, flow sensor, fluidic interconnects, and control and bias electronics.

5.2 DOSING SYSTEM CONSTRUCTION

To demonstrate the possibility of using MEMS devices and technology to create integrated microfluidic systems, a fluid dosing system was assembled from the components previously presented. Here, the check-valved diaphragm pump is connected to a downstream flow sensor aided by fluidic couplers and tubing. For simplicity, closed-loop control is not implemented. Alternatively, the flow sensor can also be placed upstream, between the pump and fluid supply. The schematic of the system demonstrated here is shown in Figure 5-1.

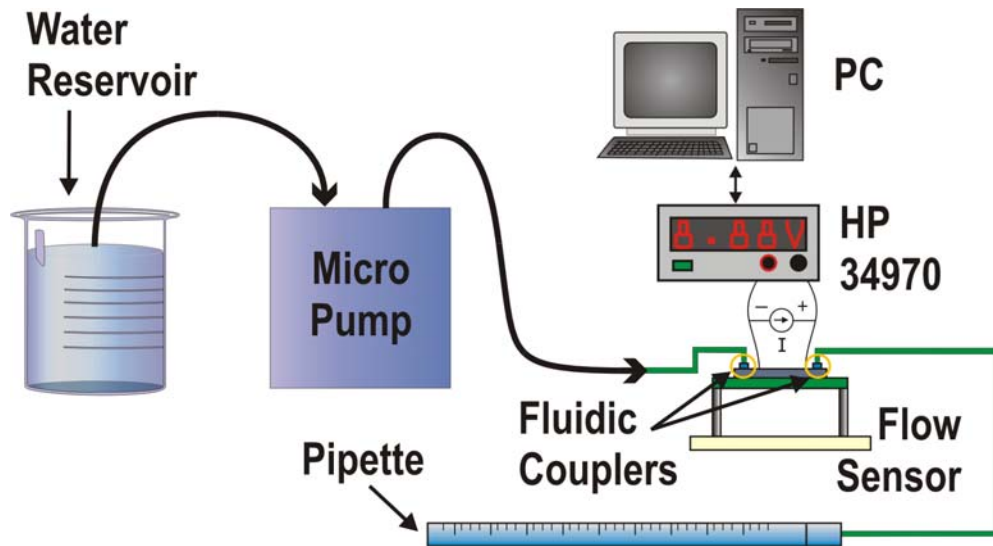


Figure 5-1 Schematic of Micro Dosing System

5.3 TESTING RESULTS

To show the ability of the micro flow sensor to measure flow for the purposes of flow regulation, a solenoid-actuated micropump was attached to it. Filtered deionized water was pumped through the system to a calibrated micropipette where the flow rate was measured by a stopwatch. The flow sensor was operated in time-of-flight mode using a 3 V, 1 s electrical pulse.

A comparison of the detected signal in terms of resistance change at 0 flow and at 46 $\mu\text{l}/\text{m}$ is shown in Figure 5-2. Values for top times and response peaks for both signals are indicated. The solenoid actuation frequency necessary to provide this flow rate is 10 Hz. Noticeable roughness exists at the peak of the 10 Hz signal. This is most likely due to the pulsing effect of the micropump. Each pump cycle results in the ejection of a plug of flow. However, in the ideal case, the supply cycle results in no flow. Thus, flow is not entirely continuous. This effect is more pronounced at lower flow rates. It may be possible to provide more continuous flow by chaining two micropumps together and operating them out of phase.

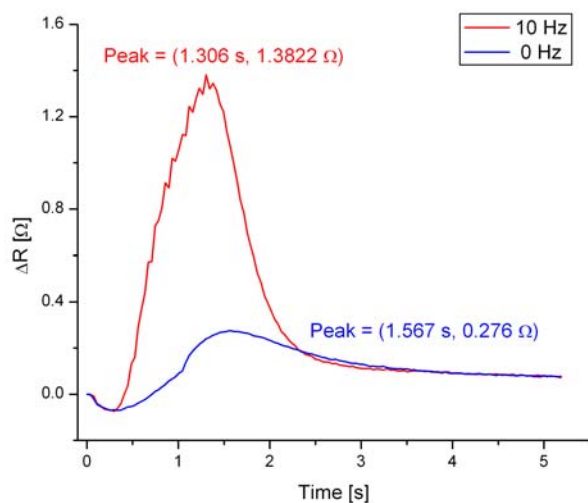
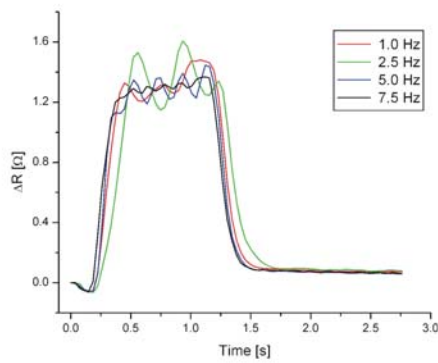


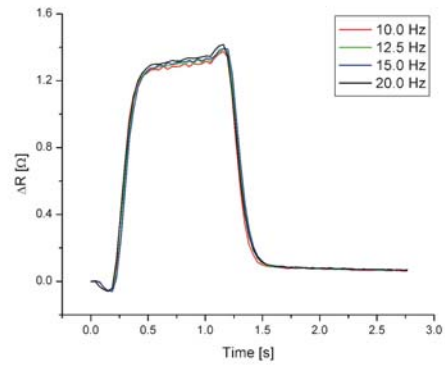
Figure 5-2 Flow Sensor Response to Micropump Induced Flow in Time-of-Flight Mode

5.4 DISCUSSION

Although time-of-flight mode testing is not ideal for non-continuous flow analysis, it can yield some information about the flow. For the particular case of flow pulsing seen in the micropump, the relative effect at different actuation frequencies can be visualized using time-of-flight testing. As previously observed, the flow sensor response curves exhibit roughness. At lower frequencies (<10 Hz), the roughness is large and pulsing is evident. At higher frequencies (> 10 Hz), the curves are smoother but the top time peaks are flattened. These results correlate well with visual observations of the flow at these frequencies. The signals deviate significantly from those in Figure 4-25, where the flow sensor was provided continuous flow by a syringe pump.



Low Frequency Responses



High Frequency Responses

Figure 5-3 Pump Behavior Analysis by Time-of-Flight Flow Testing

This system demonstrates the feasibility and usefulness of an integrated dosing system. A further refinement on this system would be to scale the entire system down to chip level. In applications where small flow rates are desired, a surface micromachined channel with integrated flow sensor and pump can be designed. Fluidic couplers can be used to provide fluidic access to the device. In addition, it is easy to include valving structures.

5.5 SUMMARY

A system level implementation of MEMS fluidic devices has been presented using interconnected discrete devices. A micro diaphragm pump and fluid flow sensor are connected using microfluidic couplers to form a fluid delivery system. The flow analysis capability of a micro thermal flow sensor in a fluid dosing system has also been demonstrated. Further miniaturization of this system by surface micromachining can result in a chip level system.

REFERENCES

- [1] Gass, V., B.H. van der Schoot, S. Jeanneret, and N.F. de Rooij, *Micro liquid handling using a flow-regulated silicon micropump*. Journal of Micromechanics and Microengineering, 1993. **3**(4): p. 214-215.
- [2] Lammerink, T.S.J., M. Elwenspoek, and J.H.J. Fluitman, *Integrated Micro-Liquid Dosing System*, in *MEMS '93*. 1993: Fort Lauderdale, FL. p. 254-259.
- [3] Handique, K., D.T. Burke, C.H. Mastrangelo, and M.A. Burns, *Nanoliter-volume discrete drop injection and pumping in microfabricated chemical analysis systems*, in *1998 Solid-State Sensor and Actuator Workshop*. 1998: Hilton Head, SC. p. 346-349.
- [4] Nguyen, N.T., S. Schubert, S. Richter, and W. Dötzel, *Hybrid-assembled micro dosing system using silicon-based micropump/valve and mass flow sensor*. Sensors and Actuators A, 1998. **69**(1): p. 85-91.

CHAPTER 6

CONCLUSION

For a MEMS micro fluid dosing system to be realized, several components are necessary. The essential components include a fluid actuator, a fluidic control device, and micro plumbing. A prototype fluid delivery system is demonstrated here using a micropump as the fluid actuator, a thermal flow sensor as the fluidic control device, and micromachined couplers as plumbing. The technology to build these components has been developed and each of these components have been fabricated and tested.

Various micro diaphragm pumps were designed to achieve the maximum flow rate possible using microfabricated parts. For the first time, high-flow parylene check valves are demonstrated for flow rectification in pumping applications. A new double-sided check valve process was designed and fabricated in two flavors, including a novel three check valve array format. Additional technological improvements include the usage of a bossed silicone membrane to improve pump performance at higher frequencies and silicone gaskets for

watertight sealing. Both pneumatic and external solenoid actuation were explored. High water flow rates of up to 13 ml/min and a maximum back pressure of 5.9 kPa were achieved through pneumatic operation with an external compressed air source. Using a custom designed solenoid actuator, flow rates of up to 4.5 ml/min and a maximum back pressure of 2.1 kPa have been demonstrated.

Microfluidic devices require custom solutions to achieve fluidic and electrical interconnects in the same real estate. To successfully connect to a wide variety of microfabricated fluidic devices, a family of couplers were created that take into account the most commonly encountered geometries of fluidic ports in the various types of construction materials used. In addition, the technology used in fabricating the couplers is amenable to creating couplers with any arbitrary two-dimensional shape. Four types of couplers adapted for compatibility with PEEK and fused silica capillary tubing were designed, fabricated, and tested. The large operational range of up to 1×10^4 kPa (1500 psi) allows flexibility in both high- and low-pressure applications. These couplers have been implemented in bulk and surface micromachined channel systems.

Flow sensing plays a crucial part in flow control. For micro flow sensing applications, thermal sensing arrays provide many advantages over other methods including simplicity of fabrication and implementation. The first parylene MEMS thermal sensor array has been demonstrated. Furthermore, this device is constructed of parylene and platinum, making it suitable for applications where biocompatibility is necessary. This sensor is integrated into a bulk micromachined channel and is capable of detecting flows down to 0.5 $\mu\text{l}/\text{min}$. By virtue of the array format, it is possible to study and compare insightful results from three different methods of flow sensing using one single device. The methods demonstrated here are hot-

film, calorimetric, and time-of-flight. Only minimal heating of the sensed medium is required in the operation of this device (<20 °C). The potential application of bubble detection has also been demonstrated.

Discrete system components were joined using micromachined couplers to assemble a micro dosing system. Analysis of the non-continuous flow characteristic of cycled micro diaphragm pump operation was performed using time-of-flight sensing methods. This demonstrated yet another facet of thermal flow sensing. By scaling this discrete system down into a surface micromachined channel with integrated pump and flow sensors it is possible to remove troublesome external connections between the fluid actuator and flow sensor. While other pump actuation methods and layouts may be necessary for channel integration, the thermal flow sensor requires scaling alone. Micromachined fluidic couplers can conveniently bring fluid into and out of such a system.

All the necessary components for a micro fluid dosing system have been demonstrated here. A prototype constructed of discrete components has also been shown. Both the pump and flow sensor can be scaled down to provide a truly integrated, channel-based fluid dosing system.

